

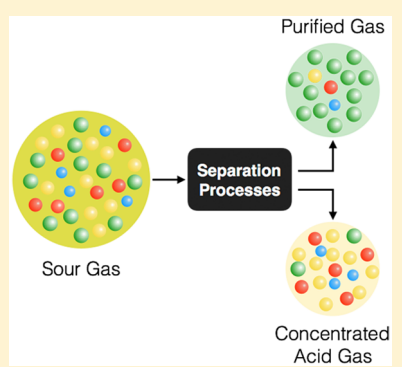
## Hydrogen Sulfide Capture: From Absorption in Polar Liquids to Oxide, Zeolite, and Metal–Organic Framework Adsorbents and Membranes

Mansi S. Shah,<sup>†</sup> Michael Tsapatsis,<sup>†</sup> and J. Ilja Siepmann<sup>\*,†,‡,§,||</sup>

<sup>†</sup>Department of Chemical Engineering and Materials Science, University of Minnesota, 421 Washington Avenue SE, Minneapolis, Minnesota 55455-0132, United States

<sup>‡</sup>Department of Chemistry and Chemical Theory Center, University of Minnesota, 207 Pleasant Street SE, Minneapolis, Minnesota 55455-0431, United States

**ABSTRACT:** Hydrogen sulfide removal is a long-standing economic and environmental challenge faced by the oil and gas industries. H<sub>2</sub>S separation processes using reactive and non-reactive absorption and adsorption, membranes, and cryogenic distillation are reviewed. A detailed discussion is presented on new developments in adsorbents, such as ionic liquids, metal oxides, metals, metal–organic frameworks, zeolites, carbon-based materials, and composite materials; and membrane technologies for H<sub>2</sub>S removal. This Review attempts to exhaustively compile the existing literature on sour gas sweetening and to identify promising areas for future developments in the field.



### CONTENTS

1. Introduction	9755	4.1. Polymeric Membranes	9785
2. Absorption	9758	4.2. Membranes for Gas–Liquid Contact	9786
2.1. Alkanolamines	9758	4.3. Ceramic Membranes	9789
2.2. Methanol	9758	4.4. Carbon-Based Membranes	9789
2.3. <i>N</i> -Methyl-2-pyrrolidone	9758	4.5. Composite Membranes	9790
2.4. Poly(ethylene glycol) Dimethyl Ether	9759	5. Cryogenic Distillation	9790
2.5. Sulfolane and Diisopropanolamine	9759	6. Outlook and Perspectives	9791
2.6. Ionic Liquids	9759	Author Information	9792
3. Adsorption	9762	Corresponding Author	9792
3.1. Metal Oxides	9762	ORCID	9792
3.2. Metals	9767	Notes	9792
3.3. Metal–Organic Frameworks	9768	Biographies	9792
3.4. Zeolites	9772	Acknowledgments	9792
3.4.1. All-Silica Zeolites	9772	References	9792
3.4.2. Aluminosilicate Zeolites	9773		
3.4.3. Titanosilicates	9775		
3.5. Carbon-Based Adsorbents	9775		
3.5.1. Activated Carbons	9775		
3.5.2. Structured Carbons	9775		
3.6. Composite Materials	9778		
3.6.1. Metal Oxides/Mesoporous Silica	9778		
3.6.2. Supported Amines	9778		
3.6.3. Zeolite/Polymer	9780		
3.6.4. Metal–Organic Framework/Graphite Oxide	9780		
3.6.5. Metal (Hydr)oxide/Graphite Oxide	9782		
3.6.6. Metal Oxide/Activated Carbon	9782		
4. Membrane Separation	9782		

### 1. INTRODUCTION

Hydrogen sulfide (H<sub>2</sub>S) is a colorless gas with a characteristic odor of rotten eggs. It is highly toxic, corrosive, and flammable in nature. Since H<sub>2</sub>S is heavier than air, it has a tendency to settle in low-lying and poorly ventilated areas (see Table 1 for the properties of H<sub>2</sub>S). It causes irritation to the eyes, nose, and throat at concentrations as low as 5 ppm and is fatal over 1000 ppm.<sup>1</sup> Inhalation is the primary route for H<sub>2</sub>S exposure. At ~30 ppm, H<sub>2</sub>S paralyzes the sense of smell and is rapidly absorbed

**Special Issue:** Carbon Capture and Separation

**Received:** February 14, 2017

**Published:** July 5, 2017

**Table 1.** Some Physical Properties of H<sub>2</sub>S

property	value
molar mass	34.081 g/mol
specific gravity	1.2
lower explosive Limit (LEL)	4.5%
upper explosive limit (UEL)	46%
normal boiling point	212.9 K
melting point	190.9 K
critical temperature	373.4 K
critical pressure	89.7 bar
critical density	0.349 g/cm <sup>3</sup>
kinetic diameter	3.6 Å
dipole moment	0.97 D
odor	rotten eggs
appearance	colorless gas
threshold limit value (TLV)	1 ppm
immediate danger limit	100 ppm

by the blood, resulting in poor oxygen uptake at the cellular level. Therefore, one should not fully trust their sense of smell for the presence of H<sub>2</sub>S because alarming concentrations may be present with no perceivable odor. Handling of H<sub>2</sub>S requires stringent safety regulations such as trained personnel, complete set of personal protective equipment including a gas mask, strategically located sensors, and emergency evacuation plans. Experimental studies with H<sub>2</sub>S at concentrations of a few hundred parts per million are challenging enough; the challenge is even greater at the percentage-level concentrations in actual gas-processing facilities.

H<sub>2</sub>S occurs naturally, at varied concentrations, in various hydrocarbon sources such as crude petroleum, natural gas, and biogas (see Table 2). It is also formed by the hydrolysis reaction of metal sulfides present in volcanic rocks. Anaerobic respiration of sulfate-reducing bacteria, whereby these organisms breathe sulfate to derive energy and release sulfide as waste, constitutes another major natural source of H<sub>2</sub>S. Landfills, rotten vegetation, and composting sites can also contribute to H<sub>2</sub>S generation; caution should be exercised in dealing with these not-so-obvious sources of H<sub>2</sub>S.

Anthropogenically, the main source of H<sub>2</sub>S is in oil refineries, wherein desulfurization of various gas streams using hydrogen gas generates H<sub>2</sub>S (also known as hydrodesulfurization). This process is essential to reduce the sulfur content of automobile and heating fuels, since combustion of sulfur compounds will result in emission of harmful sulfur oxides to the atmosphere

that can, in turn, give rise to acid rain. Hydrodesulfurization is also important since sulfur compounds, often at very low concentrations, can deactivate noble metal catalysts for downstream catalytic reforming units. Gasification of coal and biomass for syngas (CO + H<sub>2</sub>) production, under high temperature and low oxygen concentrations, results in a conversion of the sulfur content of these resources into H<sub>2</sub>S.

For any of the hydrocarbon streams, such as natural gas, biogas, or syngas, to be useful for energy generation or chemicals production, they need to be purified to remove unacceptable amounts of acid gases such as H<sub>2</sub>S and CO<sub>2</sub>. The acceptable H<sub>2</sub>S levels can be quite different depending on the end use; for example, 5–15 ppm H<sub>2</sub>S is acceptable in natural gas depending on the country of use, but <1 ppm H<sub>2</sub>S is required for fuel cell applications, where the electrodes are very susceptible to sulfur poisoning. The magnitudes of different streams that are processed globally are also quite different: for instance, over 120 trillion standard cubic feet (scf) of natural gas is produced each year, while only about 1 trillion scf of biogas is produced annually. The optimal materials and processes for H<sub>2</sub>S removal from different sources and for different end applications can be quite different. In this Review, we will focus more on the technical aspects of the different alternative methods and processes. Detailed economic analysis of competing H<sub>2</sub>S-removal processes for specific feeds and applications is beyond the scope of this Review. While there is a significant overlap in materials for different H<sub>2</sub>S-capture problems, we will base our discussions mainly in the context of natural gas purification.

Raw natural gas is a complex mixture of methane (CH<sub>4</sub>), ethane, and other light alkanes, H<sub>2</sub>S, carbon dioxide (CO<sub>2</sub>), nitrogen, and water (H<sub>2</sub>O) vapor. The U.S. Environmental Protection Agency classifies natural gas as *sour* at H<sub>2</sub>S concentrations above 4 ppm;<sup>5</sup> *sweetening* refers to removal of acidic sulfur compounds, primarily H<sub>2</sub>S. Natural gas emerging at the reservoir well head is subjected to low temperatures to condense out heavier hydrocarbons (see Figure 1). Overhead vapors are sent to the acid gas removal unit to selectively strip off H<sub>2</sub>S and CO<sub>2</sub>; amine-based absorption is most commonly used for this step. The H<sub>2</sub>S-rich stream is sent to the sulfur recovery unit (SRU), while the CH<sub>4</sub>-rich stream, after some post-processing steps such as dehydration, is sent to the pipeline as sales gas. In the SRU, sulfur is recovered by the well-known Claus process, where H<sub>2</sub>S undergoes high-temperature (~1000 °C) thermal oxidation,

**Table 2.** Properties and Compositions of Raw H<sub>2</sub>S-Containing Gases from Different Sources (Data from Refs 2–4)

parameter	unit	natural gas					biogas	landfill gas	syngas
		Ekofisk, Norway	Panhandle, US	Wustrow, Germany	Siid-Oldenburg, Germany	Tenguiz, USSR			
calorific value	MJ/N·m <sup>3</sup>	40	36	16	30	70	21–25	12–23	8–10
CH <sub>4</sub>	mol%	85	73.2	43	77	42	60–70	35–65	0–5
C <sub>2</sub> +	mol%	12.5	11.5	0.7	0.1	39			
CO <sub>2</sub>	mol%	2	0.3	0.3	8	2.6	30–40	15–40	5–15
H <sub>2</sub> S	mol%	0.001			8	16	0–0.4	0–0.01	0–0.01
N <sub>2</sub>	mol%	0.4	14.3	56	7	0.8	0–0.5	15	
H <sub>2</sub>	mol%								25–30
CO	mol%								30–60
NH <sub>3</sub>	ppm						100	5	
He	mol%		0.7	0.04					

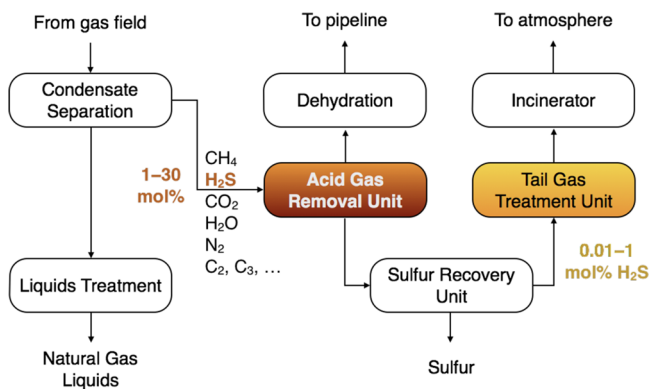
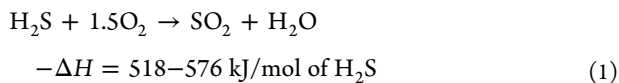
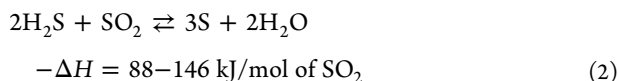


Figure 1. Block diagram for natural gas processing.



prior to low-temperature (200–300 °C) catalytic oxidation,



( $-\Delta H$  data from ref 6), in a series of reactors at progressively lower temperatures, accompanied by sulfur removal in intermediate condensers. Since the melting point of elemental sulfur is 115 °C and sulfur deposition leads to catalyst deactivation, the temperature of the final Claus reactor is generally maintained above 200 °C. This results in an incomplete conversion of H<sub>2</sub>S, and the resulting gas stream is sent to the tail gas treatment unit for additional sulfur recovery before the waste gases are released to the atmosphere. Thus, highly sour natural gas is usually processed for H<sub>2</sub>S removal in two different units, at two very different concentrations.

In addition to other papers in this special issue, *Chemical Reviews* has published three papers on the subject of CO<sub>2</sub> capture in the past 5 years: Sumida et al. reviewed CO<sub>2</sub> capture in metal–organic frameworks (MOFs),<sup>7</sup> Pera-Titus reviewed the capture process using porous inorganic membranes,<sup>8</sup> and Sanz-Pérez et al. focused on chemical sorbents for the direct capture of CO<sub>2</sub> from air.<sup>9</sup> However, similar reviews on H<sub>2</sub>S capture are few and limited in scope.<sup>10–16</sup> Abatzoglou and Boivin reviewed biogas purification processes for removal of contaminants such as H<sub>2</sub>S, NH<sub>3</sub>, and siloxanes.<sup>11</sup> They divided the purification methods into two generic categories: those involving physicochemical phenomena and those involving biological processes. Most biotechnologies still require further optimization and scale-up in order to compete with their physical/chemical counterparts.<sup>17</sup> We will focus here on the physicochemical techniques for selective H<sub>2</sub>S removal; the reader interested in microbiological alternatives is referred to earlier reviews on the subject.<sup>18,19</sup> The abundant literature available on H<sub>2</sub>S removal may be broadly classified into four categories: absorption, adsorption, membranes, and cryogenic distillation (see Figure 2). In this Review, we focus on materials and chemistries involved in each of these processes. Extensive review articles focus on solutions to tackle concentrated H<sub>2</sub>S by methods like the Claus process<sup>20–22</sup> or the production of hydrogen from H<sub>2</sub>S,<sup>23</sup> and these are not considered here.

Since H<sub>2</sub>S is a polar molecule, while CH<sub>4</sub> is a nonpolar molecule, it is obvious to imagine a polar solvent or a polar adsorbent surface to carry out this separation. However, the presence of other polar natural gas impurities such as H<sub>2</sub>O, which has a dipole moment about twice that of H<sub>2</sub>S, presents challenges to a simple polarity-based CH<sub>4</sub>/H<sub>2</sub>S separation. Exploiting the higher acidity of H<sub>2</sub>S compared to that of H<sub>2</sub>O using basic chemicals such as amines is also an alternative for sour gas sweetening. However, this principle of separation also suffers from some limitations due to the acidity of CO<sub>2</sub> being

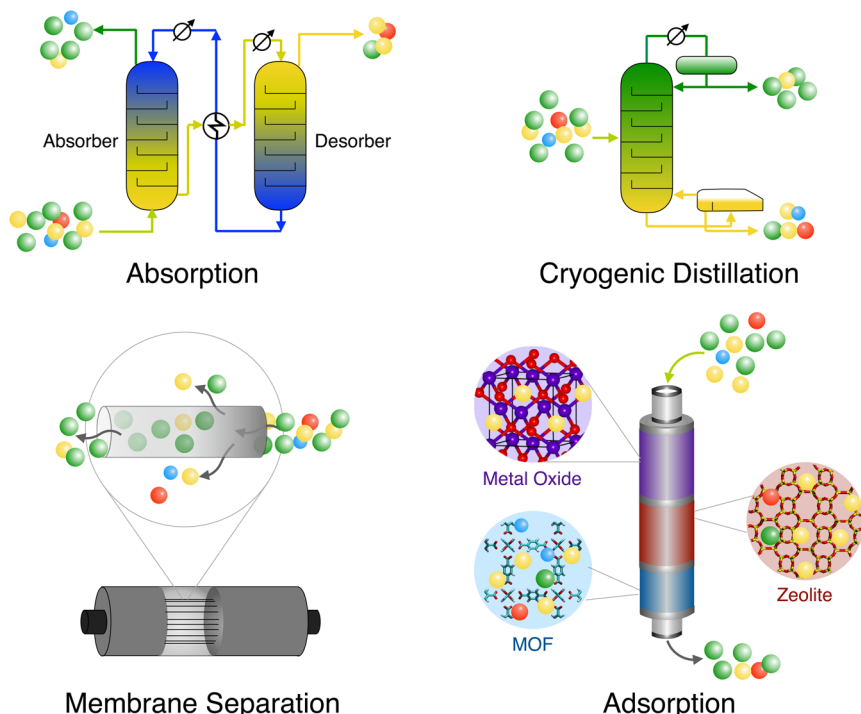


Figure 2. Different alternatives for sour gas sweetening.

higher than that of H<sub>2</sub>S and the concentration of CO<sub>2</sub> in natural gas being generally much higher than that of H<sub>2</sub>S. The kinetic diameter of CH<sub>4</sub> (3.8 Å) is slightly larger than that of H<sub>2</sub>S (3.6 Å); this might be another property that can be exploited for this particular gas separation using nanoporous adsorbents or membranes. Thus, while several possible solutions exist, challenges are associated with each of them, and it is important to evaluate these on a case-by-case basis.

## 2. ABSORPTION

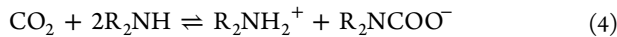
The natural gas industry has relied on gas absorption for purification of raw natural gas for nearly 100 years, and this separation technique dominates most sour gas separations around the globe even today. A variety of different liquid solvents have been employed in a tray or a packed-bed configuration to selectively absorb H<sub>2</sub>S and CO<sub>2</sub> from CH<sub>4</sub> and light alkanes. Depending on the strength of interaction of gas molecules with the solvent and the nature of the absorption isotherm, these solvents maybe broadly classified into chemical and physical categories. For chemisorption, solubility of the gas in the liquid increases sharply at very low pressures and starts to plateau at higher pressures; the plateau is indicative of the stoichiometric capacity for the chemical reaction. In physisorption, the plateau is shifted to much higher pressures, and in many cases there is no plateau for the pressure range of interest, so solubility continues to increase, more or less linearly, with pressure. A sharp distinction between these categories does not exist (e.g., hydrogen bonding and weak charge transfer), and in reality, all solute–solvent combinations have some contribution from physisorption. For sour gas sweetening, alkanolamines are the most widely used class of chemical solvents. All other solvents usually absorb the gas physically, and their very high capacities make them of interest if a feed with high acid gas partial pressure is available.

### 2.1. Alkanolamines

Bottoms for the first time, in 1930, developed an absorption process for acid gases using alkanolamine solutions.<sup>24</sup> For several years, diethanolamine (DEA) was commonly used in refineries to remove acid gases. However, not only do H<sub>2</sub>S and CO<sub>2</sub> concentrations in raw natural gas vary over a wide range of concentrations, but also since the toxicity of H<sub>2</sub>S is much higher than that of CO<sub>2</sub>, the upper-bound specifications for these impurities in the pipeline gas are also quite different (4 ppm for H<sub>2</sub>S and 2% for CO<sub>2</sub>). Clearly, the extent of H<sub>2</sub>S and CO<sub>2</sub> removal required can be very different too. For example, nearly complete removal of H<sub>2</sub>S without any major removal of CO<sub>2</sub> is desired for a feed gas containing high H<sub>2</sub>S concentration but CO<sub>2</sub> concentration being already at 2%. Traditional alkanolamines absorb CO<sub>2</sub> in preference to H<sub>2</sub>S; Frazier and Kohl first proposed the use of tertiary amines such as methyldiethanolamine (MDEA) for selective removal of H<sub>2</sub>S.<sup>25</sup> The CO<sub>2</sub>–tertiary amine reaction,



proceeding via the bicarbonate formation, is relatively slow compared with the CO<sub>2</sub>–primary and CO<sub>2</sub>–secondary amine reactions, resulting in a carbamate ion,



while the H<sub>2</sub>S–tertiary amine reaction, like all other amines, involves a proton transfer and is faster,<sup>26</sup>



MDEA not only offers kinetic selectivity toward H<sub>2</sub>S but also allows an equilibrium that favors the absorption of H<sub>2</sub>S over CO<sub>2</sub>.<sup>25,27</sup>

Besides MDEA, diisopropanolamine (DIPA), which is used in the Adip process developed by Shell, has also been reported to have a greater selectivity for H<sub>2</sub>S over CO<sub>2</sub> than either monoethanolamine (MEA) or DEA.<sup>28</sup> In 1983, Sartori et al. investigated 2-amino-2-methyl-1-propanol (AMP), a sterically hindered amine, for CO<sub>2</sub> removal at Exxon Research and Engineering Company.<sup>29</sup> Introducing steric hindrance by a bulky substituent adjacent to the amino group lowers the stability of the carbamate formed by the CO<sub>2</sub>–amine reaction. Using kinetic modeling, the authors described as to how decreased carbamate stability leads to higher thermodynamic CO<sub>2</sub> loadings approaching 1 mol of CO<sub>2</sub> per mole of amine. Additionally, this leads to a higher free-amine concentration; therefore fast CO<sub>2</sub>–amine reaction rates are obtained despite some reduction of the rate constant owing to steric interference. These hindered amines were found to be selective toward H<sub>2</sub>S over CO<sub>2</sub> and have been commercialized as the Flexsorb process by Exxon Research and Engineering Company. It is claimed that the new hindered amine-based processes are potentially attractive replacements for the existing selective H<sub>2</sub>S removal processes, including the MDEA-based process.<sup>28</sup>

Thorough knowledge of the vapor–liquid equilibria for a gas/liquid combination is a prerequisite for accurate design of absorption columns. Classical thermodynamic modeling of acid gas absorption in aqueous alkanolamines, using either semi-empirical equilibrium constant approaches or activity coefficient methods, has been a subject of interest since the 1930s. Recently, Suleman et al. reviewed these models, discussing their classification, chronological development, salient features, and recommendations of appropriate models depending on the pressure and loading of the acid gases.<sup>30</sup>

### 2.2. Methanol

The Rectisol process, developed independently by Linde and Lurgi in the late 1950s, involves physical absorption using methanol at temperatures between –40 and –60 °C. Since methanol has a low viscosity, it can be used for very low-temperature absorption processes, in particular for feeds with low partial pressures of acid gases. Since the high vapor pressure of methanol demands washing of all streams with liquid water in order to recover the methanol vapors, all streams are humidified during the process; the purified gas stream will also be humidified, thus requiring an additional step to meet the upper-bound H<sub>2</sub>O specifications for natural gas. The main application for the Rectisol process is purification of syngas derived from the gasification of heavy oil and coal rather than natural gas treating applications.<sup>31</sup> The multi-stage Ifpexol process, developed by Institut Francais du Petrole, can be used for natural gas applications.<sup>32</sup> Physical properties of various commercially used physical solvents for gas sweetening are listed in Table 3.<sup>33,34</sup>

### 2.3. N-Methyl-2-pyrrolidone

Like the Rectisol process, the Purisol process is also a physical absorption process based on N-methyl-2-pyrrolidone (NMP). However, due to its much lower vapor pressure, it can be operated at relatively higher temperatures without excessive solvent loss. Its operation at sub-ambient temperatures allows

**Table 3. Physical Properties of Common Sweetening Solvents**

	MeOH	NMP	PEGDME
process	Rectisol	Purisol	Selexol
viscosity at 25 °C (cP)	0.6	1.65	5.8
density at 25 °C (kg/m <sup>3</sup> )	785	1027	1030
molecular weight (g/mol)	32	99	280
vapor pressure at 25 °C (Pa)	16700	53	0.097
freezing point (°C)	-92	-24	-28
normal boiling point (°C)	65	202	275
maximum operating temperature (°C)	N/A	N/A	175
specific heat at 25 °C (cal/(g·°C))	0.566	0.40	0.49
H <sub>2</sub> S solubility at 25 °C (mol/L)	1.00	1.62	1.43
CO <sub>2</sub> solubility at 25 °C (mol/L)	0.142	0.159	0.162
CH <sub>4</sub> solubility at 25 °C (mol/L)	0.0072	0.011	0.011

for simultaneous water removal since water is not required to wash the treated gas stream for solvent (NMP) recovery. Various advantages and limitations of the Rectisol and Purisol processes are covered in great detail elsewhere.<sup>34,35</sup>

#### 2.4. Poly(ethylene glycol) Dimethyl Ether

Poly(ethylene glycol) dimethyl ether (PEGDME) is a mixture of  $\text{CH}_3\text{O}(\text{CH}_2\text{CH}_2\text{O})_n\text{CH}_3$  oligomers with  $n = 2-9$ . Compared to the other solvents, PEGDME has a higher viscosity, which reduces mass-transfer rates and tray efficiencies and increases packing or tray requirements, especially at reduced temperatures.<sup>34</sup> However, it benefits from lower solvent vapor pressure, which prevents solvent losses in various streams, thus eliminating the need for water wash to recover the solvent and allowing for simultaneous dehydration of the feed to the desired dew point of sales gas. The Selexol process, developed by Allied Chemical Corporation, was first utilized in 1970.

#### 2.5. Sulfolane and Diisopropanolamine

Unlike other physical solvents such as methanol, sulfolane are rarely used alone but rather in admixture with a chemical solvent such as an alkanolamine solution.<sup>36</sup> Shell Oil's Sulfinol process, first developed by Dunn et al. in 1964, employs a mixed solvent consisting of DIPA, sulfolane, and water.<sup>37</sup> The presence of the physical solvent appreciably enhances the solution capacity, especially when the gas stream to be treated is available at high pressure and the acidic components are present in high concentrations.<sup>38</sup> There have been several subsequent studies to improve the chemical solvent; one such candidate is MDEA, a tertiary amine that has thermodynamic and kinetic selectivity toward H<sub>2</sub>S in the presence of CO<sub>2</sub>.<sup>39-41</sup> Currently, three different solvents are available for the Sulfinol process: Sulfinol-X consists of MDEA and piperazine, Sulfinol-M consists of MDEA, and Sulfinol-D consists of DIPA.<sup>42</sup>

#### 2.6. Ionic Liquids

Ionic liquids (ILs) are salts having moderately low melting points (<100 °C), with their ionic character imparting them a large cohesive energy in the liquid phase, which in turn results in extremely low vapor pressures over a wide temperature range. This is a benefit for absorptive gas separation since the loss of solvent to the gas stream can be minimized. Additionally, many ILs are thermally very stable and are less combustible than other absorbents. Typically, an IL comprises a large, low-symmetry organic cation derived by alkyl substitution on parent cations such as imidazolium, pyridinium, ammonium, and phosphonium and an inorganic or organic anion such as

tetrafluoroborate, hexafluorophosphate, acetate, methyl sulfate, ethyl sulfate, triflate, etc.<sup>43</sup> Due to their polar character, ILs show a high affinity for polar molecules such as H<sub>2</sub>O, CO<sub>2</sub>, and H<sub>2</sub>S, while nonpolar molecules like CH<sub>4</sub> and other alkanes exhibit a much smaller solubility. In this section, we will discuss various advantages and shortcomings of ILs for H<sub>2</sub>S capture. The reader is also referred to earlier reviews on the subject.<sup>44-46</sup>

Jou and Mather first investigated H<sub>2</sub>S absorption in an IL, 1-N-butyl-3-methylimidazolium hexafluorophosphate ([bmim]<sup>+</sup>[PF<sub>6</sub><sup>-</sup>]), and observed that H<sub>2</sub>S only physisorbed to the IL.<sup>47</sup> This further suggests that ILs are unlikely to replace alkanolamines completely but may be useful either for the bulk removal of high-partial-pressure acid gases or for mixing with a chemical solvent to increase capacity. Pomelli et al. extended this investigation to a wide range of cations and anions and demonstrated ILs with extremely high H<sub>2</sub>S solubilities.<sup>62</sup> They also carried out gas-phase electronic structure calculations elucidating the strong binding of H<sub>2</sub>S to the anion of the IL, with interaction energies of these complexes in the range of 30–60 kJ/mol, indicating traditional hydrogen bonds. Experimental data for the Henry's law constants for H<sub>2</sub>S, CO<sub>2</sub>, and CH<sub>4</sub> in various ILs are summarized in Table 4.

**Table 4. Henry's Law Constants for H<sub>2</sub>S, CO<sub>2</sub>, and CH<sub>4</sub> in Ionic Liquids**

ionic liquid	T (°C)	Henry's law constant (bar)			reference
		H <sub>2</sub> S	CO <sub>2</sub>	CH <sub>4</sub>	
[bmim] <sup>+</sup> [PF <sub>6</sub> <sup>-</sup> ]	25	14	53.4	1700	47, 48
[bmim] <sup>+</sup> [Tf <sub>2</sub> N] <sup>-</sup>	30	13	33		44, 49
	40			500	50
[bmim] <sup>+</sup> [BF <sub>4</sub> <sup>-</sup> ]	30	16	61.6	840	49, 51
hmim <sup>+</sup> [PF <sub>6</sub> <sup>-</sup> ]	30	18			52
[hmim] <sup>+</sup> [Tf <sub>2</sub> N] <sup>-</sup>	30	17	31.6	350	52, 53
[hmim] <sup>+</sup> [BF <sub>4</sub> <sup>-</sup> ]	30	12			52
[hemim] <sup>+</sup> [PF <sub>6</sub> <sup>-</sup> ]	30	28			54
[hemim] <sup>+</sup> [Tf <sub>2</sub> N] <sup>-</sup>	30	19			
[hemim] <sup>+</sup> [BF <sub>4</sub> <sup>-</sup> ]	30	31	108		54, 55
[emim] <sup>+</sup> [PF <sub>6</sub> <sup>-</sup> ]	80	47			56
[emim] <sup>+</sup> [Tf <sub>2</sub> N] <sup>-</sup>	30	15	37	570	53, 56
[emim] <sup>+</sup> [EtSO <sub>4</sub> <sup>-</sup> ]	30	60			57
[hmim] <sup>+</sup> [Tf <sub>2</sub> N] <sup>-</sup>	30	12			58
[omim] <sup>+</sup> [Tf <sub>2</sub> N] <sup>-</sup>	30	10	24		
[emim] <sup>+</sup> [Ac <sup>-</sup> ]	30	1.2			59
[emim] <sup>+</sup> [Pro <sup>-</sup> ]	30	0.85			
[emim] <sup>+</sup> [Lac <sup>-</sup> ]	30	1.4			
[bmim] <sup>+</sup> [Ac <sup>-</sup> ]	30	0.90			
[hmim] <sup>+</sup> [Ac <sup>-</sup> ]	30	0.85			
[MDEAH][Ac]	30	5.5	49		60
[MDEAH][For]	30	11.5	117		
[DMEA][Ac]	30	3.5	53		
[DMEA][For]	30	5.9	115		
[BDMAEE][Tf <sub>2</sub> N]	25	2.47	29		61

Since sorption experiments are much more difficult to conduct for gas mixtures than for pure gases, an assumption needs to be invoked for defining absorption selectivity. There are at least two possible ways to define ideal absorption selectivity that have been used in the literature: (i) ratio of the solubilities at infinite dilution (Henry's law coefficients) and (ii) computing a mixture selectivity,

$$S_{ij} = \frac{x_i/x_j}{y_i/y_j} \quad (6)$$

assuming that the amount absorbed for a mixture at a given partial pressure is equal to that for a pure case at the same total pressure. The answers obtained from the two definitions can be quite different. In order to assess the validity of ideal absorption selectivity approximation, Singh et al.<sup>63</sup> carried out molecular simulations for mixture absorption of CO<sub>2</sub>/H<sub>2</sub> in [C<sub>4</sub>mim<sup>+</sup>]-[Tf<sub>2</sub>N<sup>-</sup>] and [C<sub>8</sub>mim<sup>+</sup>][Tf<sub>2</sub>N<sup>-</sup>] and found that definition (ii) for selectivity is in much better agreement with mixture selectivity. For CO<sub>2</sub>/CH<sub>4</sub> absorption in [C<sub>4</sub>mim<sup>+</sup>][Tf<sub>2</sub>N<sup>-</sup>], Budhathoki et al. observed definition (i) to be in better agreement with the mixture selectivity.<sup>64</sup> These differences demonstrate a lack of quantitative predictive capabilities to determine mixture absorption from pure-component data and suggest that either mixture measurements or mixture simulations with reliable force fields should indeed be carried out for at least the more promising ILs.

Trends in affinity of H<sub>2</sub>S toward the anion of the IL were found to depend on the cation under consideration: [emim<sup>+</sup>]-[Tf<sub>2</sub>N<sup>-</sup>] > [emim<sup>+</sup>][PF<sub>6</sub><sup>-</sup>]<sup>56</sup> [bmim<sup>+</sup>][Tf<sub>2</sub>N<sup>-</sup>] > [bmim<sup>+</sup>]-[BF<sub>4</sub><sup>-</sup>] > [bmim<sup>+</sup>][PF<sub>6</sub><sup>-</sup>]<sup>49</sup> [hmim<sup>+</sup>][BF<sub>4</sub><sup>-</sup>] > [hmim<sup>+</sup>][PF<sub>6</sub><sup>-</sup>] ≈ [hmim<sup>+</sup>][Tf<sub>2</sub>N<sup>-</sup>]<sup>52</sup> and [hemim<sup>+</sup>][Tf<sub>2</sub>N<sup>-</sup>] ≥ [hemim<sup>+</sup>]-[OTf<sup>-</sup>] > [hemim<sup>+</sup>][PF<sub>6</sub><sup>-</sup>] > [hemim<sup>+</sup>][BF<sub>4</sub><sup>-</sup>].<sup>54</sup> These results indicate that H<sub>2</sub>S solubility is affected by both the cation and the anion of the IL, and it may not be possible to find the best anion and the best cation without trying all possible pairs. With the aid of molecular simulations, deeper insights can be gained about the entropic and enthalpic contributions of H<sub>2</sub>S solubilities in different ILs. Recently, Sánchez-Badillo and co-workers computed solvation thermodynamics of H<sub>2</sub>S in ILs and demonstrated qualitative agreement with experimental data.<sup>65</sup> These calculations showed that, at room temperature, the absolute solvation enthalpy is 2 times higher than the absolute entropic contribution for [bmim<sup>+</sup>][PF<sub>6</sub><sup>-</sup>] and [bmim<sup>+</sup>][BF<sub>4</sub><sup>-</sup>] and 3 times higher for [bmim<sup>+</sup>][Cl<sup>-</sup>]. The solubility of H<sub>2</sub>S in [bmim<sup>+</sup>][Tf<sub>2</sub>N<sup>-</sup>] from molecular simulations was shown to be sensitive to the choice of the H<sub>2</sub>S force field; the TraPPE model resulted in the most accurate predictions.<sup>66,67</sup> Jalili et al. also studied [C<sub>8</sub>mim<sup>+</sup>][Tf<sub>2</sub>N<sup>-</sup>] and found that the solubility of H<sub>2</sub>S in [C<sub>n</sub>mim<sup>+</sup>][Tf<sub>2</sub>N<sup>-</sup>] ILs increases as the number of carbon atoms in the alkyl substituent of the methylimidazolium cation, *n*, increases.<sup>58</sup> The authors explained that since the molar volume of the IL increases with *n*, possibly due to poorer interactions between bulkier cations and the anion, higher free volumes may result, in turn increasing the solubility. One must remember that such increased acid gas solubility due to increased free volumes will also lead to increased CH<sub>4</sub> solubility, in turn reducing S<sub>H<sub>2</sub>S/CH<sub>4</sub></sub>. As described previously with regard to how the necessity for selective H<sub>2</sub>S over CO<sub>2</sub> absorption led to the development of absorbents such as MDEA, new solvents with S<sub>H<sub>2</sub>S/CO<sub>2</sub></sub> > 1 that also exert a low vapor pressure to reduce solvent losses will be interesting targets, and ILs, with their tunable polarity, can be groundbreaking candidates to achieve this selectivity.<sup>68</sup> Investigations of ternary systems consisting of H<sub>2</sub>S, CO<sub>2</sub>, and [C<sub>8</sub>mim<sup>+</sup>]-[Tf<sub>2</sub>N<sup>-</sup>] showed S<sub>H<sub>2</sub>S/CO<sub>2</sub></sub> ≈ 3 under ambient pressure and temperature.<sup>58</sup>

All the studies conducted so far focused only on H<sub>2</sub>S and not on CH<sub>4</sub> absorption. After all, for gas sweetening, selectivity is more important than solubility alone. Carvalho et al. suggested

that the solubility of H<sub>2</sub>S in ILs is governed predominantly by entropic effects and that the most promising approach to enhance the sour gases/CH<sub>4</sub> selectivities at high pressures is by lowering the methane solubility in ILs and not by increasing the sour gas solubility, which is essentially dependent on the solvent molar volume.<sup>69</sup> These authors measured CH<sub>4</sub> solubility in four different ILs and demonstrated that it was highly dependent on the polarity of the IL and that, contrary to the previous selectivity models in the literature,<sup>70,71</sup> the molar volume of the IL alone was not a sufficient criterion to tune selectivity.<sup>72</sup>

While high solubility and selectivity for the desired molecule form the prerequisites for an IL to be useful for separation purposes, additional criteria such as thermal and mass transport through the IL can also contribute to the overall operating cost of the absorber. Due to their high cohesive energies, ILs demonstrate high viscosities, 1–3 orders of magnitude higher than for the conventional solvents.<sup>73</sup> Higher viscosities imply higher power consumption for gas–liquid contact, but also an unusual possibility for diffusion-based selectivity in a gas–liquid system. Under such circumstances, it will be helpful if the diffusivity of H<sub>2</sub>S is higher than that of CO<sub>2</sub> in order to benefit from a transport selectivity. Reports investigating the diffusion of acid gases in ILs are limited.<sup>55,57,74</sup> At room temperature, [emim<sup>+</sup>][EtSO<sub>4</sub><sup>-</sup>] shows a high diffusion selectivity,  $\mathcal{D}_{\text{H}_2\text{S}/\text{CO}_2} \approx 40$ , while [hemim<sup>+</sup>][BF<sub>4</sub><sup>-</sup>] shows  $\mathcal{D}_{\text{H}_2\text{S}/\text{CO}_2} \approx 1$ .

In 2002, Bates et al. first reported an IL designed for CO<sub>2</sub> capture (task-specific ionic liquids (TSILs)) where a primary amine moiety is covalently tethered to an imidazolium cation for enhanced interaction with CO<sub>2</sub>.<sup>75</sup> Huang et al. employed carboxylate-based ILs for H<sub>2</sub>S capture, the Lewis base character of which resulted in higher absorption capacities.<sup>59</sup> These ILs absorb about 0.3 mol of H<sub>2</sub>S per mole of IL under ambient pressure at 60 °C, about 15 times higher than conventional ILs. The enthalpy of this reactive absorption varies between 30 and 65 kJ/mol, depending on the cation and the anion, but is still lower than typical enthalpies of absorption in alkanolamines (≥80 kJ/mol). However, in spite of these favorable characteristics, the S<sub>H<sub>2</sub>S/CO<sub>2</sub></sub> in the carboxylate ILs is even worse than in the normal ILs due to the strong affinity of carboxylate ions toward CO<sub>2</sub>.<sup>76</sup> This challenge was overcome with the design of dual Lewis base functionalized ILs (DLB-ILs),<sup>77</sup> which have a tertiary amine group tethered to the carboxylate anion. It was found that the DLB-ILs could reversibly absorb 0.39–0.84 mol of H<sub>2</sub>S per mole of IL at 1 bar and 60 °C, which is significantly higher than for other ILs. These DLB-ILs show S<sub>H<sub>2</sub>S/CO<sub>2</sub></sub> ≈ 20 at 1 bar and S<sub>H<sub>2</sub>S/CO<sub>2</sub></sub> > 100 at pressures less than 0.1 bar. Density functional theory (DFT) calculations demonstrated the favorable geometry and energetics of the carboxylate–H<sub>2</sub>S–amine complex and the reduced CO<sub>2</sub>–IL binding.

Although TSILs can be modified for high H<sub>2</sub>S capacity and S<sub>H<sub>2</sub>S/CO<sub>2</sub></sub>, their high costs and viscosity disfavor their application in industry.<sup>60</sup> This limitation encouraged the same authors to explore protic ionic liquid (PILs), which are a class of low-cost ILs that can be easily prepared from simple materials through direct neutralization between the corresponding acid and base.<sup>60,78</sup> For instance, mixing dimethylethanolamine and acetic acid yields dimethylethanolammonium acetate ([DMEA]·[Ac]). It was demonstrated that [DMEA]·[Ac] and dimethylethanolammonium formate ([DMEA]·[For]) have S<sub>H<sub>2</sub>S/CO<sub>2</sub></sub> greater than those of normal ILs and any other organic solvent.

Another issue with TSILs is that they are highly hydrophilic and miscible with water, thus increasing the expense of regeneration by requiring energy for removing bound water. Both the cation and anion can affect the mutual solubilities between water and ILs, but the anion plays the major role in determining their phase behavior.<sup>79</sup> Huang et al.<sup>61</sup> synthesized half-protonated diamines with a free tertiary amine group (disfavoring CO<sub>2</sub>) tethered on the cations and bis(trifluoromethylsulfonyl)imide ([Tf<sub>2</sub>N<sup>-</sup>]) as the anion, which is a well-known building block for hydrophobic ILs with low viscosity.<sup>79</sup> Although these ILs have H<sub>2</sub>S absorption capacity similar to that of other TSILs reported in the literature on a mole ratio basis, they have a molecular weight nearly twice that of other TSILs, making capacity on molality basis (per mass of IL) nearly half.

As described earlier, compared to common organic solvents with high vapor pressures, ILs contribute negligible volatile organic compounds to the atmosphere, thus reducing the issue of atmospheric emissions. However, it has been noted in the literature that most ILs are not intrinsically “green”,<sup>80</sup> and similar to other commercial organic solvents, irresponsible release of them will pose a threat to the environment. One of the key issues here is that, unlike the common solvents, the toxicity of ILs is not fully characterized. However, at least in principle, the large design space of ILs should allow for designing solvents that not only are effective for the application of interest but also pose no serious ecological threat. In an attempt to explore environmentally benign solvents, Guo et al. synthesized and measured H<sub>2</sub>S absorption in a series of caprolactam tetrabutylammonium bromide (CPL-TBAB) ILs with different mole ratios of CPL and TBAB.<sup>81</sup> For the 1:1 CPL-TBAB mixture, the solubilities of pure H<sub>2</sub>S at atmospheric pressure are 0.69 and 0.44 mol of H<sub>2</sub>S per mole of IL at 30 and 90 °C, respectively.

Heldebrant et al. developed a new class of CO<sub>2</sub>-binding organic liquids (CO<sub>2</sub>BOLs) that chemically and reversibly absorb CO<sub>2</sub>.<sup>82</sup> These organic liquids are mixtures of organic alcohols and amidine/guanidine bases. Since these organic liquids have lower specific heats compared to H<sub>2</sub>O and also since they require much lower regeneration temperatures, a higher energy efficiency can be achieved during absorption/regeneration cycles. Following on the capture of acid gases such as CO<sub>2</sub>, SO<sub>2</sub>, CS<sub>2</sub>, and COS using such organic liquids,<sup>82,83</sup> it was hypothesized that weak bases such as tertiary alkanolamines (anhydrous) could react with H<sub>2</sub>S to form liquid hydrosulfide salts that could be used as reversible H<sub>2</sub>S-binding organic liquids (H<sub>2</sub>SBOLs).<sup>84</sup> These authors demonstrated desorption of H<sub>2</sub>S by either inert gas sparging or mild heating, or even at room temperature by the addition of low-specific-heat antisolvents such as hexanes that can be boiled at 50–70 °C. BOLs are non-ionic before reacting with the gas molecule; however, after chemically reacting with the gas, they become ILs.

Very similar in properties to ILs, deep eutectic solvents (DESs) are a relatively new class of solvents that are formed by complexing a large, asymmetric quaternary ammonium salt with a metal salt or a hydrogen bond donor.<sup>85</sup> Hydrogen bonding in the system results in charge delocalization, thus lowering the lattice energy and decreasing the melting point of the mixture relative to the melting points of the individual components.<sup>86</sup> In addition to most of the better solvent properties of ILs, DESs are generally more biodegradable, less toxic, and inexpensive, thus making these solvents more sustainable. Articles on CO<sub>2</sub> capture using DESs have started to appear in

the past few years,<sup>87,88</sup> and CO<sub>2</sub> removal from natural gas was reviewed recently.<sup>89</sup> To the best of our knowledge, there is no report in the literature on H<sub>2</sub>S capture, and this might be an unexplored opportunity to discover novel solvents for this application.

Since 2010, several research groups have started to focus on equations of state (EoS) modeling of H<sub>2</sub>S + ILs phase behavior.<sup>90–98</sup> A major drawback in the use of the most prevalent cubic EoS is that they require critical parameters of the ILs that can only be obtained indirectly and with large uncertainties, limiting their utility to correlation purposes only.<sup>99</sup> In contrast, contributions from various energetic interactions, such as dipole–dipole, quadrupole–quadrupole, and dipole–quadrupole, can be explicitly included in a class of equations based on the statistical associating fluid theory (SAFT) formalism.<sup>90,92</sup> Several other correlation techniques that use molecular weight, critical temperature and pressure, andacentric factor as input variables have been applied to H<sub>2</sub>S absorption in ILs.<sup>100–103</sup> Group contribution methods, requiring only the number and type of each fragment type as the input, were used to establish a comprehensive database on the solubility of H<sub>2</sub>S in ILs using 1334 pieces of data covering the period from 2007 to 2016.<sup>104</sup>

Lei et al. employed the conductor-like screening model for real solvents (COSMO-RS) to predict the solubilities of different gases, including H<sub>2</sub>S, in ILs and observed deviations of less than 40%.<sup>43</sup> This approach requires only the molecular structure and is independent of any experimental correlation. In another study, Mortazavi-Manesh et al. used COSMO-RS to screen 425 ILs for sour gas separations and, based on binary selectivities, suggested 58 promising ILs with H<sub>2</sub>S/CH<sub>4</sub>, H<sub>2</sub>S/C<sub>2</sub>H<sub>6</sub>, and H<sub>2</sub>S/CO<sub>2</sub> selectivities in the ranges 51–75, 11–23, and 2.6–3.4, respectively.<sup>105</sup>

In 1977, Tennyson and Schaaf provided some guidelines for the choice of appropriate physical/chemical solvent depending on the partial pressures of acid gases in the feed and product gas streams.<sup>106</sup> Process optimization for absorption using ILs in comparison to the commercial solvents can help identify the partial pressure regimes under which certain ILs may be preferred over conventional solvents. The past decade has seen several reports demonstrating high H<sub>2</sub>S–IL affinities, but ILs for selective acid gas removal are still in the design stage. Several design variables, such as length of the alkyl chains on the cation, branching of the alkyl chain, task-specific functional groups, pairing with appropriate anions, etc., make this a multi-dimensional combinatorial problem. As is shown in several fundamental studies for discovery of novel solid adsorbents, insights from molecular simulations can potentially speed up discovery of optimal ILs and DESs for H<sub>2</sub>S capture. Additionally, simulations can also help understand the differences between selectivities calculated from pure-component absorption isotherms and those observed in an actual mixture measurement. In conclusion, while ILs enjoy clear advantages such as design flexibility and negligible vapor pressures, properties such as viscosity, diffusivity, thermal conductivity, and reaction kinetics in ILs under varying temperatures and partial pressures of acid gases require thorough investigations in order to compare these new solvents with the conventional solvents that have been successfully commercialized for several decades.

### 3. ADSORPTION

Adsorptive separation involves the use of a selective and high-capacity solid substrate that shows a preferential affinity for one or more molecule types from their mixtures. Similar to absorption, adsorption may also be classified as physisorption and chemisorption, depending on the strength of sorbate–sorbent interactions. In addition to interaction-based separation, different sizes and shapes of molecules can also be exploited for selective removal of one compound over another. In this section, we will discuss a variety of adsorbents, such as metal oxides, MOFs, zeolites, carbons, and composite materials, for H<sub>2</sub>S capture from gas mixtures containing CH<sub>4</sub>, CO<sub>2</sub>, N<sub>2</sub>, H<sub>2</sub>, and/or H<sub>2</sub>O. For any adsorption application, it is desirable that the adsorbent has a high separation selectivity for the molecule of interest (primarily H<sub>2</sub>S in this case) and also a high capacity for the adsorbate. In addition to capacity and selectivity, stability under extreme acid gas environments as well as performance and structural regenerability are important for longer lifetime of the adsorbent bed.

#### 3.1. Metal Oxides

Since the 1960s, metal oxides have been used for desulfurization of coal gas, syngas, hydrogen for fuel cells, and Claus tail gas.<sup>107,108</sup> Metal oxides for hot-gas desulfurization have been investigated extensively;<sup>109,110</sup> this large body of literature is beyond the scope of this Review, and we focus here mostly on low to moderate temperatures (25–300 °C) that are of relevance to natural gas sweetening, including the Claus tail gas.

In 1976, Westmoreland and Harrison screened for the high-temperature (400–1200 °C) desulfurization potential of oxides of 28 elements with computational free energy minimizations of a C-H-N-O-S elemental system in the presence of the metal oxide using temperature-dependent free energies from the literature.<sup>111</sup> Eleven candidate solids, based upon the metals Fe, Zn, Mo, Mn, V, Ca, Sr, Ba, Co, Cu, and W, showed thermodynamic feasibility (at least 95% desulfurization and solid stability) for high-temperature desulfurization. Another simulation study at 400 °C with feed containing 12.5% CO<sub>2</sub>, 42.5% CO, 32.175% H<sub>2</sub>, 12.5% H<sub>2</sub>O, and 3250 ppm H<sub>2</sub>S showed that oxides of Zn, Mo, Mn, W, Sn, Co, Cu, Ni, and Fe should be successful in reducing the residual H<sub>2</sub>S content to 0.03, 0.6, 2.5, 3.4, 19, 24, 39, 41, and 91 ppm, respectively.<sup>112</sup>

Rodriguez et al. studied adsorption of H<sub>2</sub>S on a series of metal oxide surfaces using synchrotron-based high-resolution photoemission.<sup>113,114</sup> It was observed that the smaller the band gap in the oxide, the bigger its reactivity toward S-containing molecules (see Figure 3). *Ab initio* self-consistent field (SCF) theory calculations and experimental data indicated that the reactivity of an oxide mainly depends on how well its bands mix with the orbitals of H<sub>2</sub>S or HS.<sup>113</sup> Oxides possessing a large ionicity, like Al<sub>2</sub>O<sub>3</sub> and MgO, displayed the lowest reactivity toward H<sub>2</sub>S, indicating that the electrostatic interactions between the dipole of H<sub>2</sub>S and the ionic field generated by the charges in an oxide may play only a secondary role in the adsorption process.<sup>114</sup> As can be seen from Figure 3, Cr<sub>3</sub>O<sub>4</sub> interacts strongly with H<sub>2</sub>S. Even before this study, the most significant evolution of the Claus process, the Superclaus process, employed an  $\alpha$ -alumina support coated with a mixture of iron and chromium oxides as the catalyst.<sup>115</sup> However, due to the severe toxicity of chromia, continuing research to develop new catalysts for this important reaction is underway.<sup>116</sup> CuO and Cu<sub>2</sub>O have band gaps of 1.2 and 2.1 eV, respectively; the contribution by Rodriguez et al. should imply

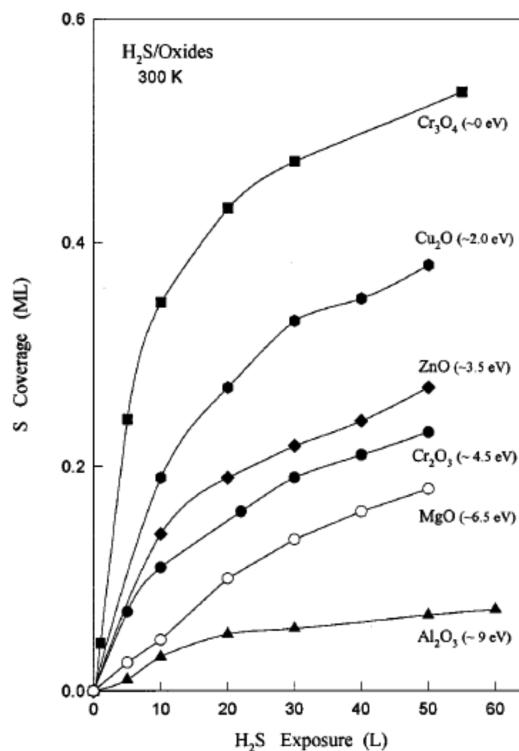


**Figure 3.** Total coverage of sulfur (S + SH) as a function of H<sub>2</sub>S exposure at 300 K on Al<sub>2</sub>O<sub>3</sub>, MgO,  $\alpha$ -Cr<sub>2</sub>O<sub>3</sub>(0001), ZnO, Cu<sub>2</sub>O, and Cr<sub>3</sub>O<sub>4</sub>(111). One monolayer (ML) corresponds to the deposition of  $1.43 \times 10^{15}$  atoms/cm<sup>2</sup>. The numbers in parentheses denote the band gap of each oxide. Reprinted with permission from ref 114. Copyright 1999 AIP Publishing.

better desulfurization using CuO compared to Cu<sub>2</sub>O. Room-temperature experimental screening of oxides of Ag, Cu, Zn, Co, Ni, Ca, Mn, and Sn showed a conversion of 66% for CuO but <10% for the other oxides.<sup>117</sup>

Several DFT studies on H<sub>2</sub>S reaction with oxides of Zn,<sup>118,119</sup> Fe,<sup>120</sup> Ce,<sup>121</sup> Ti,<sup>122</sup> Mn,<sup>123</sup> V,<sup>124,125</sup> Cu,<sup>126,127</sup> Co,<sup>128</sup> and Mg<sup>129</sup> have been carried out in the past decade. While these studies provide some details of possible reaction mechanisms for each metal oxide, a comparative study of different pure and mixed oxides for adsorption and regeneration from first-principles calculations, at the same level of theory, can provide insights into optimal metal oxide selection. Jia et al. carried out a comparative study of the reactions of M<sub>m</sub>O<sub>n</sub><sup>−</sup> (M = Fe, Co, Ni, Cu, and Zn) with H<sub>2</sub>S using mass spectrometry and DFT calculations.<sup>130</sup> The authors tested several density functionals by calculating the bond enthalpies of M–O, M–S, HS–H, and S–H species, and except for Zn–S, the B3LYP functional was found to be generally in better agreement with the experimental enthalpies.

Adsorption of H<sub>2</sub>S by ZnO is stoichiometric at 350 °C but falls off rapidly as the temperature is reduced.<sup>131</sup> Since this is an exothermic reaction, this decline in conversion is due to slower reaction kinetics. Baird et al. reported 91% conversion of Co<sub>3</sub>O<sub>4</sub> at room temperature,<sup>132</sup> while Xue et al. reported only a 1% conversion.<sup>117</sup> These studies suggest the possible implications of synthesis recipes on the size, shape, and surface area of the metal oxide particles that can, in turn affect the H<sub>2</sub>S breakthrough capacity. In fact, there are several reports exploring desulfurization using different ZnO morphologies.<sup>133–138</sup> While it is hard to draw a head-to-head comparison

**Table 5.** BET Surface Areas and Percentage Utilization in ZnO for H<sub>2</sub>S Adsorption

morphology	<i>S</i> <sub>BET</sub> (m <sup>2</sup> /g)	% utilization	<i>T</i> (°C)	composition	reference
imp-ZnO, 25–600 nm	3.1	0.29	<200	H <sub>2</sub> S in N <sub>2</sub>	Baird et al. <sup>131</sup>
cp-ZnO, 10–100 nm	37	3.7			
cp-ZnO, 20–50 nm	39	14	30	2% H <sub>2</sub> S in N <sub>2</sub>	Baird et al. <sup>132</sup>
44 nm, commercial	3.9	1.4	25	N/A	Carnes et al. <sup>133</sup>
33 nm, commercial	20	1.9			
4 nm, nanocrystalline	130	24			
		29	100		
		42	250		
64 × 283 nm, rod-like	12	57	250	0.5–1% H <sub>2</sub> S, 59% CH <sub>4</sub> in He	Habibi et al. <sup>134</sup>
		49	150		
56 nm, spherical	50	22	250		
		8.3	150		
4000 nm, commercial	45	38	200	1% H <sub>2</sub> S in He	Garcés et al. <sup>135</sup>
	34	69	300		
Zn(acac) <sub>2</sub> , microwave	52	38	200	1% H <sub>2</sub> S in He	Garcés et al. <sup>136</sup>
Zn(acac) <sub>2</sub> , heat	14	11			
Zn(NO <sub>3</sub> ) <sub>2</sub> , heat	14	5.1			

between independent studies due to different gas velocities, reactor volume, feed compositions, and definitions of breakthrough concentration, data for these are compiled in Table 5. The % utilization for a metal oxide-based adsorbent is defined as the ratio of the actual amount of H<sub>2</sub>S adsorbed to the theoretical amount of H<sub>2</sub>S adsorbed by complete conversion of metal oxide to metal sulfide, multiplied by 100. Note that the value can change depending on the choice of the oxidation state of the metal in its oxide and sulfide forms. This number can be greater than 100 due to H<sub>2</sub>S adsorbing without chemical reaction with the metal oxide (see, for instance, the H<sub>2</sub>S adsorption on metal oxides impregnated on high-surface-area silica supports).

The reaction between H<sub>2</sub>S and a metal oxide in the absence of O<sub>2</sub> belongs to the class of non-catalytic gas–solid reactions. These reactions have been most commonly analyzed using either the unreacted shrinking core model (USCM)<sup>139</sup> or the grain model.<sup>140</sup> USCM is built on the assumption that the reaction is much faster than the diffusion and, hence, the reaction occurs at the solid reactant surface. This model clearly assumes inward propagation of the reaction front. In the grain model, each of the large number of spherical grains in a solid pellet is assumed to react independently according to the USCM. Early reports on sulfidation kinetics of ZnO, employing the grain model with constant or varying properties (size changes due to sintering and reaction) of the adsorbent, agreed quantitatively with experiments.<sup>141,142</sup>

From the time when empirical commercialization of ZnO as a desulfurization sorbent took precedence until the early 1990s, very little was known about the structural changes and the mechanism for this reaction. Using *in situ* sulfur K-edge X-ray absorption spectroscopy (XAS) in the soft X-ray region (<5000 eV), Evans and co-workers first showed that the reaction of ZnO and H<sub>2</sub>S occurs via island formation of ZnS on the oxide surface and, as the reaction proceeds, eventually bulk regions of ZnS are formed.<sup>143,144</sup> Since there was no apparent shift in the edge energies of the S K-edge spectra, it was concluded that the

oxidation state of the sulfur remains as S<sup>2−</sup> throughout the process.<sup>143</sup> The X-ray photoelectron spectroscopy (XPS) and X-ray diffraction (XRD) data for the final states of the adsorbent confirmed the theory of a two-phase material consisting of crystalline ZnO (wurtzite) and a less ordered phase of ZnS (wurtzite), in spite of the fact that ZnS blend structure is thermodynamically more stable.<sup>144</sup> The reader is also referred to a review paper by Samokhvalov et al. on the low-temperature desulfurization using ZnO.<sup>145</sup>

Until recently, ZnO sulfidation models assumed inward diffusion of H<sub>2</sub>S, but Neveux et al. showed evidence for an outward growth mechanism (see Figure 4).<sup>146,147</sup> Using

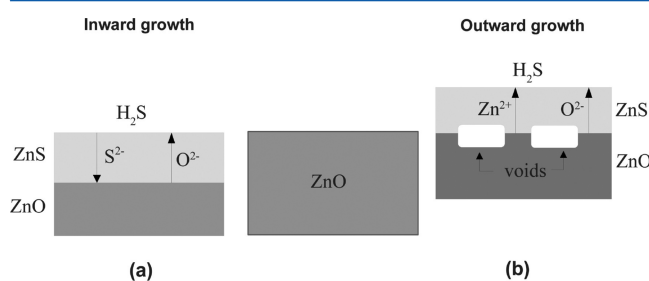


**Figure 4.** Two mechanisms of ZnS growth starting from pure ZnO (center): (a) inward ZnS growth and (b) outward ZnS growth. Reprinted with permission from ref 150. Copyright 2012 American Chemical Society.

transmission electron microscopy (TEM) and electron tomography, the authors observed voids inside the ZnS particle, suggesting that the Zn<sup>2+</sup> and O<sup>2−</sup> species diffuse through the product ZnS layer. Since the external particle surface increases during the course of the reaction, the decrease in reaction rate with time cannot be explained if the rate-determining step (RDS) is located at the external surface (adsorption, desorption, external interface reaction). Thus, the authors proposed that diffusion through the ZnS layer is most likely to be the RDS. Eight elementary steps of the sulfidation

**Table 6.** BET Surface Areas and Percentage Utilization in Mixed Zinc-Based Metal Oxides for H<sub>2</sub>S Adsorption

adsorbent	S <sub>BET</sub> (m <sup>2</sup> /g)	% utilization	T (°C)	composition	reference
ZnO	29	10	200	0.2% H <sub>2</sub> S, 49.9% H <sub>2</sub> , 49.9% N <sub>2</sub>	Skrzypski et al. <sup>148</sup>
Cu <sub>0.03</sub> Zn <sub>0.97</sub> O	44	47			
Cu <sub>0.06</sub> Zn <sub>0.94</sub> O	—	61			
ZnO	29	28	250		
Cu <sub>0.03</sub> Zn <sub>0.97</sub> O	44	70			
Cu <sub>0.06</sub> Zn <sub>0.94</sub> O	—	76			
ZnO	29	71	350		
Cu <sub>0.03</sub> Zn <sub>0.97</sub> O	44	79			
cp-ZnO	36	12	40	0.3% H <sub>2</sub> S in N <sub>2</sub>	Jiang et al. <sup>149</sup>
cp-Cu <sub>33.3</sub> Zn <sub>66.7</sub>	67	22			
cp-Cu <sub>67.7</sub> Zn <sub>33.3</sub>	54	32			
cp-Cu <sub>88.9</sub> Zn <sub>11.1</sub>	48	38			
cp-CuO	27	41			
cp-Zn <sub>90</sub> Al <sub>10</sub>	82	17			
cp-Cu <sub>30</sub> Zn <sub>60</sub> Al <sub>10</sub>	93	25			
cp-Cu <sub>60</sub> Zn <sub>30</sub> Al <sub>10</sub>	76	39			
cp-Cu <sub>80</sub> Zn <sub>10</sub> Al <sub>10</sub>	61	52			
cp-Cu <sub>90</sub> Al <sub>10</sub>	46	74			
mp-Zn <sub>90</sub> Al <sub>10</sub>	61	13			
mp-Cu <sub>30</sub> Zn <sub>60</sub> Al <sub>10</sub>	93	30			
mp-Cu <sub>60</sub> Zn <sub>30</sub> Al <sub>10</sub>	98	48			
mp-Cu <sub>80</sub> Zn <sub>10</sub> Al <sub>10</sub>	81	67			
mp-Cu <sub>90</sub> Al <sub>10</sub>	46	48			
mp-Cu <sub>80</sub> Zn <sub>10</sub> Al <sub>10</sub>	81	99	80		
imp-ZnO	3.1	0.29	<200	H <sub>2</sub> S in N <sub>2</sub>	Baird et al. <sup>131</sup>
imp-5.7%Fe/ZnO	5.0	0.31			
imp-4.7%Co/ZnO	10	0.58			
imp-6.1%Cu/ZnO	4.8	0.42			
cp-ZnO	37	3.7			
cp-4.4%Fe/ZnO	17	1.7			
cp-6.2%Co/ZnO	46	4.7			
cp-4.7%Cu/ZnO	57	5.4			
Zn <sub>6</sub> Al <sub>2</sub> O <sub>9</sub>	69	8.9	30	2% H <sub>2</sub> S in N <sub>2</sub>	Baird et al. <sup>151</sup>
Co <sub>3</sub> Zn <sub>3</sub> Al <sub>2</sub> O <sub>10</sub>	110	12			
Co <sub>6</sub> Al <sub>2</sub> O <sub>11</sub>	93	15			
ZnO (0/100)	39	14	30	2% H <sub>2</sub> S in N <sub>2</sub>	Baird et al. <sup>132</sup>
18.66%Co-59.26%Zn (20/80)	65	24			
29.13%Co-40.36%Zn (40/60)	66	33			
31.69%Co-40.67%Zn (50/50)	60	20			
43.80%Co-16.42%Zn (70/30)	57	46			
64.74%Co-7.16%Zn (90/10)	83	63			
Co <sub>3</sub> O <sub>4</sub> (100/0)	87	92			

reaction were proposed, with the outward growth of ZnS and diffusion of zinc and oxygen through ZnS.<sup>147</sup> The authors derived a rate expression that also considered the evolution of the voids by a nucleation–growth mechanism, and the model predictions agreed quantitatively with experiments.

To enhance the H<sub>2</sub>S capacity at lower temperatures, another approach of varying the ZnO morphology involves doping with other metallic species (see Table 6).<sup>117,131,132,148–153</sup> Skrzypski et al. studied mixed Cu–Zn oxides and found a 6-fold increase in capacity at 200 °C by doping 6 mol% Cu.<sup>148</sup> XPS of pristine Cu<sub>0.03</sub>Zn<sub>0.97</sub>O showed a Cu 2p<sub>3/2</sub> peak (933.5 eV), characteristic of Cu<sup>2+</sup> surrounded by oxygen; after only partial sulfidation, this peak shifted to lower energy (932.6 eV),

indicating the appearance of Cu<sup>+</sup> in a sulfide environment. The sulfidation mechanism of these mixed oxides was further investigated using TEM and *in situ* synchrotron XRD.<sup>150</sup> While non-doped ZnO at 250 °C resulted in void formation at the ZnO/ZnS interface, Cu-doped ZnO showed no cavity formation; this suggests an inward growth mechanism where S<sup>2-</sup> anions diffuse from the external surface to the internal ZnO/ZnS interface and exchange with O<sup>2-</sup> anions. This radical change in mechanism was attributed to the presence of sulfur vacancies in the ZnS layer due to partial replacement of Zn<sup>2+</sup> by Cu<sup>+</sup>; these anionic vacancies accelerate the diffusion of sulfur to yield higher conversions of Cu–Zn oxides. XRD measurements showed that the size of the ZnS crystallites formed from non-

doped ZnO remains constant during the reaction. In contrast, the pronounced growth of Cu-doped samples enhances the mobility of sulfur anions in Cu-containing ZnS particles.

Jiang et al. also studied Cu–Zn and Cu–Zn–Al mixed metal oxides prepared via co-precipitation (cp) or multi-precipitation (mp) methods.<sup>149</sup> Better dispersion by aluminum results in smaller mean crystalline sizes and higher specific surface area of Al-containing sorbents; breakthrough sulfur capacities also improve as a result of reducing the thickness of the potential sulfide shell on the outer layer of the oxide, in turn reducing the diffusion path length. The Cu-rich adsorbents were more suitable for H<sub>2</sub>S adsorption than the Zn-rich adsorbents, with mp-Cu<sub>80</sub>Zn<sub>10</sub>Al<sub>10</sub> reaching nearly complete conversion at 80 °C. XRD of sulfidated samples revealed that the CuS peaks were much more dominant compared to the CuO peaks, but high-intensity ZnO peaks persisted for sulfidated Zn-rich samples. This suggests that CuS penetrated deep into the crystal, while ZnS likely formed only surface layers. Since the anionic sites in ZnO need to rearrange from hexagonal to cubic lattice on sulfidation, while those in CuO need only to transform from monoclinic to hexagonal, a faster sulfidation rate was proposed for CuO than that for ZnO. Similar structural arguments were invoked for Zn–Co oxides (discussed below) by Baird et al.<sup>132</sup> It should be noted here that the sulfidation reaction in the study by Jiang et al. was carried out at 40 °C,<sup>149</sup> as opposed to a much higher temperature (370 °C) in the study by Hayter et al. (discussed above)<sup>144</sup> that reported the wurtzite (hexagonal) phase of ZnS. This suggests that temperature can play a role in stabilizing different crystal structures of the product metal sulfide, which in turn can influence the overall sulfidation kinetics.

Co-precipitated mixed oxides showed smaller particle sizes, higher specific surface areas, and a higher H<sub>2</sub>S capacity compared to their impregnated counterparts that are synthesized by immersing the parent oxide in a salt solution of the dopant metal and calcining this precursor at ~350 °C.<sup>131</sup> These authors also studied adsorption on single-phase Co–Zn–Al–O prepared from co-precipitated hydroxycarbonate precursors (hydrotalcite-type structure).<sup>151</sup> The presence of aluminum increased the specific surface areas, but the modified compounds did not adsorb significantly more H<sub>2</sub>S per metallic (Zn, Co) species. H<sub>2</sub>S adsorption in Co–Zn oxides with varying Co/Zn atomic ratios showed that the increase in % utilization correlates well with the increase in surface area; the main function of Co doping seems to be increasing the surface area by reducing the particle size.<sup>132</sup> Thermodynamically, Co<sub>3</sub>O<sub>4</sub> has a more negative free energy for sulfidation than ZnO. Additionally, sulfiding cubic Co<sub>3</sub>O<sub>4</sub> normal spinel to spinel Co<sub>3</sub>S<sub>4</sub> or Co<sub>8</sub>S<sub>9</sub> will require lesser lattice rearrangement than that for hexagonal ZnO to cubic ZnS.

Westmoreland et al. showed that the intrinsic reaction rate of H<sub>2</sub>S with MnO over a temperature range of 300–800 °C is approximately 1 order of magnitude greater than that with ZnO, even though its surface area was an order of magnitude smaller.<sup>154</sup> Higher conversions were observed for mixed oxides of Zn containing Fe, Ni, Co, Mn, Cu, Al, Ti, and Zr at room temperature, especially for Zn<sub>2.9</sub>MnO<sub>4.2</sub>, but the reason for poor conversion for pure Mn<sub>3</sub>O<sub>4</sub> solid is not yet clear.<sup>117</sup> Regeneration of Zn–Ti-based mixed metal oxides using 20% O<sub>2</sub> in He at 750 °C for 4 h showed broad XRD peaks of very low intensity, indicating transformation to an amorphous material.<sup>152</sup> Doping this oxide with Mn, Cu, or Mo led to an improvement in H<sub>2</sub>S uptake for the regenerated solid: 41 mg/g

for 10Mn–45Zn–45Ti–O using a feed of 600 ppm H<sub>2</sub>S, 25% H<sub>2</sub>, and 7.5% CO<sub>2</sub> in helium. The presence of 1% H<sub>2</sub>O in the feed leads to a significantly higher capacity (160 mg/g). Davidson et al. have demonstrated the autocatalytic role of water during desulfurization on ZnO, suggesting a mechanism involving proton transfer from H<sub>2</sub>S to chemisorbed OH groups from hydration of the surface.<sup>137,155</sup> Addition of Fe showed a pronounced effect of Fe/Mn molar ratio on the morphology of the Fe–Mn–Zn–Ti mixed oxide crystallites.<sup>116</sup> H<sub>2</sub>S uptakes of 82 mg/g and 17 mg/g were observed for 5Fe–15Mn–40Zn–40Ti–O and 20Fe–40Zn–40Ti–O, respectively; in this case, 1% H<sub>2</sub>O led to only a small increase in capacity to 100 mg/g. Mössbauer spectroscopy is sensitive to changes in the energy levels of an atomic nucleus in response to its environment; quadrupole splitting ( $\Delta$ ) is induced by an electric field gradient of nearby electrons. Changes in  $\Delta$  during sulfidation and regeneration in the case of 5Fe–15Mn–40Zn–40Ti–O solid, compared to no changes for 20Fe–40Zn–40Ti–O solid, suggest that Mn makes the mixed oxide structures more susceptible to structural distortions, in turn enhancing H<sub>2</sub>S adsorption. Regeneration in 20% O<sub>2</sub> in He at 500 °C for 4 h resulted in over 80% of capacity recovered for the Fe-containing solids, while regeneration at 750 °C halved the H<sub>2</sub>S capacity. The structure was preserved for the regenerated 5Fe–15Mn–40Zn–40Ti–O solid with clear peaks in the XRD pattern.

Liu et al. investigated copper-based cp-mixed oxides (see Table 7) and observed high capacities for Fe-doped oxides.<sup>157</sup>

**Table 7. BET Surface Areas and Breakthrough Capacity in Mixed Copper-Based Metal Oxides for H<sub>2</sub>S Adsorption**

adsorbent	S <sub>BET</sub> (m <sup>2</sup> /g)	mg S/ g sorbent	T (°C)	composition	reference
cp-CuO	16.4	17.7	40	0.1% H <sub>2</sub> S in CO <sub>2</sub>	Liu et al. <sup>156</sup>
cp-Cu <sub>3</sub> Al	72.3	86.0			
cp-Co <sub>0.44</sub> Cu <sub>3</sub> Al	87.4	73.4			
cp-Ni <sub>0.44</sub> Cu <sub>3</sub> Al	86.0	55.7			
cp-Ce <sub>0.44</sub> Cu <sub>3</sub> Al	82.1	91.1			
cp-Fe <sub>0.44</sub> Cu <sub>3</sub> Al	96.7	114			
		207	70		
		212	100		
		220	130		
cp-CuO	16.4	25.3	40	0.1% H <sub>2</sub> S in N <sub>2</sub>	
cp-Cu <sub>3</sub> Al	72.3	106			
cp-Fe <sub>0.44</sub> Cu <sub>3</sub> Al	96.7	125			

Capacities were 10–40% higher for H<sub>2</sub>S in bulk N<sub>2</sub> compared to the case of bulk CO<sub>2</sub>, suggesting some degree of competitive adsorption with CO<sub>2</sub>; the inhibition effect was lower for doped CuO compared to pure CuO. The authors report that regenerated CuO exhibited a breakthrough capacity up to 75% of its initial value when regenerated between 100 and 200 °C but decreased rapidly with further increase of regeneration temperature. The authors explain that CuS tends to decompose into the more stable Cu<sub>2</sub>S when the temperature is above 220 °C. The authors carried out five adsorption–regeneration cycles for pure CuO, Cu–Al–O, and Fe–Cu–Al–O with regeneration using air at 100 °C. For CuO, the regenerated capacities were maintained at 75% of the fresh adsorbent capacity; however, regenerated capacities decreased for the Cu–Al–O and Fe–Cu–Al–O adsorbents and became steady during the last two cycles at 50% and 43% of the fresh capacity,

**Table 8.** BET Surface Areas and Percentage Metal Utilization in Mesoporous Metal Oxides for H<sub>2</sub>S Adsorption

adsorbent	<i>S</i> <sub>BET</sub> (m <sup>2</sup> /g)	% utilization	<i>T</i> (°C)	composition	reference
3DOM-F65	44	68	350	300 ppm H <sub>2</sub> S, 5% H <sub>2</sub> in N <sub>2</sub>	Fang et al. <sup>158</sup>
3DOM-F90	43	70			
3DOM-F158	34	93			
3DOM-F205	31	90			
3DOM-F550	16	79			
3DOM-FS156	110	97			
FS-1	125	30	80	360 ppm H <sub>2</sub> S in N <sub>2</sub>	Huang et al. <sup>159</sup>
FS-2	120	42			
FS-4	120	75			
FS-8	113	76			
FS-16	72	21			
γ-Fe <sub>2</sub> O <sub>3</sub>	82	18			
α-Fe <sub>2</sub> O <sub>3</sub>	36	0			
Fe <sub>2</sub> O <sub>3</sub> (commercial)	87	—			
γ-Fe <sub>2</sub> O <sub>3</sub>	82	5.6	60		
		2.6	40		
		1.0	20		
ZnO (commercial)	60	16	30	360 ppm H <sub>2</sub> S, 3% H <sub>2</sub> O in N <sub>2</sub>	Wang et al. <sup>160</sup>
SZ50	220	11			
3DOM-SZ50	340	69			
3DOM-SZ20	360	60			
3DOM-SZ73	140	59			
Co <sub>3</sub> O <sub>4</sub> (commercial)	3	4	200	1% H <sub>2</sub> S in He	Pahalagedara et al. <sup>161</sup>
m-Co-150	23	9			
m-Co-250	140	130			
m-Co-350	99	130			
m-Co-450	38	40			
m-Co-250	140	30	25		
		50	100		
		100	150		
		120	175		
		130	250		
m-Cr-250	N/A	50	200		
m-Cu-250	N/A	60			
m-Mn-250	N/A	110			
m-Fe-250	N/A	60			

respectively. These studies bring to light the difficulty in regenerating the high capacities of mixed metal oxides; future work in this area should focus not only on high-capacity sorbents but also on better regenerability.

Researchers have investigated H<sub>2</sub>S adsorption in three-dimensionally ordered macroporous (3DOM) structures of iron oxide (3DOM-F) and of silica-supported iron oxide (3DOM-FS) prepared by a colloidal crystal templating method (see Table 8).<sup>158,159</sup> Highly uniform polystyrene (PS) beads ordered into close-packed domains were used as a template for the growth of the inorganic 3DOM structure; the resulting pore diameters were considerably smaller than the original PS sphere.<sup>158</sup> The shrinkage in size resulting from sintering during calcination ranged from 45 to 59% for the 3DOM-F sorbents and from 37 to 45% for the 3DOM-FS sorbents. 3DOM-FS showed somewhat smaller nanoparticles (5 nm) than 3DOM-F (25 nm), which the authors explain as silicon keeping the iron grains separate and preventing the latter from growing larger during calcination. Depending on the macropore diameter, these structures have variable surface areas, ranging from 16 to

44 m<sup>2</sup>/g for 3DOM-F and from 80 to 220 m<sup>2</sup>/g for 3DOM-FS. Mesopore-sized void spaces between the crystallites are observed in the TEM images and also from the pore size distribution (20–33 and 6–17 nm for 3DOM-F and 3DOM-FS, respectively) obtained from the N<sub>2</sub> isotherms. It can be seen that the % utilization of Fe improves with increase in macropore diameter up to about 150 nm due to possible reduction in diffusion limitations, but further increasing the macropore diameter leads to a lowering of Fe utilization. Nearly complete regeneration of 3DOM-FS samples using 2% O<sub>2</sub> in N<sub>2</sub> at 300 °C was shown for three cycles. Scanning electron microscopy (SEM) illustrated that, despite some cracking, the macroporosity and ordering of the structure was still intact and the overall 3DOM structure was retained after second regeneration.

Huang et al. studied the effect of Fe:Si ratio from 1 to 16 (and also the case of no Si), temperature, and humidity on the low-temperature desulfurization performance of 3DOM structures.<sup>159</sup> Breakthrough capacities showed an increase with increase in Fe:Si ratio up to 8; low capacity at even

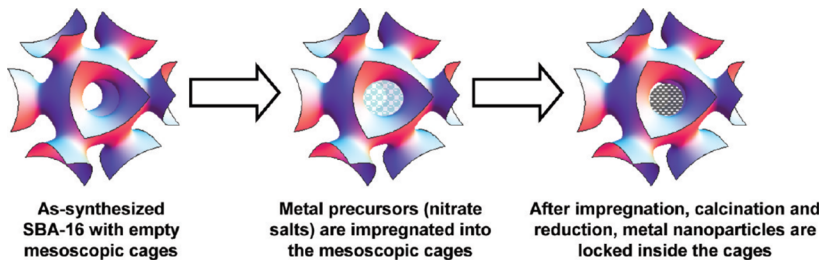


**Figure 5.** Schematic illustration of the impregnation and thermal treatment process for stabilizing metal nanoparticles in the cage structure of SBA-16. Reprinted with permission from ref 171. Copyright 2009 American Chemical Society.

higher Fe:Si ratios was attributed to the presence of  $\alpha$ -Fe<sub>2</sub>O<sub>3</sub>. SiO<sub>2</sub> enhanced the dispersion of Fe<sub>2</sub>O<sub>3</sub>, which stabilized the  $\gamma$ -Fe<sub>2</sub>O<sub>3</sub> and hindered its transformation to  $\alpha$ -Fe<sub>2</sub>O<sub>3</sub> during calcination. The authors further explain that the vacancy site in the lattice of  $\gamma$ -Fe<sub>2</sub>O<sub>3</sub>, accompanied by its lower density, larger surface area, and smaller grain size, facilitates ion diffusion. Relative humidity of  $\sim$ 10% favored H<sub>2</sub>S removal. It was also found that conventional regeneration at 300 °C using 5% O<sub>2</sub> in N<sub>2</sub> resulted in a drastic loss of capacity for the regenerated material. As an alternative regeneration technique, the authors proposed an *in situ* regeneration process by adding 5% O<sub>2</sub> to the feed stream (desulfurization and regeneration occur at the same time); this resulted in breakthrough capacities twice those observed when O<sub>2</sub> was absent from the inlet gas. In the case of conventional regeneration, a significant fraction of  $\gamma$ -Fe<sub>2</sub>O<sub>3</sub> transformed to  $\alpha$ -Fe<sub>2</sub>O<sub>3</sub>, while no such change was observed for the case where O<sub>2</sub> was added to the feed. It is unclear if this simultaneous desulfurization–regeneration process is resulting in a transformation of H<sub>2</sub>S to SO<sub>2</sub>; monitoring only H<sub>2</sub>S concentration in the outlet stream may hint at high H<sub>2</sub>S breakthrough capacity, but monitoring SO<sub>2</sub> concentration may reveal that little or no sulfur is adsorbed in such a process.

In another study, Wang et al. synthesized 3DOM structures of ZnO and silica, with different weight percent of ZnO ranging from 23 to 70%.<sup>160</sup> Samples exhibited a typical amorphous structure, except 3DOM-SZ73, which showed peaks corresponding to ZnO in the XRD pattern. Highest utilization of 69% was observed for the 3DOM structure with 50 wt% ZnO; nearly 70% of this capacity was retained for four regeneration cycles (air at 500 °C for 4 h). These adsorbents hold significant promise for desulfurization at ambient temperature, and investigation of structural stability over several regeneration cycles will help reveal the true potential of these sorbents for commercial application.

Even though cobalt oxide is one of the thermodynamically more favorable metals for desulfurization of H<sub>2</sub>S, attempts at making it a major component for removing H<sub>2</sub>S are limited.<sup>132,162</sup> Due to larger particle sizes, bulk cobalt oxide showed slower sulfidation and incomplete conversion even at 500 °C, but when it was supported on either Al<sub>2</sub>O<sub>3</sub> or TiO<sub>2</sub>, higher rates and complete conversion could be observed even at 300 °C, primarily due to smaller grain size.<sup>162</sup> TiO<sub>2</sub>-supported Co<sub>3</sub>O<sub>4</sub> showed lower activation barriers, and it may serve as an effective H<sub>2</sub>S removal sorbent, even at lower temperatures. Pahalagedara et al. investigated mesoporous cobalt oxides (m-Co-X, where X = 150, 250, 350, or 450 °C, the calcination temperature) as desulfurization sorbents and could achieve 100% capacity at 150 °C.<sup>161</sup> The reason for breakthrough capacities higher than 100% metal utilization for mesoporous Co and Mn is not clear but may be attributed to

physically adsorbed H<sub>2</sub>S beyond the chemically reacted capacity. The authors also investigated other mesoporous materials (Cr<sub>2</sub>O<sub>3</sub>, CuO, Mn<sub>2</sub>O<sub>3</sub>, and Fe<sub>2</sub>O<sub>3</sub>) that showed superior activities compared to their nonporous analogues (as high as 200 times). Using field-emission scanning electron microscopy (FESEM), the mesostructure was shown to be preserved after sulfidation, but the mesostructure collapsed during calcination at 450 °C, and regeneration at 400 °C in air resulted in a 45% drop in capacity. An alternative regeneration technique for ZnO catalysts using a 3:1 H<sub>2</sub>O/N<sub>2</sub> mixture at 800 °C resulted in nearly 100% capacity regeneration without loss of porosity, as opposed to only about 10% regeneration and significant increase in bulk density of the adsorbent when air was used at the same temperature.<sup>163</sup> A significant scope still remains for developing better regeneration procedures for metal oxides that retain not only the adsorption capacity reversibility but also the structural reversibility. The latter is more important from the perspective of adsorbent bed stability to prevent attrition of the solids that will increase the pressure drop across the bed.

### 3.2. Metals

Early literature focused on H<sub>2</sub>S poisoning of metal catalysts and the threshold concentration below which H<sub>2</sub>S will not unduly poison a given metal catalyst. McCarty and Wise investigated the thermodynamics of H<sub>2</sub>S chemisorption on different metallic catalysts over a wide range of temperatures and reported the order of increasing activity toward H<sub>2</sub>S at 300 °C and 50% surface coverage to be Ni > Co > Ru > Fe > Pt.<sup>164–167</sup> Using magnetization measurements, Den Besten and Selwood showed that H<sub>2</sub>S is dissociatively chemisorbed on the Ni surface.<sup>168</sup> The enthalpy of adsorption of H<sub>2</sub>S on Ni was measured to be about 130–160 kJ/mol.<sup>164,169</sup> Due to such high enthalpies of adsorption, adsorbent regeneration will result in a very expensive natural gas desulfurization process. Metal adsorbents may be useful as a final polishing step to limit the energy duty for H<sub>2</sub>S adsorption/regeneration. For example, they can be useful in certain applications such as direct-methane fuel cells<sup>170</sup> to achieve ultra-low sulfur content methane from pre-treated natural gas.

Usually, when metals are employed for H<sub>2</sub>S removal, they are used as sacrificial sorbents since, during a regeneration process, metals will have a strong tendency to sinter and aggregate, resulting in a complete loss of surface area and active sites. By isolating and stabilizing small metal particles in cubic structured mesoporous silica, Li et al. were probably the first to demonstrate the regeneration of the sulfur-loaded adsorbents with minimal sintering (see Figure 5).<sup>171</sup> Adsorption was carried out at 300 °C using a coal syngas composition of 23% H<sub>2</sub>, 29% CO, 8% CO<sub>2</sub>, 30% H<sub>2</sub>O, 10% He, and 10 ppm H<sub>2</sub>S, and regeneration was carried out at 550 °C using a five-cycle

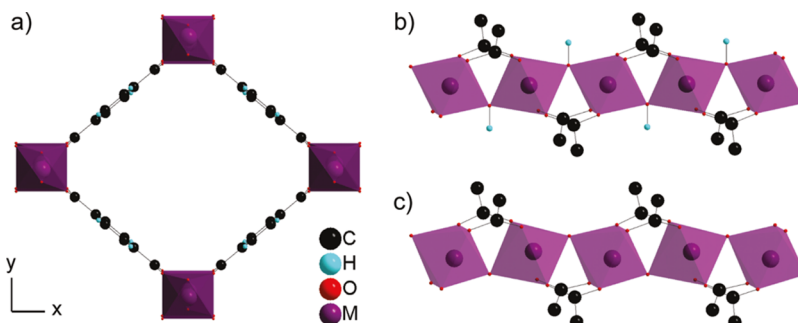


**Figure 6.** (a) View of the MIL-53(Cr)LP/MIL-47(V) structures along the chain ( $z$  axis), highlighting the 1D pores system with  $M = \text{Cr}^{3+}$  or  $\text{V}^{4+}$ . View perpendicular to the pores of the MIL-53(Cr) (b) and MIL-47(V) (c) with  $\mu^2\text{-OH}$  and  $\mu^2\text{-O}$  atoms linked to the metal atom (M), respectively. Reprinted with permission from ref 179. Copyright 2011 American Chemical Society.

alternating oxidation–reduction treatment of pure  $\text{H}_2$  and 10% air in Ar with a short Ar purge in between. A fully regenerable capacity of 7 mg of S/g adsorbent over five adsorption–regeneration cycles was achieved for 16.6 wt% Ni loaded on SBA-16, with the ratio of chemisorbed  $\text{H}_2\text{S}$  to Ni being 0.07. It is unclear, however, whether  $\text{H}_2\text{S}$  adsorption was carried out on the hydrogen-regenerated form of the adsorbent or on the air-regenerated form that would result in a metal oxide.

### 3.3. Metal–Organic Frameworks

MOFs are porous structures resulting from coordination of metal ions or clusters to organic ligands.<sup>172</sup> Bare metals exist at most as nanoparticles formed out of clusters of several thousands of atoms and suffer from activity loss by way of sintering during high-temperature regeneration. MOFs provide a scheme for isolating the metal atoms or the metal oxide clusters by being chemically coordinated within a porous framework. This allows design of adsorbents where not only each metal atom exclusively interacts with a single adsorbate molecule but also each of these interaction sites may be regenerated without significant loss of activity. Additionally, appropriately functionalized organic ligands can also contribute in promoting the selectivity toward the desired gas molecule. MOFs offer a large parameter space to rationally design the size, shape, and functionality of pores with high adsorption and/or diffusion selectivity toward the molecule of interest. In addition to selectivity, performance and structural reversibility on regeneration are important factors in judging the performance. The presence of polar impurities such as  $\text{H}_2\text{O}$  on the adsorption performance as well as stability of the adsorbent structure can also play determining roles in the successful application of MOFs for desulfurization applications. Typical pore diameters in MOFs are in the microporous regime ranging from 3 to 20 Å<sup>173</sup> although more recently, MOFs with pore sizes as high as 85 Å have been synthesized for inclusion of large biological molecules.<sup>174</sup> Due to the highly porous nature of most MOFs, their lower conductivity (0.3 W/m·K for MOF-5 at 300 K<sup>175</sup>) compared to that of crystalline materials in general can be a potential concern for strong host–guest interactions. Desulfurization using MOFs has been reviewed in the past;<sup>14,15,176,177</sup> here we try to summarize some of these topics, provide our interpretation, and identify areas for further investigation.

Hamon et al. carried out the first experimental study of  $\text{H}_2\text{S}$  adsorption in MOFs; these included the small-pore (SP) MIL-53( $\text{Al}^{III}$ ,  $\text{Cr}^{III}$ ,  $\text{Fe}^{III}$ ) and MIL-47( $\text{V}^{IV}$ ) (~11 Å) and the large-pore (LP) MIL-100(Cr) and MIL-101(Cr) (25 and 30 Å cage diameter and 4.8×5.8 and 12.5×12.5 Å pore apertures,

respectively).<sup>178</sup> SP MILs are built from corner-sharing chains of metal oxide ( $\text{M}^{IV}\text{O}_6$ ) or hydroxide ( $\text{M}^{III}\text{O}_4(\text{OH})_2$ ) octahedra connected through terephthalate moieties ( $S_{\text{BET}} \approx 1000 \text{ m}^2/\text{g}$ ) (see Figure 6). LP MILs comprise of trimers of chromium octahedra linked with trimesate (MIL-100) or terephthalate (MIL-101) ( $S_{\text{BET}} > 2000 \text{ m}^2/\text{g}$ ). MIL-100, MIL-101, and MIL-47 showed the type-I-shaped (no adsorption step) isotherm, indicating that these are rigid structures; MIL-53( $\text{Al},\text{Cr},\text{Fe}$ ) exhibited two-step adsorption isotherms, which the authors proposed to be caused by the polar  $\text{H}_2\text{S}$  molecules interacting strongly with the OH groups of the inorganic chains at the pore opening, leading to closure of the pores at low loading. This hypothesis was later claimed to be verified using infrared (IR) spectroscopy and molecular simulations.<sup>179</sup> It should be noted here that, for the breathing MOF (MIL-53(Cr)), isotherms were simulated for two different rigid MOF structures, representing the narrow and the large-pore regimes in the experimental adsorption isotherm. By imposing the experimental fractions of each pore type as a function of pressure, a composite isotherm was calculated for the simulated isotherms. While this strategy yields a good match with the experimental data, the study did not investigate the ability to predict the structural transformation. Measurement of excess  $\text{CH}_4$  adsorption before and after high-pressure  $\text{H}_2\text{S}$  adsorption followed by vacuum desorption showed full recovery of  $\text{CH}_4$  capacity for MIL-47(V) and MIL-53( $\text{Al},\text{Cr}$ ), partial recovery for MIL-100 and MIL-101, and complete loss of capacity for MIL-53(Fe) due to its decomposition into iron sulfide. At 30 °C and 20 bar, MIL-101 showed an unprecedented  $\text{H}_2\text{S}$  loading of 38.4 mmol/g; MIL-53( $\text{Al},\text{Cr}$ ), MIL-47, and MIL-100 showed saturation loadings of 11.8, 13.1, 14.6, and 16.7 mmol/g, respectively, which are also quite high compared to those of other  $\text{H}_2\text{S}$  adsorbents. However, in cases such as off-shore natural gas sweetening, where having a smaller footprint is important, volumetrically bulky porous MOFs suffer a drawback. Adsorption being an exothermic process, sharp increases in temperatures for MOFs with ultra-high capacity raise concerns about bed stability in the absence of adequate heat transfer. Attempts to compute thermal conductivities of MOFs in the presence of adsorbed gases are starting to elucidate that the thermal conductivity of MOFs decreases with increasing pore sizes.<sup>180,181</sup>

Vaesn et al. explored functionalization of MOFs for desulfurization application by comparing amino-functionalized titanium terephthalate MIL-125(Ti)-NH<sub>2</sub> versus its parent MIL-125(Ti) analogue.<sup>182</sup> The frameworks consists of tetrahedral (4.7 Å) and octahedral (10.7 Å) cages, accessible

through triangular windows of 5–7 Å. The cage diameters for the functionalized material are slightly smaller those of the parent material (6 and 12 Å for the tetrahedral and octahedral cages, respectively). Grand Canonical Monte Carlo (GCMC) simulations were carried out using force fields that were shown to yield a decent agreement with the single-component experimental adsorption isotherms and enthalpies. The GCMC-predicted binary  $\text{H}_2\text{S}/\text{CH}_4$  selectivity values (at 10 bar, 30 °C, and  $y_{\text{H}_2\text{S}} = 0.001$ ) for MIL-125(Ti) and MIL-125(Ti)-NH<sub>2</sub> were reported to be 40 and 67, respectively. The  $\text{H}_2\text{S}$  adsorption enthalpy for these materials (~30 kJ/mol) is comparable to that for the aluminosilicate zeolite 4A (~35 kJ/mol).<sup>183</sup> These MOF materials are thermally stable up to 300 °C, but only up to 100 °C in water vapor. Their performance and structural stability in the presence of both  $\text{H}_2\text{S}$  and  $\text{H}_2\text{O}$  require further investigation. Furthermore, the moderately high  $\text{CO}_2/\text{CH}_4$  selectivity (~7) allows for envisaging a one-step process for the concomitant elimination of  $\text{CO}_2$  and  $\text{H}_2\text{S}$ . Obtaining separate  $\text{CO}_2$ -rich and  $\text{H}_2\text{S}$ -rich streams unnecessarily increases the separation costs if the end goal for  $\text{H}_2\text{S}$  is high-pressure reinjection into empty wells, instead of the conventional Claus process for sulfur recovery.

Yang et al. studied  $\text{H}_2\text{S}$  adsorption in MIL-68(Al) at room temperature using molecular simulations and experiments.<sup>184</sup> This framework consists of two kinds of channels, triangular (6.0–6.4 Å) and hexagonal (16–17 Å), running along the *c* axis (see Figure 7). It was found that only some of the hydroxyls

additional saturation capacity, that is predicted from simulations, may or may not be accessible; the difference in the adsorbed amounts of  $\text{CH}_4$  and  $\text{CO}_2$  for the material activated at 260 or 330 °C was negligible. Although MIL-68(Al) is a polymorph of MIL-53(Al) (described above), unlike the latter, the former does not seem to exhibit framework flexibility, as evidenced by its type-I adsorption isotherm. This brings to light the importance of MOF framework topology in addition to the choice of the metallic cluster and the organic ligands, further iterating the importance of powerful screening of adsorbents using existing and new computational techniques that capture these subtle differences.

Cu-BTC (or HKUST-1 or MOF-199) comprises of an intersecting three-dimensional system of large square-shaped pores (9 × 9 Å) and small tetrahedral pockets (5 Å) formed with copper as the inorganic metal and benzene-1,3,5-tricarboxylic acid (BTC), also known as trimesic acid, as the organic linker (see Figure 8) with a reasonable degree of thermal stability (up to 240 °C).<sup>185</sup> In the past few years, several research groups have investigated various aspects of  $\text{H}_2\text{S}$  adsorption in this material.<sup>186–192</sup> Petit et al. first studied HKUST-1 and its composites with graphite oxide under ambient conditions using 1000 ppm  $\text{H}_2\text{S}$  in moist air.<sup>186</sup> The authors commented that bed pre-humidification does not prevent the adsorption of  $\text{H}_2\text{S}$  (2.7 mmol/g); on the contrary, it favors its retention via dissolution in the water film. Additional  $\text{H}_2\text{S}$  measurements in absence of moisture will help better understand the role of  $\text{H}_2\text{O}$ . The XRD pattern revealed that exposure to  $\text{H}_2\text{S}$  results in a collapse of the MOF structure. From the decrease in pH on  $\text{H}_2\text{S}$  adsorption and from Fourier-transform infrared (FTIR) spectroscopy, it was concluded that the BTC ligands were released (no more coordinated to copper) to their acidic form.

Watanabe and Sholl investigated chemisorption of several molecules, including  $\text{H}_2\text{S}$  and  $\text{H}_2\text{O}$ , in Cu-BTC using plane wave periodic DFT.<sup>187</sup>  $\text{H}_2\text{O}$  and  $\text{H}_2\text{S}$  showed similar binding energies of 51 and 47 kJ/mol, respectively. Single-component GCMC adsorption simulations at room temperature, computed by restricting the chemisorbed molecules in the geometries obtained from prior DFT calculations, showed that the onset pressure for  $\text{H}_2\text{O}$  adsorption is nearly 3 orders of magnitude lower than that for  $\text{H}_2\text{S}$ . The influence of physisorbed molecules on the adsorption isotherm was not considered in this study.  $\text{H}_2\text{S}$  models in the literature, trained to reproduce the bulk liquid densities and vapor pressures, significantly overestimate the gas-phase dipole moment of  $\text{H}_2\text{S}$ . Gutiérrez-Sevillano et al. developed new  $\text{H}_2\text{S}$  models to test whether a model with an accurate gas-phase dipole moment could predict a strong interaction of  $\text{H}_2\text{S}$  with Cu-BTC, in line with the experimental observation.<sup>188</sup> The simulations used generic force fields for the MOF structure that have been shown to perform reasonably well for some of the other adsorption studies in MOFs.<sup>184</sup> Additionally, their hybrid DFT calculations showed that indeed  $\text{H}_2\text{O}$  has a higher affinity for the copper sites (extra 3.3 kJ/mol) compared to  $\text{H}_2\text{S}$ . *Ab initio* molecular dynamics (MD) studies of the molecules adsorbed on the model cluster showed  $\text{H}_2\text{O}$  to be closer to the copper center compared to  $\text{H}_2\text{S}$  by about 2.6 Å. Another hybrid DFT study, with a damped  $1/r^6$  term to account for London dispersion, showed that the interaction energies for  $\text{H}_2\text{O}$  and  $\text{H}_2\text{S}$  adsorption on Cu-BTC are –60.9 and –52.2 kJ/mol, respectively, reiterating the dominance of  $\text{H}_2\text{O}$ .<sup>189</sup> Different theoretical treatments are in agreement that the interaction of

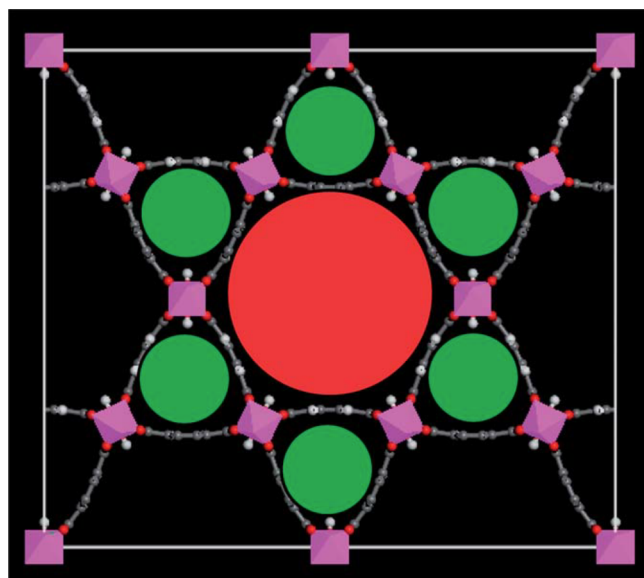


**Figure 7.** View of the crystalline structure of the MIL-68(*M*) (*M* = V, Ga, Fe, or Al) along the *c* axis: green and red circles denote the triangular and hexagonal channels, respectively (metal polyhedra, pink; C, gray; O, red; H, white). Reproduced with permission from ref 184. Copyright 2012 The Royal Society of Chemistry.

were available for interaction, as evidenced by the computed isotherm, obtained by blocking the triangular channels, matching exactly with the experimental isotherm. It can also be observed that the saturation loadings are less sensitive to the choice of force field parameters than the Henry's law region slope. This partially activated material was fully regenerable for five consecutive cycles with a pure-component  $\text{H}_2\text{S}$  capacity of 12 mmol/g at 30 °C and 12 bar and an adsorption enthalpy of ~21 kJ/mol. Even if the material can be fully activated, the 25%

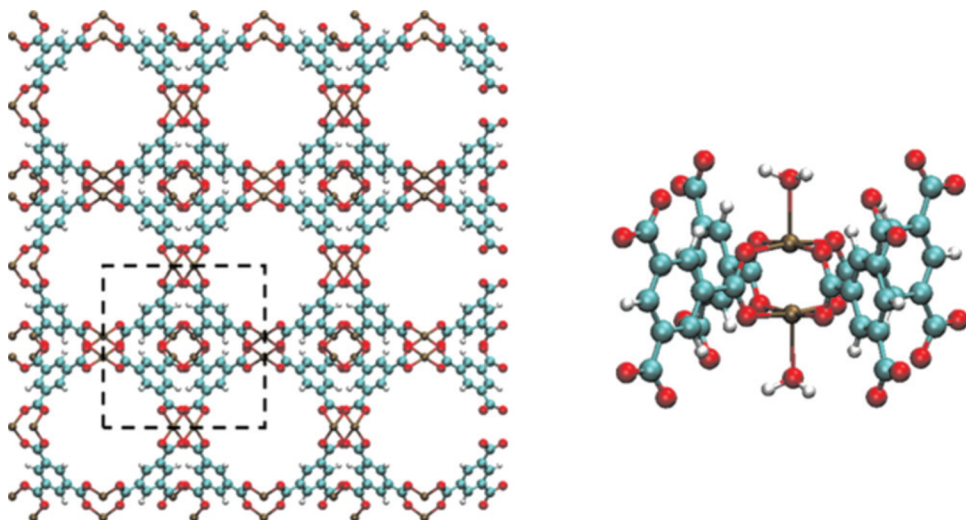


**Figure 8.** Crystal structure of dehydrated  $\text{Cu}_3(\text{BTC})_2$  view along the [100] direction (left). Carbon, hydrogen, copper, and oxygen atoms are represented by the blue, white, brown, and red spheres, respectively. The paddlewheel structure of a Cu dimer in  $\text{Cu}_3(\text{BTC})_2$  with water molecules coordinated to the metal centers is shown on the right. Reprinted with permission from ref 187. Copyright 2010 AIP Publishing.

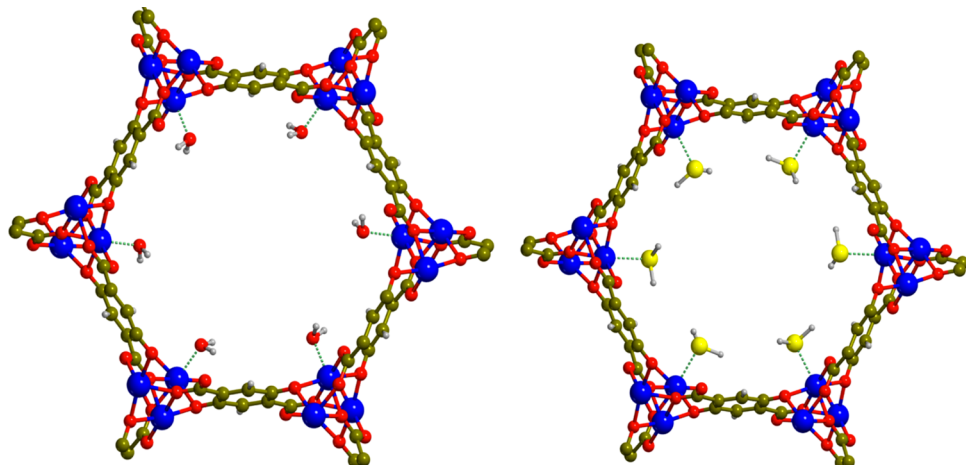


**Figure 9.**  $\text{H}_2\text{O}$  (left) and  $\text{H}_2\text{S}$  (right) molecules as arranged in the CPO-27-Ni channels. Metal, sulfur, oxygen, carbon, and hydrogen atoms are blue, yellow, red, gray, and white, respectively. Reprinted with permission from ref 195. Copyright 2013 American Chemical Society.

Cu-BTC with  $\text{H}_2\text{S}$  is weaker than that with  $\text{H}_2\text{O}$ , thus failing to explain the experimental observation that  $\text{H}_2\text{S}$  converts Cu in Cu-BTC to black CuS in the presence of moisture.<sup>186</sup> An important point to note here is that the theoretical studies only considered the host–guest interaction; however,  $\text{H}_2\text{S}$  reacts chemically with copper to form CuS, and the thermodynamics of product formation have not been attempted in any of the theoretical studies reported so far.

Li et al. experimentally investigated the same system by activating the material before carrying out  $\text{H}_2\text{S}$  adsorption.<sup>190</sup> They found that the breakthrough capacity increased by 38% on activation at 180 °C compared to the unactivated sample and decreased by 10% if the sample was activated further at 200 °C. The breakthrough capacity also increased by 40% when the adsorption temperature was raised from 30 to 80 °C. Both of these observations suggest that there is a competitive adsorption between  $\text{H}_2\text{O}$  and  $\text{H}_2\text{S}$ , and lowering the adsorbed quantity of moisture, either with an increased activation temperature or with an increased adsorption temperature, increases the  $\text{H}_2\text{S}$  capacity. Contrary to this inference, Peterson et al. observed no change in  $\text{H}_2\text{S}$  adsorption capacity under dry

(0% relative humidity) and wet (80% relative humidity) conditions.<sup>191</sup> In spite of a lot of research effort to understand the role of moisture in desulfurization using Cu-BTC, this problem remains unresolved.

Eddaoudi et al. synthesized a series of 16 isoreticular (having the same network topology) MOFs (IRMOF-*n*, *n* = 1–16) based on a skeleton of Zn-based MOF-5, wherein the pore functionality and size were varied without changing the original cubic topology.<sup>173</sup> Theoretical investigation of  $\text{H}_2\text{S}$  was performed in IRMOF-1 (or MOF-5) having 1,4-benzenedicarboxylate organic linkers; the heat of adsorption was  $\sim -15$  kJ/mol, much lower than that for Cu-BTC ( $\sim -30$  kJ/mol) due to wider (11.2 Å) pores of IRMOF-1 compared to confined (5 Å) tetrahedral-shaped pockets in Cu-BTC. IRMOF-1 also results in  $\sim 6$  kJ/mol weaker binding than  $\text{H}_2\text{O}$ , suggesting the difficulty in using this material for  $\text{H}_2\text{S}$  adsorption from moist natural gas.<sup>188</sup> Wang et al. studied IRMOF-3 (free pore diameter of 9.6 Å) having 2-amino-1,4-benzenedicarboxylate ligands and showed that the breakthrough capacity increased by 46% on activation at 150 °C compared to that of the unactivated sample and decreased by 93% if the sample was

activated further at 200 °C.<sup>193</sup> The breakthrough capacity decreased to 19% when the adsorption temperature was increased from 30 to 60 °C. It would be interesting to study comparative H<sub>2</sub>S adsorption in the two MOFs (IRMOF-1 and IRMOF-3) to understand the role of the –NH<sub>2</sub> group in IRMOF-3 for selective binding with acid gases.

Allan et al. studied desulfurization using Ni-CPO-27 and Zn-CPO-27, where Ni/Zn cations are linked by 2,5-dihydroxyterephthalic acid organic linkers, forming a honeycomb lattice with channels of ~11 Å pore diameter.<sup>194</sup> In the hydrated state, each metal is coordinated by one H<sub>2</sub>O molecule, but upon activation at 150 °C under vacuum, H<sub>2</sub>O is removed, leaving the metal in square pyramidal geometry with an open metal site, resulting in  $S_{\text{BET}} = 1193$  and 379 m<sup>2</sup>/g, respectively. H<sub>2</sub>S exposure did not degrade the crystalline structure of Ni-CPO-27 but amorphized Zn-CPO-27.<sup>194,195</sup> Ni-CPO-27 showed a steep rise in loading up to 6.4 mmol/g (corresponding to each metal center interacting with one gas molecule, see Figure 9), indicating a sharp chemisorption regime followed by a slower uptake likely due to physisorption up to 12 mmol/g at atmospheric pressure. Adsorbents with such high loadings at low pressures are rare, and it may be useful in effectively removing large amounts of H<sub>2</sub>S from gas streams with a low H<sub>2</sub>S partial pressure. However, the material cannot be fully regenerated at outgassing temperature of 150 °C and a vacuum of 0.1 Pa,<sup>194</sup> but it could be nearly completely regenerated at 200 °C.<sup>195</sup> The authors hint at some damage to the framework by this high-temperature regeneration; additional microscopy and diffraction data for the regenerated samples should help understand the degree of damage and whether the structural damage increases with the number of regeneration cycles. The heat of adsorption is nearly constant (56–58 kJ/mol) up to a loading of 0.7 H<sub>2</sub>S molecule per atom of Ni, assuming all Ni atoms are activated. The authors comment that, beyond this loading, the drop in interaction strength can be justified with typical weak physisorption with no specific interaction between the host/guest species. However, it is unclear how the physisorption regime can start without reaching a loading of 1 H<sub>2</sub>S molecule per Ni atom, and this could possibly indicate incomplete activation of the MOF (~70% activated). Compared to other MOFs investigated so far for H<sub>2</sub>S adsorption, Ni-CPO-27 shows the highest uptake and high enthalpy of adsorption (indicative of possibly higher selectivity over methane) with structural stability. However, the experimental heat of adsorption of H<sub>2</sub>O for this material is <−100 kJ/mol, which may or may not make this material an ideal adsorbent for natural gas in the presence of moisture. Nonetheless, the material appears to be very promising and should be investigated for H<sub>2</sub>S adsorption in the presence of H<sub>2</sub>O.

Using GCMC simulations with generic force fields that have not been thoroughly validated for any particular property, Peng and Cao carried out a screening of some select porous carbons, zeolites, and MOFs for a feed containing 0.2% H<sub>2</sub>S, 29.8% CO<sub>2</sub>, and 70% CH<sub>4</sub> at 50 bar and 30 °C.<sup>196</sup> Among the MOFs, indium-based *rho*-zMOF (a zeolite-like MOF with the topology of *rho*-zeolite) and socMOF showed high selectivity (175 and 100, respectively) and capacity (2.6 and 1.8 mmol/g, respectively). The capacity for *rho*-zMOF at temperatures of 60 °C and higher is reported to be 0.5 mmol/g, suggesting a working capacity of about 2 mmol/g with very low temperatures of regeneration. While this is an important discovery, there is a considerable uncertainty in the force-field parameters

for such highly charged systems, and experiments will help to confirm the validity of the predictions as regards such high selectivity and capacity as well as stability of MOF in the presence of impurities such as moisture.

Very recently, Belmabkhout et al. investigated In<sup>3+</sup>-, Fe<sup>3+</sup>-, Ga<sup>3+</sup>-, and Al<sup>3+</sup>-based socMOFs as adsorbents and thin-film membranes for the production of high-quality hydrocarbons (CH<sub>4</sub>, C<sub>3</sub>H<sub>8</sub> and *n*-C<sub>4</sub>H<sub>10</sub>, and olefins) from H<sub>2</sub>S-containing gas streams. Only Ga<sup>3+</sup>- and Al<sup>3+</sup>-based socMOFs could preserve the crystal structure on exposure to H<sub>2</sub>S.<sup>197</sup> The authors measured pure-component adsorption isotherms for H<sub>2</sub>S, CO<sub>2</sub>, and CH<sub>4</sub> in Ga<sup>3+</sup>-socMOF at 25 °C and found that, unlike CH<sub>4</sub> and CO<sub>2</sub>, H<sub>2</sub>S showed a steep adsorption. The authors also carried out breakthrough measurements for a ternary mixture containing 5% H<sub>2</sub>S, 5% CO<sub>2</sub>, and 90% CH<sub>4</sub> for six adsorption–desorption cycles with a combination of temperature and vacuum swing regeneration. Optimal regeneration was achieved at 160 °C under a helium flow for 8 h with complete recyclability of the adsorbent. Since the mass of adsorbent used for the experiment is unclear (between 0.1 and 0.4 g), the reported H<sub>2</sub>S breakthrough time of 40 min translates to a breakthrough capacity between 2 and 8 mmol/g. CH<sub>4</sub> and CO<sub>2</sub> breakthrough occurred at nearly 0 and 5 min, respectively, suggesting very high H<sub>2</sub>S/CH<sub>4</sub> and H<sub>2</sub>S/CO<sub>2</sub> selectivities. The narrow window aperture (4.5 Å) to reach the cages of the of Ga<sup>3+</sup>-socMOF may have an influence on the breakthrough capacity and selectivity. Al<sup>3+</sup>-socMOF was shown to be stable up to temperatures as high as 300 °C and relative humidity as high as 95%, and even soaking in liquid water for 2 weeks did not affect the XRD pattern. However, the H<sub>2</sub>O stability of the Ga<sup>3+</sup>-socMOF was not reported. These materials show promise for regenerative sour gas sweetening using MOFs.

Stability of adsorbent in the corrosive environment of acid gases in the presence/absence of moisture is arguably the most important test that the adsorbent must meet in order to qualify as a potential candidate for sweetening applications. The not-so-strong coordination bond between the metal and the organic ligand in a MOF structure make it very susceptible to hydrolysis and poor stability. Burtch et al. have recently published a very detailed paper in *Chemical Reviews* on the hydrothermal stability of MOFs.<sup>198</sup> Apart from a few studies on acid gas stability of certain MOFs,<sup>199</sup> this area is not very mature for a comprehensive review. Future efforts in this direction will not only help advance the development of adsorbents for commercial purposes but also enhance the fundamental understanding of MOF stability.

Zeolitic imidazolate frameworks (ZIFs), a sub-class of MOFs, composed of transition metal ions that replace the silicon/aluminum atoms in a zeolite topology and organic linkers in place of the oxygen atoms in the zeolite lattice, are a relatively new type of materials that benefit from the structural variety of MOFs and stability of zeolites.<sup>200,201</sup> ZIF-8, with a BET surface area of 1630 m<sup>2</sup>/g, a high thermal stability (up to 550 °C), and remarkable chemical resistance to boiling alkaline water and organic solvents,<sup>201</sup> is one of the very extensively studied ZIF materials in the literature. Recently, Ethiraj et al. investigated the stability of HKUST-1 and ZIF-8 MOFs in an H<sub>2</sub>S environment using various techniques, including XRD, and observed a significantly higher stability of ZIF-8 over HKUST-1.<sup>192</sup> Other microporous materials, such as covalent organic frameworks<sup>202</sup> and porous aromatic frameworks,<sup>203</sup> that are low-density, high-surface-area materials but do not contain any selective metallic sites, can be explored for bulk H<sub>2</sub>S removal.

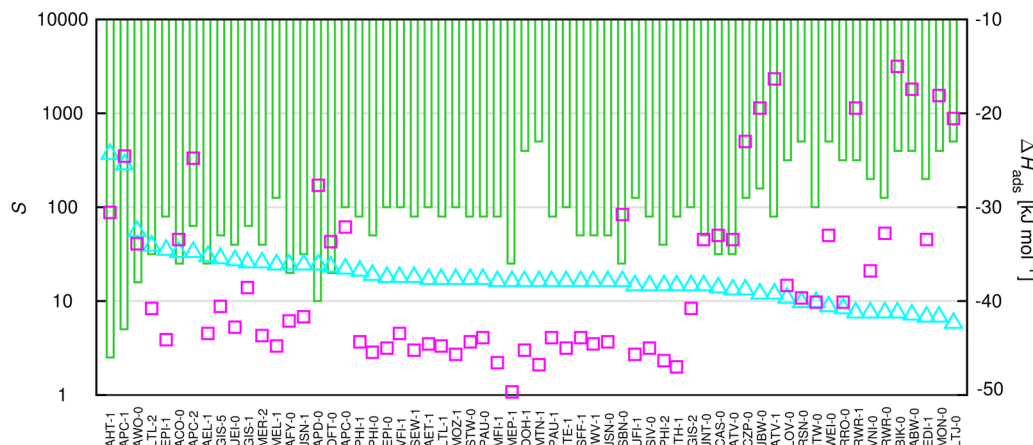


**Figure 10.** Selectivity (left axis) and  $\Delta H_{\text{ads}}$  (right axis) in top-performing zeolite structures at  $y_F = 0.50$ ,  $T = 343$  K, and  $p = 50$  bar.  $S_{\text{H}_2\text{S}/\text{CH}_4}$  cyan triangles,  $S_{\text{H}_2\text{S}/\text{C}_2\text{H}_6}$  magenta squares, and  $\Delta H_{\text{ads}}$  (for the  $\text{H}_2\text{S}/\text{CH}_4$  mixture) green bars. Reprinted with permission from ref 205. Copyright 2016 John Wiley & Sons, Inc.

As noted earlier, feed streams with varying overall pressure as well as concentration of  $\text{H}_2\text{S}$  are likely to require very different sweetening procedures. While low-concentration (10–1000 ppm) breakthrough measurements provide important data for applications such as Claus tail gas cleanup, data at higher  $\text{H}_2\text{S}$  partial pressures are also important for applications involving ultra-sour gas streams. A major difficulty in drawing a fair comparison between different MOFs in the literature for  $\text{H}_2\text{S}$  adsorption arises due to the unavailability of complete adsorption data over a wide range of partial pressures, from a few ppm at atmospheric pressure to 100%  $\text{H}_2\text{S}$  at several atmospheres in the presence/absence of moisture, different definitions of breakthrough capacity, etc. Future studies should account for factors such as moisture, regeneration for several cycles, and XRD measurements before and after each (or at least, after every few) regeneration.

### 3.4. Zeolites

For several decades, zeolites have been used as catalysts in the petrochemical industry for cracking, isomerization, and alkylation applications. These materials are also widely used for water purification and softening in the detergent industry. Structurally, zeolites are crystalline porous aluminosilicates consisting of a three-dimensional framework of  $\text{SiO}_4$  and  $\text{AlO}_4$  tetrahedra. Their pores are defined by their crystal structure and have precise sizes and shapes, allowing them excellent sieving properties at a molecular level. As of today, the database of the International Zeolite Association—Structure Commission identifies 232 unique zeolite frameworks, and each framework is represented by a three-letter code.<sup>204</sup> The International Union of Pure and Applied Chemistry classifies nanoporous materials into three classes: microporous (<2 nm), mesoporous (2–50 nm), and macroporous (>50 nm). Zeolites are microporous in nature, and depending on the particular framework structure, the maximum diameter of a sphere that can diffuse through the zeolite framework can range from 1 to 8 Å. The maximum diameter of a sphere that can be included in the zeolite structures can range from 3 to 16 Å.

**3.4.1. All-Silica Zeolites.** All-silica zeolites have a very low polarity due to negligible amounts of polar cations and silanol defects, imparting a highly hydrophobic character to this class of zeolites.<sup>206</sup> Maghsoudi et al. first investigated pure-component adsorption of  $\text{H}_2\text{S}$  and  $\text{CH}_4$  in an all-silica zeolite

of the chabazite (CHA) framework.<sup>207</sup> This material demonstrated a high  $\text{H}_2\text{S}$  capacity of 4 mmol/g at 25 °C and 2 bar, suggesting that all-silica zeolites maybe promising materials for bulk  $\text{H}_2\text{S}$  removal. Shah et al. carried out Monte Carlo simulations of  $\text{H}_2\text{S}$  and  $\text{CH}_4$ , both pure-component and mixture, over a wide range of temperatures, pressures, and compositions in seven different all-silica zeolites.<sup>208</sup> The authors showed quantitative agreement between predictive molecular simulations without any fitting parameters and the experimental data reported by Maghsoudi et al., thus validating the force fields for  $\text{H}_2\text{S}$ ,<sup>209</sup>  $\text{CH}_4$ ,<sup>210</sup> and the zeolite.<sup>211</sup> Shat et al. also assessed the application of ideal adsorbed solution theory (IAST) to pure-component data in order to predict mixture data and found differences as high as 60% in case of some zeolites. In order to probe whether the presence of  $\text{H}_2\text{S}$  induces  $\text{H}_2\text{O}$  coadsorption and reduces the hydrophobic character of all-silica zeolites, binary  $\text{H}_2\text{S}/\text{H}_2\text{O}$  mixture adsorption in MFI was also studied. The simulations showed preferential adsorption of  $\text{H}_2\text{S}$  over  $\text{H}_2\text{O}$  with a selectivity of about 18, suggesting that these zeolites can be promising materials for sour gas sweetening. In a subsequent study, Shat et al. carried out a large-scale computational screening of the adsorption of binary  $\text{H}_2\text{S}/\text{CH}_4$  and  $\text{H}_2\text{S}/\text{C}_2\text{H}_6$  mixtures in the all-silica forms of 386 zeolitic frameworks (see Figure 10).<sup>205</sup> The authors also investigated the adsorption of four- and five-component mixtures at the conditions representing sour gas fields for 16 promising all-silica zeolites selected from binary adsorption selectivities and capacities. It was found that, depending on the fractions of  $\text{CH}_4$ ,  $\text{C}_2\text{H}_6$ , and  $\text{CO}_2$ , different sorbents allow for optimal  $\text{H}_2\text{S}$  removal and hydrocarbon recovery.

Liu et al. carried out a multi-scale modeling study for combined material screening and process optimization to reduce the overall process cost with atomistic and mesoscopic scales for the selection of zeolites and the macroscopic scale for the selection of optimal conditions for pressure swing adsorption.<sup>212</sup> Several high-performing zeolites were identified, and zeolite ABW ranks as one of the top materials for the removal of both  $\text{H}_2\text{S}$  and  $\text{CO}_2$  (acid gases) from natural gas. There is a considerable degree of overlap between the zeolites identified from the two screening studies in the literature for high  $\text{H}_2\text{S}/\text{CH}_4$  selectivities.<sup>205,212</sup> The best-performing zeolites will likely always be from this pool of structures identified with high selectivity over methane; however, the optimal adsorbent

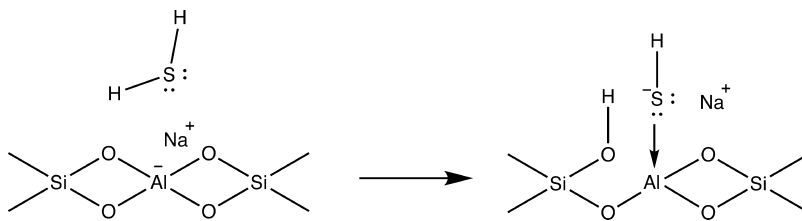


**Figure 11.** Schematic of dissociative  $\text{H}_2\text{S}$  adsorption on an aluminosilicate zeolite.

will depend on the feed conditions (wet/dry, lean/rich in light hydrocarbons,  $\text{CO}_2/\text{H}_2\text{S}$  proportions).

Of all the top-performing structures presented in Figure 10, CAS, DOH, ITE, ITH, ITW, MEL, MEP, MFI, MTN, RRO, RWR, and SFF frameworks have been synthesized in their all-silica form, IWV with a Si/Al ratio of 29, SEW with a Si/B ratio of 13, and ABW, BIK, EDI, EPI, GIS, JBW, LTJ, LTL, MER, MON, MOZ, PAU, PHI, and UFI with a low to moderate Si/Al ratio.<sup>205</sup> Although DOH, MEP, and MTN show a high selectivity, it is unlikely that the pores in these structures with only six-membered ring openings will allow accessibility to the selective sites. Development of experimental syntheses for the all-silica defect-free forms of these top-performing zeolite topologies can further the development of these hydrophobic adsorbents for the bulk acid gas removal from ultra-sour gas fields.

**3.4.2. Aluminosilicate Zeolites.** Aluminosilicate zeolites are crystalline microporous frameworks, based on a three-dimensional network of silica and alumina, that can accommodate a variety of cations such as  $\text{Na}^+$ ,  $\text{K}^+$ ,  $\text{Ca}^{2+}$ , etc. In addition to the precise sizes and shapes of pores in all-silica zeolites that allow them excellent sieving properties at a molecular level, the cations in aluminosilicate zeolites may allow the possibility of strong selective interactions with the desired polar gas molecules. There is a significant amount of literature exploring the Claus reaction between  $\text{H}_2\text{S}$  and  $\text{SO}_2$  to produce elemental sulfur using cation-exchanged zeolites.<sup>213,214</sup> While this is a very important aspect of sour gas sweetening, it has been reviewed in the past,<sup>20</sup> and we will focus here on the interaction of these zeolites with  $\text{H}_2\text{S}$  in the absence of oxygen.

Ozekmekci et al. have presented a short review on  $\text{H}_2\text{S}$  removal using zeolites.<sup>215</sup> We try to expand on this subject here. Identifying the adsorption mechanism of  $\text{H}_2\text{S}$  in cation-exchanged zeolites has been a challenge, whether it is a physisorption, chemisorption by coordination to the cations, or a chemical reaction forming  $\text{H}_2\text{O}$  using either framework oxygen or gas-phase oxygen impurities or possibly even metal oxides of the extra-framework cations. In an attempt to understand the adsorption mechanism, several zeolitic systems based on faujasite (FAU; NaX, NaY, HY), LTA (NaA, CaNaA, ZnNaA, MnNaA, CoNaA, NiNaA, CuNaA), and MFI (H-ZSM-5, Na-ZSM-5) were probed using IR,<sup>216–221</sup> UV-vis,<sup>219</sup> and nuclear magnetic resonance (NMR) spectroscopies.<sup>222</sup>

On aluminum-rich FAU up to Si/Al ratios of about 2.5 (NaX zeolites), the first  $\text{H}_2\text{S}$  molecules are adsorbed dissociatively, producing OH groups ( $3650 \text{ cm}^{-1}$ ) similar to those of hydrogen FAU; however, NaY-type zeolites with Si/Al > 2.5 adsorb the  $\text{H}_2\text{S}$  molecules practically without dissociation.<sup>218</sup> Similar conclusions were also reported by Lechert and Henning using the NMR technique.<sup>222</sup> The first molecules adsorbed on NaX dissociated completely with formation of  $\text{S}^{2-}$  and  $2\text{OH}$ , but at higher coverages, dissociation into  $\text{HS}^-$  and  $\text{H}^+$  (see Figure 11) as well as physical adsorption occurs.<sup>219</sup> Four times

higher  $\text{H}_2\text{S}$  adsorption capacities for X-type zeolites than for Y-type zeolites were observed; moreover, the uptake changed in the following sequence: K-FAU > Na-FAU > Li-FAU, suggesting that  $\text{H}_2\text{S}$  adsorption improves with FAU basicity.<sup>223</sup> Garcia and Lercher studied adsorption of  $\text{H}_2\text{S}$  in ZSM-5 zeolites (Si/Al = 35.5) and observed molecular adsorption on both Na- and H-ZSM-5 zeolite surfaces.<sup>221</sup> In conclusion, lower Si/Al ratios promote dissociative adsorption of  $\text{H}_2\text{S}$  on cation-exchanged zeolites. Recently, Sigot et al. attempted to investigate the retention mechanism of  $\text{H}_2\text{S}$  on NaX zeolites with Si/Al ratio of 1.4.<sup>224</sup> The authors observed poor thermal desorption at  $350^\circ\text{C}$ , indicating no physisorption and the formation of stable sulfur polymers which further compromised thermal regeneration.

The SH vibration band of  $\text{H}_2\text{S}$  adsorbed on NaA showed a large frequency shift; however, in the case of CaNaA, over a wide range of coverage, the characteristic frequency of the SH band remained constant at  $2540 \text{ cm}^{-1}$ .<sup>217</sup> Thus, the authors concluded that no significant sorbate–sorbate interactions occur and that all  $\text{H}_2\text{S}$  molecules occupy equivalent sites in the case of CaNaA. No bands corresponding to adsorbed species were observed for NiNaA and CuNaA, and CoNaA adsorbed non-dissociatively, while ZnNaA and MnNaA demonstrated both dissociative and non-dissociative adsorption.<sup>220</sup> In agreement with previous studies of  $\text{H}_2\text{S}$  adsorption on various zeolites,<sup>216–218</sup> water formation was observed on adsorption of  $\text{H}_2\text{S}$  onto MnNaA, ZnNaA, and CoNaA. It is not very clear, however, whether  $\text{H}_2\text{O}$  is formed using either framework oxygen or oxygen impurities in the gas feed. It is unclear if metal oxide clusters of the exchanged cations are present in the system and whether these form a source of oxygen for water formation. Very recently, Wynnyk and co-workers carried out precise and detailed measurements up to high pressures for adsorption of sour gas species ( $\text{CO}_2$ , COS,  $\text{CH}_4$ , and  $\text{H}_2\text{S}$ ) on zeolite 4A (LTA) with Si/Al ratios between 1.14 and 1.15 and activated under ultra-high vacuum ( $10^{-10} \text{ bar}$ ) up to  $400^\circ\text{C}$ .<sup>183</sup> The adsorption isotherms of these compounds were found to be quite different, with saturation loadings extrapolated from the fitted adsorption isotherm for  $\text{CH}_4$ ,  $\text{CO}_2$ ,  $\text{H}_2\text{S}$ , and COS being 9.16, 7.25, 5.87, and 3.11 mmol/g, respectively. The low saturation capacity of COS was not expected; computational calculations for HOMO bond orientation indicated that COS should be excluded from zeolite 4A, despite the experimental results. The reason for decreasing saturation loadings for  $\text{CO}_2$  with decreasing temperatures (0, 25, and  $50^\circ\text{C}$ ) was not explained by the authors. The authors also calculated the enthalpy of adsorption using isotherms at different temperatures; at low loadings,  $\text{CH}_4$  and COS yield similar values of 20 kJ/mol, while  $\text{CO}_2$  and  $\text{H}_2\text{S}$  interact more strongly, with values of  $\sim 35 \text{ kJ/mol}$  (near saturation loading). These enthalpies of adsorption seem too small to suggest a chemisorption behavior; however, it should be noted that these interactions can be

sensitive to even trace amounts of  $\text{H}_2\text{O}$  that may accompany the feed gas.

$\text{H}_2\text{S}$  adsorption on cluster models of metal-exchanged ZSM-12 ( $M = \text{Fe}, \text{Co}, \text{Ni}, \text{Cu}, \text{and Zn}$  atoms) was investigated using DFT calculations, and the reported enthalpies of adsorption were  $-77, -77, -90, -58$ , and  $-76 \text{ kJ/mol}$ , respectively.<sup>225</sup> This suggests that Ni binds most strongly to  $\text{H}_2\text{S}$ , while the binding with Cu is the weakest. One can see that the trends for different metals are not the same as reported for cation-exchanged LTA zeolites described above.<sup>220</sup> A key issue here is that we are not certain of the fraction of the cations in the ion-exchanged sites versus that in the metal oxide form. Several other factors, such as difference in the confinement of LTA and MTW zeolites for the same metallic species, presence of impurities in experimental measurements, or inadequate level of theory to describe the system using DFT, can also contribute to the different trends in the two zeolite types. In the absence of more data, it is hard to draw concrete conclusions about the affinity of various transition metal cations toward  $\text{H}_2\text{S}$ .

SAPO-43, a small-pore silicoaluminophosphate, is a microporous sorbent with appropriate dimensions for sour gas sieving; however, its low thermal stability up to about  $300^\circ\text{C}$  prevents its utilization for adsorptive separations. Elemental analysis and  $\text{CO}_2$  heats of adsorption point to the presence of amine-like compounds entrapped in the surface of SAPO-43, which are believed to keep the framework from collapsing.<sup>226</sup> Hernández-Maldonado et al. demonstrated the use of partially calcined SAPO-43 to separate  $\text{CO}_2$ ,  $\text{H}_2\text{S}$ , and  $\text{H}_2\text{O}$  from natural gas.<sup>226</sup> Regeneration with pure helium at  $180^\circ\text{C}$  was sufficient to remove almost all of the adsorbed water, but only 40% of the adsorption capacity was restored for  $\text{H}_2\text{S}$ . The authors suggest that regeneration using chemicals such as hydrogen peroxide ( $\text{H}_2\text{O}_2$ ) may help in entirely removing  $\text{H}_2\text{S}$  without the need to thermally regenerate the adsorbent.

Crespo et al. compared the  $\text{H}_2\text{S}$  breakthrough capacities among  $\text{Cu(I)Y}$ ,  $\text{Cu(II)Y}$ ,  $\text{CuCl/MCM-41}$ ,  $\text{CuCl/SBA-15}$ , and  $\text{AgY}$ .<sup>227</sup> It was found from both *ab initio* molecular orbital calculations and the experimental temperature dependence of adsorption isotherms that the energy of adsorption decreased in the following order:  $\text{Cu(I)Y} > \text{AgY} > \text{Cu(II)Y}$ . The chemical composition of AgY zeolites,  $\text{Ag}_{63}\text{Al}_{57}\text{Si}_{135}\text{O}_{384}$ , clearly shows that the Ag/Al ratio is greater than unity; this suggests that some of the cations are located at sites other than the cation-exchange sites. Structural characterization of cation-exchanged zeolites<sup>228</sup> may help in better understanding some of the anomalies in trends in affinity of  $\text{H}_2\text{S}$  toward various cations. Nearly 70% regeneration of  $\text{Cu(I)Y}$  zeolite was achieved by heating at  $450^\circ\text{C}$  in a helium environment, and 100% regeneration could be accomplished by reacting with air at  $350^\circ\text{C}$ ; this is another indication of cations in their oxide form. With a high  $\text{H}_2\text{S}$  capacity at concentrations as low as 100 ppm, high selectivity over  $\text{CH}_4$ , and being fully regenerable at a moderate temperature ( $350^\circ\text{C}$ ),  $\text{Cu(I)Y}$ ,  $\text{CuCl/SBA-15}$ , and  $\text{CuCl/MCM-41}$  materials hold some promise for natural gas desulfurization.

In addition to the  $\text{H}_2\text{S}$  impurity, most natural gas fields also contain other impurities such as  $\text{CO}_2$ ,  $\text{CO}$ , and  $\text{H}_2\text{O}$ , and these polar molecules may have a tendency to compete with, and sometime even supersede,  $\text{H}_2\text{S}$  adsorption. Kumar et al. carried out a detailed investigation of such mixture systems for Na-, Ag-, and Cu-exchanged FAU at high and low Si/Al ratios (see Figure 12).<sup>229</sup> The authors report a nearly complete loss in  $\text{H}_2\text{S}$  adsorption capacity for NaX zeolite in the presence of either

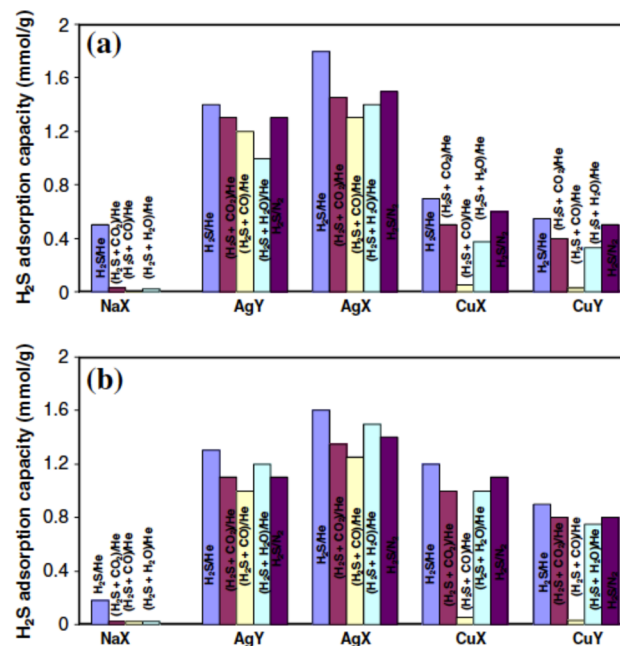


**Figure 12.**  $\text{H}_2\text{S}$  adsorption capacities of NaX, AgY, AgX, CuX, and CuY zeolites for 10 ppmw  $\text{H}_2\text{S}$  in He and  $\text{N}_2$  in the absence and presence of  $\text{CO}_2$  (20%),  $\text{CO}$  (2%), and  $\text{H}_2\text{O}$  (2%) in the feed at (a) room temperature and (b)  $150^\circ\text{C}$ . Reprinted with permission from ref 229. Copyright 2011 Elsevier.

$\text{CO}_2$ ,  $\text{CO}$ , or  $\text{H}_2\text{O}$ , while CuX and CuY showed similar losses in selectivity in the presence of CO. AgX and AgY zeolites maintained  $\text{H}_2\text{S}$  capacities of about 30–40 mg/g at 10 ppm  $\text{H}_2\text{S}$ , even in the presence of all three impurities. The authors could also explain the observed experimental trends using DFT calculations; comparisons of the structures and energetics between the cluster and periodic calculations led to the conclusion that the confinement effect from the complete zeolitic framework is insignificant for the adsorbates studied. Further DFT calculations showed that, while the presence of the zeolite does not change radically the trend in the adsorption energies for alkali metal cations, in the case of transition metal cations it enhances the CO adsorption markedly relative to all other adsorbates.<sup>230</sup> The authors also investigated other cation-exchanged zeolites such as  $\text{Zn(II)Y}$ ,  $\text{Ni(II)Y}$ , and  $\text{Ga(III)Y}$  and found that they are all subject to strong adsorption of  $\text{H}_2\text{O}$ .<sup>231</sup> It should be noted here that strict ion exchange (without formation of metal oxides) has not been demonstrated for these cations.

In addition to the competitive adsorption in the presence of impurities, Bülow and co-workers reported on reactive adsorption of  $\text{H}_2\text{S}$  and  $\text{CO}_2$  on cation-exchanged LTA and FAU zeolites.<sup>232–234</sup> Due to strongly preferred sorption of  $\text{H}_2\text{O}$  on these zeolites ( $\text{H}_2\text{O} \gg \text{H}_2\text{S} \geq \text{CO}_2 \approx \text{COS}$ ), the equilibrium of the reaction  $\text{H}_2\text{S} + \text{CO}_2 \rightleftharpoons \text{COS} + \text{H}_2\text{O}$  is shifted to the right. As a result, one sulfur-containing species ( $\text{H}_2\text{S}$ ) is transformed to another (COS), with nearly zero enrichment of sulfur on the molecular sieve. The authors have extensively studied different variations of the adsorbent such as type of zeolite, Si/Al ratio, choice of cation for exchange, degree of ion exchange (percentage of  $\text{Na}^+$  exchanged), and presorption of  $\text{NH}_3$ . At room temperature,  $\text{H}_2\text{S}$  conversion on LTA can be as high as 50% for a Si/Al ratio of 1, and drops to nearly zero for a Si/Al ratio of 3.<sup>232</sup> At higher degrees of ion exchange, there is a considerable kinetic barrier, and one can

observe H<sub>2</sub>S conversions anywhere between 20 and 75%, depending on the reaction time.<sup>232,233</sup> Thus, in the absence of any known method to suppress this reaction, the authors suggest short-time techniques such as PSA/VSA.<sup>234</sup> This study suggests that future investigations of H<sub>2</sub>S breakthrough behavior in cationic zeolites should also monitor COS breakthrough.

**3.4.3. Titanosilicates.** In 1989, several synthetic titanosilicates were introduced as oxides or molecular sieves that have not only tetrahedrally coordinated sites that are characteristic of zeolites such as aluminosilicates or aluminophosphates but also octahedrally coordinated framework sites.<sup>235</sup> These materials possess moderately high surface areas ( $S_{\text{BET}} \approx 200 \text{ m}^2/\text{g}$ ), and if active metals are well-dispersed on these supports, high metal utilization for reactive adsorption can be attained. Rezaei et al. have recently investigated low-temperature reactive H<sub>2</sub>S removal using copper-exchanged Engelhard titanosilicates (ETS-2, ETS-4, ETS-10).<sup>236</sup> While ETS-4 and ETS-10 are microporous, ETS-2 is most probably just a layered titanate and is too dense to be considered a molecular sieve.<sup>235</sup> Cu-ETS-2, Cu-ETS-4, and Cu-ETS-10 show H<sub>2</sub>S breakthrough capacities of 1.4, 0.32, and 1.3 mmol/g and copper utilization of 71, 44, and 98%, respectively. The high and low copper utilization in ETS-10 and ETS-4 has been attributed to their large and small pores, respectively, leading to pore blockage by adsorbed H<sub>2</sub>S in case of ETS-4. Since ETS-10 allows near complete utilization of copper sites at 8.4 wt% copper loading, higher loadings should be investigated to possibly improve breakthrough capacities. In a follow-up work, the authors investigated the effect of exchange metals such as Ag, Ca, Cu and Zn on ETS-2 and compared to a fully developed commercial H<sub>2</sub>S adsorbent (R3-11G, 36 wt% CuO, BASF).<sup>237</sup> The results indicated H<sub>2</sub>S uptake capacities in the following order: Cu-ETS-2 > Ag-ETS-2 > Zn-ETS-2 ≈ R3-11G > Ca-ETS-2 ≈ Na-ETS-2. In a recent study, Roller et al. studied Cu-ETS-2, Ce-ETS-2, and Cu-Ce-ETS-2 over a wide range of temperatures and under hydrogen-rich and water-rich atmospheres and found that, contrary to Ce-modified sorbents in the literature,<sup>153</sup> Ce-based ETS-2 showed a very low H<sub>2</sub>S breakthrough capacity.<sup>238</sup>

### 3.5. Carbon-Based Adsorbents

**3.5.1. Activated Carbons.** Activated carbon (AC) with surface areas easily in excess of 1000 m<sup>2</sup>/g due to a high degree of microporosity is a well-known material for adsorption and catalysis. It is most commonly manufactured by carbonizing easily available carbon sources such as coconut shell, wood, coal, etc. at high temperatures in an inert atmosphere. The resultant coke has pores too small for use as an adsorbent, and usually steam activation is carried out to enlarge the pore structure, making it accessible for adsorption. Several studies have been reported in the literature on the use of ACs for H<sub>2</sub>S adsorption as well as Claus reaction between H<sub>2</sub>S and O<sub>2</sub> to form elemental sulfur. Unlike crystalline materials such as MOFs and zeolites, ACs are amorphous and hence characterized using N<sub>2</sub> adsorption, pH measurements, thermal analysis, ion chromatography, elemental analysis, and FTIR techniques. It is nearly impossible to rationalize the large amounts of data in this field with various carbon sources, activation conditions, pH of adsorption, and presence of unidentifiable impurities in the ACs. An attempt is made to highlight some of the studies that show high adsorption of H<sub>2</sub>S, but the reasons for most of these are not well-understood.

Turk et al. have demonstrated the injection of basic chemicals such as ammonia and caustic solutions to enhance H<sub>2</sub>S adsorption.<sup>239,240</sup> There are numerous investigations from the Bandosz group on removal of H<sub>2</sub>S using ACs that differ in their surface areas, pore volumes, and surface acidities.<sup>241–246</sup> The heat of H<sub>2</sub>S adsorption on a variety of ACs, differing in surface chemistry, pH, or the presence of specific oxygenated groups, was shown to be between 39 and 47 kJ/mol, about 2 times that obtained for a nonporous surface.<sup>242</sup> Adib et al. tried to increase the basicity of AC by impregnating it with urea; however, the H<sub>2</sub>S conversion decreased by about 10% from 298 to 272 mg/g for the impregnated samples compared to the initial sample, possibly due to an 18% decrease in surface area on urea impregnation.<sup>244</sup> Tian et al. chemically modified the surface of AC using 3-aminopropyltriethoxysilane (APTES), thus imparting a basic character to the sorbent with the goal of enhancing interaction with acidic H<sub>2</sub>S.<sup>247</sup> The authors observed poor breakthrough capacities of <1 mg/g at 1600 ppm, maybe due to blockage of pores because of the bulky APTES impregnation. At 8200 ppm the equilibrium adsorption capacity of H<sub>2</sub>S is 18.13, 8.88, and 6.03 mg/g for APTES-AC, Na<sub>2</sub>CO<sub>3</sub>-AC, and AC, respectively. Moisture and temperature were found to have adverse effects on H<sub>2</sub>S removal, while oxygen favored H<sub>2</sub>S removal. The negative role of humidity in this study is contradictory to previous studies of H<sub>2</sub>S adsorption on AC,<sup>241</sup> while the positive effect of oxygen has been explained by the authors to be due to the catalytic role of oxygen during oxidation.

Regeneration of ACs using cold and hot water washing and using heating at 300 °C in air atmosphere showed that, after the first adsorption run, the capacity of carbon for hydrogen sulfide adsorption significantly decreased (around 60%) due to irreversible adsorption in the most active adsorption cites located in small pores; subsequent runs revealed a more or less constant capacity.<sup>248,249</sup> Boudou et al. could regenerate the H<sub>2</sub>S-adsorbed AC sorbents by heating for 10 min in flowing N<sub>2</sub> at 500 °C.<sup>250</sup> Although inert atmosphere can be maintained at laboratory scales, the possibility of self-ignition at such high temperatures of regeneration cannot be eliminated. Aging of ACs has shown that the sorbents having significant capacity after the first adsorption run are practically unwashable with water due to the deposition of bulky sulfur polymers that are resistant to oxidation.<sup>251</sup>

**3.5.2. Structured Carbons.** Structured nanoporous carbon materials may be broadly classified into two main kinds: graphene-based materials and carbon nanotubes (CNTs). Graphene is an allotrope of carbon that consists of a two-dimensional hexagonal lattice of single atomic layer of sp<sup>2</sup>-hybridized carbon atoms. Graphene-based materials may be further classified as pristine graphene, graphene oxide (GO), and reduced graphene oxide (rGO).<sup>252</sup> CNTs are cylindrical nanostructures that may be imagined as seamlessly rolled-up graphene sheets with channel diameters as small as 0.4 nm,<sup>253</sup> ~1.4 nm in several studies,<sup>254</sup> and can be as high as 50 nm.<sup>252</sup> The CNTs can be open or closed with half-fullerene caps at either ends of the cylindrical structure. These single-walled CNTs (SWCNTs) are usually observed as closely packed bundles on a honeycomb lattice with typically 100 nanotubes (of 1.4 nm diameter) forming bundles of <20 nm diameter.<sup>255</sup> The adsorption sites in SWCNT bundles maybe classified into three kinds: inside each tube, interstitial channels between the tubes, and outer surface peripheral to the bundle. The surface area for these materials may range from over 2500 m<sup>2</sup>/g for a

**Table 9.** H<sub>2</sub>S Breakthrough Capacities and Percentage of Theoretical Capacity Utilized in Metal Oxides Supported on Silica

adsorbent	mg S/g sorbent	% utilization	T (°C)	composition	reference
0.50%Zn-SBA-15	39	1600	25	0.1% H <sub>2</sub> S in air	Wang et al. <sup>275</sup>
1.24%Zn-SBA-15	65	1100			
3.04%Zn-SBA-15	220	1500			
4.45%Zn-SBA-15	42	190			
9.00%Zn-SBA-15	34	80			
0.58%Fe-SBA-15	97	2900	25	0.1% H <sub>2</sub> S in air	Wang et al. <sup>276</sup>
1.36%Fe-SBA-15	120	1600			
3.59%Fe-SBA-15	170	810			
7.14%Fe-SBA-15	190	470			
11.4%Fe-SBA-15	190	300			
19.6%Fe-SBA-15	240	210			
31.3%Fe-SBA-15	320	180			
BASF ZnO	11	3.3	25	1–2% H <sub>2</sub> S, 33% CO or CO <sub>2</sub> in H <sub>2</sub>	Dhage et al. <sup>277,278</sup>
Sud-Chemie ZnO	24	7.1			
16.9%Zn-SiO <sub>2</sub>	51	62			
16.9%Zn-SiO <sub>2</sub>	53 <sup>s</sup>	64			
12.1%Zn-SiO <sub>2</sub>	32 <sup>s</sup>	54			
0.82%Cu-16.0%Zn-SiO <sub>2</sub>	77 <sup>s</sup>	93			
0.82%Cu-16.0%Zn-SiO <sub>2</sub>	51 <sup>0</sup> –17 <sup>1</sup> –37 <sup>5</sup> –17 <sup>9</sup>	62 <sup>0</sup> –21 <sup>1</sup> –45 <sup>5</sup> –21 <sup>9</sup>			
0.59%Cu-11.4%Zn-SiO <sub>2</sub>	43 <sup>s</sup>	73			
3.28%Cu-13.5%Zn-SiO <sub>2</sub>	78 <sup>s</sup>	94			
2.34%Cu-9.64%Zn-SiO <sub>2</sub>	45 <sup>s</sup>	76			
0.71%Mn-16.0%Zn-SiO <sub>2</sub>	50 <sup>s</sup>	61			
0.72%Fe-16.0%Zn-SiO <sub>2</sub>	69 <sup>s</sup>	84			
0.76%Co-16.0%Zn-SiO <sub>2</sub>	64 <sup>s</sup>	78			
0.76%Ni-16.0%Zn-SiO <sub>2</sub>	53 <sup>s</sup>	64			
ZnO (commercial)	29 <sup>0</sup> –3.2 <sup>1</sup>	6.6 <sup>0</sup> –0.73 <sup>1</sup>	20	2% H <sub>2</sub> S in H <sub>2</sub>	Yang and Tatarchuk <sup>279</sup>
13.7%Zn-SiO <sub>2</sub>	14 <sup>0</sup> –13 <sup>1</sup>	22 <sup>0</sup> –20 <sup>1</sup>			
0.66%Cu-13.0%Zn-SiO <sub>2</sub>	28 <sup>0</sup> –22 <sup>1</sup>	42 <sup>0</sup> –33 <sup>1</sup>			
0.62%Co-13.0%Zn-SiO <sub>2</sub>	14	21			
0.61%Ni-13.0%Zn-SiO <sub>2</sub>	17	25			
0.57%Mn-13.0%Zn-SiO <sub>2</sub>	17	25			
1.13%Ag-13.0%Zn-SiO <sub>2</sub>	28	42			
BASF ZnO	11	3.3	25	1% H <sub>2</sub> S in H <sub>2</sub>	Dhage et al. <sup>280</sup>
Sud-Chemie ZnO	24	7.1			
12.1%Zn-SiO <sub>2</sub>	26	44			
0.26%Fe-11.75%Zn-SiO <sub>2</sub>	35	59			
0.25%Mn-11.75%Zn-SiO <sub>2</sub>	37	63			
0.25%Fe-0.25%Mn-11.45%Zn-SiO <sub>2</sub>	37 <sup>0</sup> –20 <sup>5</sup> –37 <sup>9</sup> –23 <sup>10</sup>	63 <sup>0</sup> –34 <sup>5</sup> –63 <sup>9</sup> –39 <sup>10</sup>			
12%Zn-MCM-41	9.6	16	25	200 ppm H <sub>2</sub> S in H <sub>2</sub>	Hussain et al. <sup>281</sup>
16%Zn-KIT-6	9.1	12			
12%Zn-SBA-15-sphere	21	36			
12%Zn-SBA-15-fiber	22	37			
2.4%Zn-TNP (TiO <sub>2</sub> NP)	5	43			
8.0%Zn-ROZ3 (AC Norit)	8	20			
11.2%Cu-6%Zn-SBA-15	75	87	150	102 ppm H <sub>2</sub> S in He	Elyassi et al. <sup>282</sup>
10.6%Cu-5%Zn-SiO <sub>2</sub>	34	44			
10%Cu-MSU-1	11	22	25	5% H <sub>2</sub> S in CH <sub>4</sub>	Montes et al. <sup>283</sup>
20%Cu-MSU-1	19	19			
30%Cu-MSU-1	19	13			
10%Zn-MSU-1	42	86			
20%Zn-MSU-1	15	15			
30%Zn-MSU-1	12	7.8			

Table 9. continued

adsorbent	mg S/g sorbent	% utilization	T (°C)	composition	reference
24%Zn-SiO <sub>2</sub>	3.8 46 $96^0-61^1-65^2-53^3-52^4-53^5$	3.2 39 $81^0-52^1-55^2-45^3-44^4-45^5$	200 300 400	100 ppm H <sub>2</sub> S in N <sub>2</sub>	Liu et al. <sup>284</sup>
Katalco 32-5	$13^0-3^1-3^2$	0.68	300	1.5% H <sub>2</sub> S in He	Mureddu et al. <sup>285</sup>
IWI-24.1%Zn-SBA-15	$9^0-15^1-18^2$	15			
TS-24.1%Zn-SBA-15	$9^0-12^1-12^2$	10			
Katalco 32-5	$6^0-2^1-2^2$	0.45	300	1.5% H <sub>2</sub> S in He	Mureddu et al. <sup>286</sup>
TS-14.5%Zn-SBA-15	$10^0-13^1-14^2$	20			
TS-11.2%Fe-SBA-15	$80^0-40^1-42^2$	65			
16.1%Zn-SBA-16	8.0	10	25	800 ppm H <sub>2</sub> S in N <sub>2</sub>	Li et al. <sup>287</sup>
24.1%Zn-SBA-16	5.7	4.8			
32.1%Zn-SBA-16	3.4	2.2			
8.03%Zn-MCM-48	4.6	12			
16.1%Zn-MCM-48	6.8	8.6			
24.1%Zn-MCM-48	15	13			
32.1%Zn-MCM-48	8.0	5.1			
8.03%Zn-KIT-6	11	29			
16.1%Zn-KIT-6	14	17			
24.1%Zn-KIT-6	38	32			
32.1%Zn-KIT-6	29	18			

<sup>a</sup>Key to superscripts: 0, fresh sample; *n* (= 1–5), after *n* cycles; s, saturation capacity.

SWCNT to as low as 800 m<sup>2</sup>/g for bundles of infinite diameter.<sup>255</sup> SWCNTs of varying channel diameters can also arrange in the form of several concentric cylinders to form multi-walled nanotubes (MWNTs).

Several groups have theoretically investigated the role of defects in the adsorption of H<sub>2</sub>S on the graphene surface, mainly for sensor applications.<sup>256–259</sup> Depending on the position of binding, adsorption energies of H<sub>2</sub>S on pristine graphene were found to be between 10 and 16 kJ/mol, but having a defect site with the sulfur atom of H<sub>2</sub>S pointing toward the defect resulted in a much stronger binding (88 kJ/mol).<sup>256</sup> In another study, three different graphene structures (pristine, with divacancy, and with the inclusion of nitrogen in graphene) were investigated, and the binding energies were found to be 1.6, 1.3, and 2.5 kJ/mol, respectively.<sup>257</sup> Borisova et al. investigated the effect of vacancy in graphene and found that H<sub>2</sub>S adsorbed by forming weak S–C covalent bonds with the atoms surrounding the single vacancy.<sup>258</sup> In addition to the single vacancy and divacancies in graphene described above, there can be several other defect types; one such defect is the Stone–Wales (SW) defect that has four hexagons fused into two alternating pentagons and heptagons. Hegde et al. studied H<sub>2</sub>S binding to the carbon site of pristine graphene, SW defect site, and BN sites of BN-doped graphene through first-principles DFT with van der Waals (vdW) interactions.<sup>259</sup> While the adsorption of H<sub>2</sub>S is weak at both C and BN sites, with a binding energy of 15 kJ/mol, it is significantly stronger at the SW defect site with a binding energy of 26 kJ/mol. In the relaxed geometries, the sulfur atom of H<sub>2</sub>S points toward graphene (at a distance 3.14 Å) at C and BN sites, while the molecule's H atoms point toward graphene (at a distance 2.84 Å) at the SW defect site. There seem to be significant differences in the various predictions for H<sub>2</sub>S adsorption on graphene; these differences may be due to different levels of

theories employed for the independent studies. A consistent treatment of all defect types will be important in order to understand, quantitatively, the role of graphene defects in H<sub>2</sub>S adsorption.

There are several studies employing DFT for adsorption of H<sub>2</sub>S on metal-doped graphene.<sup>256,260–265</sup> Strong adsorption was found due to a large binding energy (615 kJ/mol for 1 H<sub>2</sub>S/Pt system and 75 kJ/mol of H<sub>2</sub>S for the 7 H<sub>2</sub>S/Pt system) and short Pt–H<sub>2</sub>S bond length compared to those of the H<sub>2</sub>S/graphene system.<sup>260</sup> Zhang et al. reported binding energies of 16, 64, 174, and 185 kJ/mol for pristine, Ca-, Co-, and Fe-doped graphene, respectively.<sup>256</sup> Sharma and Verma calculated binding energies of 33, 42, 123, and 98 kJ/mol for pristine, B-, Al-, and Ga-doped graphene, respectively.<sup>261</sup> Pang et al. reported binding energies of 15, 81, 102, and 112 kJ/mol for pristine, Cr-, Cu-, and W-doped graphene, respectively.<sup>265</sup> These highly energetic interactions of H<sub>2</sub>S with metal-doped graphene are mainly of interest for sensor applications; however, they may have potential usefulness in adsorbents for ultra-deep sulfur removal of natural gas as the final polishing step for direct-methane fuel cells.<sup>170</sup>

The effect of the presence of S atom on graphene on the adsorption of H<sub>2</sub>S was investigated using DFT.<sup>266</sup> Two types of systems were investigated: S-functionalized graphene, where an S atom was added on pristine graphene, and S-doped graphene, where an S atom was added to the single-vacancy defect of graphene. Pristine graphene showed adsorption energies of 34 kJ/mol, while S-functionalized graphene showed energies as high as 170 kJ/mol due to covalent bond formation between S and H<sub>2</sub>S for configurations with H atoms pointing away from the graphene plane. Both physisorption and chemisorption were observed, depending upon C–S bond distances in the H<sub>2</sub>S/S-doped graphene complex before optimization.

Molecular simulations for adsorption on structured carbons in the literature give very inconsistent answers and use idealized structures that may not be experimentally realizable.<sup>267–270</sup> Neglect of electrostatic interactions for the adsorbent in studies involving polar sorbate molecules may result in incorrect predictions of sorbate–sorbent interactions. The potential of GO has not yet been extensively explored by molecular modeling, mainly due to the lack of an atomistic GO model for theoretical calculations.<sup>271</sup> Huang et al. have reported the controllable generation of atomistic GO models by a temperature-programmed reactive MD simulation. They further calculated the reactive adsorption of H<sub>2</sub>S and H<sub>2</sub>O/H<sub>2</sub>S mixtures on the as-generated atomistic GO structures.<sup>271</sup> H<sub>2</sub>S was observed to dissociate on the carbonyl functional groups, in agreement with the dynamic adsorption experiments; for the H<sub>2</sub>O/H<sub>2</sub>S mixtures, H<sub>2</sub>O molecules were preferentially adsorbed to the carbonyl sites, thus blocking the availability of active sites for H<sub>2</sub>S decomposition, again in agreement with the experimental findings.

Mohamadalizadeh et al. investigated the sorption of pure H<sub>2</sub>S on AC, MWNTs, CNTs decorated with tungsten nanoparticles (W-CNTs), and amino-functionalized CNTs (F-CNTs).<sup>272</sup> Although these CNT-based materials have a surface area ( $\sim 100 \text{ m}^2/\text{g}$ ) lower than that of AC ( $\sim 1000 \text{ m}^2/\text{g}$ ), the saturation capacities for these systems (at 10 bar and 20 °C) did not differ drastically, and CNTs showed better regenerability compared to AC.

### 3.6. Composite Materials

**3.6.1. Metal Oxides/Mesoporous Silica.** While metal oxide sorbents show high affinity for H<sub>2</sub>S, they suffer from limitations such as loss in surface area and porosity, and this subsequently results in degraded performance during cyclic sulfidation and regeneration. Ordered mesoporous molecular sieves that allow narrow pore sizes (16–100 Å) tailored through the choice of surfactant, auxiliary chemicals, and reaction conditions were first discovered in the early 1990s.<sup>273,274</sup> This seminal discovery enabling uniform pore sizes of mesoporous materials with high surface areas opened up a new area for novel heterogeneous catalysts.

Wang et al. for the first time investigated adsorption of H<sub>2</sub>S on metal-oxide-impregnated mesoporous silica, ZnO/SBA-15<sup>275</sup> and Fe<sub>2</sub>O<sub>3</sub>/SBA-15.<sup>276</sup> The breakthrough capacities mentioned by those authors are not in accord with the breakthrough times they report; using the details of the experimental setup, we calculated new breakthrough capacities which are reported in Table 9. In an inert medium, H<sub>2</sub>S reacts chemically with metal oxides, and hence, at most the adsorbed amount can correspond to 100% utilization of the metal oxide on the high-surface-area substrates. However, these two studies show H<sub>2</sub>S adsorption far exceeding the theoretical maximum, suggesting that Claus reaction occurs between H<sub>2</sub>S and O<sub>2</sub> from the air in the feed and the metal oxide functions as catalyst for this reaction rather than itself reacting with H<sub>2</sub>S to form metal sulfide.

Dhage et al. studied room-temperature H<sub>2</sub>S adsorption on transition-metal-promoted ZnO, impregnated on high-surface-area ( $\sim 550 \text{ m}^2/\text{g}$ ) SiO<sub>2</sub>.<sup>277</sup> The ZnO/SiO<sub>2</sub> system showed much higher absolute breakthrough capacities as well as percentage Zn utilization compared to their unsupported commercial counterparts from BASF and Sud-Chemie (see Table 9). It was observed that the sulfur capacity oscillated, reproducibly, with the number of cycles rather than monotonically increasing or decreasing. Using dopants such as Mn, Fe, Co, Ni, and Cu improved the utilization of ZnO, with the effect from copper being most prominent, changing the ZnO utilization at saturation from an already high 64% to about 93%. This increase does not seem to improve with the amount of copper, since the saturation capacities remained nearly unchanged upon increasing the Cu:Zn ratio from 0.05 to 0.25 at the same overall metal oxide loading. DFT studies showed that there is a significant energetic discrimination between H<sub>2</sub>S binding to a Cu<sup>2+</sup> versus a Zn<sup>2+</sup> site; this difference is smaller for H<sub>2</sub>O.<sup>278</sup> On a ZnO surface with some Zn<sup>2+</sup> sites substituted with Cu<sup>2+</sup>, there can be a displacement of H<sub>2</sub>O with H<sub>2</sub>S at the Cu<sup>2+</sup> surface sites. This is yet another explanation for the promoter effect by copper, in addition to several other arguments such as surface area and diffusion invoked earlier. Yang and Tatarchuk<sup>279</sup> also carried out similar studies and found significantly enhanced utilization by doping ZnO with copper or silver. In another study, they studied Fe- and Mn-promoted H<sub>2</sub>S sorbents supported on silica and found higher metal utilization compared to undoped ZnO; however, no significant preference was observed for Fe or Mn.<sup>280</sup> For the first time, real-time *in situ* electron spin resonance (ESR) spectroscopy was performed during reactive adsorption of H<sub>2</sub>S. It was inferred that the surface of the sorbents is enriched with Fe promoter cations, while the Mn<sup>3+</sup> promoter cations are located within the supported ZnO nanocrystallites. *In situ* experiments over multiple cycles may help to further elucidate the mechanism behind the oscillatory behavior.

Hussain et al. investigated the effect of different supports for ZnO; SBA-15 allows much higher breakthrough capacities as well as ZnO utilization.<sup>281</sup> This further highlights the importance of designing increasingly improved supports for metal oxides and suggests that Cu-Zn mixed oxides doped on SBA-15 may demonstrate a high capacity. In addition to capacity, stable performance of the adsorbent over several regeneration cycles is an important factor that may impact the economic viability of the process; in general, it is hard to reproducibly achieve the capacity of fresh adsorbents.<sup>284–286</sup> Generally, nanoparticles exhibit a tendency to grow into larger crystallites during the process of high-temperature regeneration. Inspired by the work of Prieto et al., who developed a highly stable methanol synthesis catalyst of Cu-ZnO nanoparticles on SBA-15,<sup>288</sup> Elyassi et al. investigated this adsorbent for H<sub>2</sub>S removal, resulting in extremely high and fully regenerable breakthrough capacities and ZnO utilization over five regeneration cycles.<sup>282</sup>

The major drawback of such composite sorbents is that the active component forms only a small fraction of the overall mass of the material, so even though high metal oxide utilizations can be achieved, the absolute amount of H<sub>2</sub>S that can be removed per unit mass of the adsorbent remains low. Attempts to increase the loading of metal oxide have not succeeded in increasing the H<sub>2</sub>S capacity without loss in % utilization.<sup>283,284,287</sup> Future research to increase the fraction of the active material in the composite with high utilization of the active component and high regenerability of the sorbents will help develop even better materials.

**3.6.2. Supported Amines.** Supported amine adsorbents can be broadly classified into three classes: Class 1 constitutes adsorbents with physically loaded amine species, Class 2 adsorbents contain a covalent link between the amine and the solid support, mostly via silane chemistry or via polymeric supports with amine-containing side chains, and Class 3

adsorbents comprise porous supports upon which amino-polymers are polymerized *in situ*, starting from an amine-containing monomer.<sup>289</sup> Class 3 materials combine the higher amine loadings of class 1 materials and the enhanced stability of class 2 materials due to amine–support covalent linkages.<sup>290,291</sup>

Huang et al. first reported on H<sub>2</sub>S removal using supported amines by employing high-surface-area silica supports (silica xerogel (816 m<sup>2</sup>/g) and MCM-48 (1389 m<sup>2</sup>/g)) functionalized with 3-aminopropyl (−CH<sub>2</sub>CH<sub>2</sub>CH<sub>2</sub>NH<sub>2</sub>) groups.<sup>292</sup> Adsorption/desorption was measured for pure-component H<sub>2</sub>S, CO<sub>2</sub>, and CH<sub>4</sub>, with and without moisture. At atmospheric pressure and temperature, the CO<sub>2</sub>/amino group ratio was observed to be 0.7 and 0.9 for xerogel and MCM-48, respectively. These ratios are 0.08 and 0.05 for CH<sub>4</sub> and 0.29 and 0.25 for H<sub>2</sub>S at the highest measurement pressure of 0.001 atm (1000 ppmv) for xerogel and MCM-48, respectively. The sorbents could be almost completely regenerated by pressure swing or temperature swing at 75 °C. The results indicated that the presence of water vapor doubled the amount of CO<sub>2</sub> adsorbed and barely affected the H<sub>2</sub>S adsorption.

Zhou et al. explored Class 1 adsorbents by physically loading triethanolamine (C<sub>6</sub>H<sub>15</sub>O<sub>3</sub>N; TEA) on silica gel (335 m<sup>2</sup>/g).<sup>293</sup> Due to the weaker basicity of TEA, its sorption capacity is nearly 100 times less than that of amine-modified silicas.<sup>292</sup> The breakthrough capacity doubled on loading the silica gel with 20 wt% of TEA and increased 5-fold when the loading was increased to a mere 27.5 wt%. There is no clear explanation for this sudden rise in adsorption, except that small selective pores that are otherwise unexposed to TEA may get filled with TEA at a higher loading of 27.5 wt%. In a subsequent study, the authors used this system for studying a multi-cycle pressure swing adsorption setup.<sup>294</sup> In a follow-up work, the authors synthesized SBA-15 as a high specific surface area TEA carrier and reported that the amount of H<sub>2</sub>S adsorbed on the TEA-modified SBA-15 is 1.85 times more than that on the TEA-modified silica gel.<sup>295</sup> Xue and Liu tried another tertiary amine, methyl-diethyl-amine, loaded on SBA-15, and found an optimal amine loading of 60 wt% for an H<sub>2</sub>S breakthrough capacity of 0.1 mmol/g.<sup>296</sup> Although the adsorbed amine is stated to be methyldiethylamine, such low loadings, comparable to those for TEA, are more representative of methyltriethanolamine.

In another study, physically loaded polyethylenimine (PEI) particles on mesoporous molecular sieves MCM-41 at 50 wt% loading were explored for low-temperature H<sub>2</sub>S adsorption at 90 °C and 10 ppmv inlet concentration.<sup>297</sup> The adsorbent could maintain an outlet concentration of 0.04 ppmv. The utility of these sorbents for natural gas sweetening at higher H<sub>2</sub>S concentrations needs to be investigated. In yet another study, linear PEI was dispersed inside the meso-channels of a SBA-15 framework, allowing interaction of amine groups in PEI with silanol groups on SBA-15.<sup>298</sup> The breakthrough and saturation capacities increased with inlet H<sub>2</sub>S concentrations of 2000, 4000, and 6000 ppmv in the ranges 0.68, 1.18, 1.48 and 1.50, 2.06, 2.38 mmol/g, respectively. The saturation value for amine-grafted sorbents at 1000 ppmv is 0.56 mmol/g.<sup>292</sup> So unlike TEA, PEI-modified supports show higher affinity for H<sub>2</sub>S, probably due to higher basicity of PEI, but possibly due to higher swelling of PEI compared to TEA. This is an open question that can be addressed perhaps by molecular simulations. The presence of moisture proved to enhance the adsorption capacity since only one amine group is needed per H<sub>2</sub>S molecule in the presence of moisture, versus two in its absence. However, moisture also resulted in a decrease in H<sub>2</sub>S

desorption rates. The same authors also studied the effects of the operating temperature (22–75 °C), gas hourly space velocity (GHSV; 337–1011 h<sup>-1</sup>), amount of PEI loading, and different molecular sieve supports (MCM-41, MCM-48, and SBA-15).<sup>299</sup> The structure of the mesoporous molecular sieves influences the kinetic capacity of the supported PEI sorbents; large pore size and three-dimensional channel structure favor higher breakthrough capacity. A decrease in temperature favors both breakthrough and saturation capacities, while a decrease in GHSV enhances the breakthrough capacity. The amount of PEI loading has a strong synergistic influence on the sorption performance: 50 wt% PEI on SBA-15 gives the best breakthrough capacity, while 65 wt% PEI on SBA-15 shows the highest saturation capacity. The developed sorbents exhibit a breakthrough capacity as high as 0.79 mmol/g and a saturation capacity of 3.02 mmol/g at 22 °C using 4000 ppm H<sub>2</sub>S, 20% H<sub>2</sub> in bulk N<sub>2</sub>. In addition, the developed sorbents can be regenerated easily at mild conditions (75–100 °C), with sorption capacity maintained over eight cycles.

The studies discussed so far did not involve H<sub>2</sub>S adsorption in the presence of CO<sub>2</sub>, which is known to be much more acidic compared to H<sub>2</sub>S. Ma et al. have made significant progress by finding an exceptional dependence of these sorbents on temperature for CO<sub>2</sub> and H<sub>2</sub>S competitive sorption and developing an innovative sorption process.<sup>300</sup> These PEI/SBA-15 sorbents show an exceptionally high CO<sub>2</sub> loading at 75 °C (3.2 mmol/g at 0.15 atm), but the lower kinetic barrier for H<sub>2</sub>S compared to CO<sub>2</sub>, which may be attributed to the faster proton-transfer reaction mechanism in the case of H<sub>2</sub>S, results in higher H<sub>2</sub>S breakthrough capacities at a lower temperature of 22 °C. The authors proposed a two-stage process, with the first column being operated at 75 °C for CO<sub>2</sub> removal and the second column at 22 °C for H<sub>2</sub>S removal (see Figure 13).

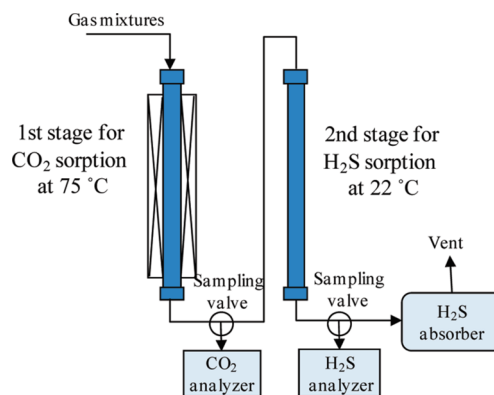


**Figure 13.** Scheme of the experimental two-stage process for removal of CO<sub>2</sub> and H<sub>2</sub>S from a model fuel gas. Reprinted with permission from ref 300. Copyright 2009 American Chemical Society.

Yosuk and co-workers carried out similar two-stage studies for PEI loaded on low-cost fumed silica (fSi) and also investigated regeneration studies over multiple cycles.<sup>301</sup> Although the authors observed high breakthrough capacities for both CO<sub>2</sub> and H<sub>2</sub>S for pure-component adsorption at 80 and 30 °C, respectively, in the mixture adsorption with two-column configuration, the working capacity of CO<sub>2</sub> was enhanced from 2.2 to about 3.5 mmol/g, while that of H<sub>2</sub>S decreased from the expected 1.2 to about 0.05 mmol/g. This reduced performance for H<sub>2</sub>S compared to the system introduced by Ma et al. can be attributed to two factors: (i) the difference in

$\text{CO}_2$  and  $\text{H}_2\text{S}$  pure-component adsorption at 22 °C for PEI/SBI-15 is much higher compared to the difference at 30 °C for PEI/fSi, and (ii) the mixture feed contained a very high concentration of  $\text{CO}_2$  (20%) compared to  $\text{H}_2\text{S}$  (0.36%) in the work of Yoosuk et al.; these values were 2.4% and 0.40%, respectively, for the work of Ma et al. These differences demonstrate the importance of choice of process conditions in selecting optimal sorbents. Similar to the discovery of novel zeolites for natural gas purification through a combined material screening and process optimization approach,<sup>302</sup> process optimization in materials selection for supported amines can help discover optimal sorbents.

In spite of these exciting properties, the powder nature of ordered mesoporous silica inhibits its direct usage in industrial packed columns due to very high pressure drops. Chen et al. investigated hierarchical porous silica supports for PEI. They can be easily formed as monoliths, which can be directly used in the fixed bed without any shaping process.<sup>303</sup> The largest breakthrough capacity of these sorbents was 1.27 mmol/g, about 60% higher than that of PEI/SBA-15 (0.79 mmol/g) or MCM-41 (0.81 mmol/g), although the test for the former was carried out at a lower inlet  $\text{H}_2\text{S}$  concentration and a higher GHSV.<sup>299</sup> A new parameter, polymerization degrees of PEI (423, 600, 15 000, 750 000), was investigated, and it was found that the sorbent with a PEI molecular weight of 600 had the best sorption property. The authors propose that PEI with higher polymerization degree should have very large steric hindrance and low fluidity, restraining the internal diffusion of  $\text{H}_2\text{S}$  and lowering the amine utilization, while PEI (423), a mixture of linear monomers and branch polymers, may be partially consumed or volatilized during the impregnation and drying, resulting in the decrease of efficient amine groups.

Belmabkhout et al. studied triamine-grafted ( $-\text{CH}_2\text{CH}_2\text{CH}_2\text{NHCH}_2\text{CH}_2\text{NHCH}_2\text{CH}_2\text{NH}_2$ ) pore-expanded mesoporous silica (TRI-PE-MCM-41) for adsorption of dry  $\text{CO}_2$ ,  $\text{H}_2\text{S}$ , and  $\text{CH}_4$  and found a much higher affinity for  $\text{CO}_2$  and  $\text{H}_2\text{S}$  compared to  $\text{CH}_4$  (see Figure 14).<sup>304</sup> Binary  $S_{\text{H}_2\text{S}/\text{CO}_2}$  varied from 70 to 10 upon varying the  $\text{H}_2\text{S}$  concentrations from 5 to 100 ppm.<sup>305</sup> These materials thus provide a promising solution to single-step  $\text{H}_2\text{S}$  and  $\text{CO}_2$  removal. Such simultaneous removal is desirable if re-injection of concentrated

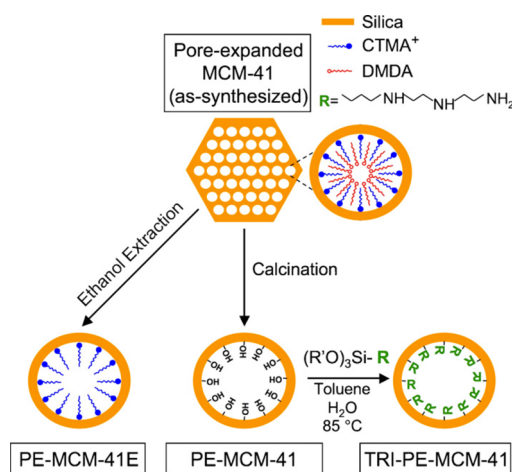


**Figure 14.** Schematic representation of the synthesis of amine-functionalized mesoporous silica. Reprinted with permission from ref 306. Copyright 2010 Elsevier.

sour gas stream into empty gas fields is preferred over conversion of  $\text{H}_2\text{S}$  to elemental sulfur by the Claus process.  $\text{H}_2\text{S}$  adsorption isotherms in the temperature range of 25–80 °C are available from two different studies, and both predict an isosteric heat of adsorption between –40 and –20 kJ/mol with increasing loading; the low-loading heats of adsorption can be as high as –100 kJ/mol.<sup>305,306</sup>

Another Class 1 adsorbent study employed SBA-15 loaded with hexamethylenetetraamine for  $\text{H}_2\text{S}$  removal from a stream containing 9000 ppm  $\text{H}_2\text{S}$  in  $\text{CH}_4$ ; the highest loading was observed for 50 wt% amine loading with a capacity of 0.75 mmol/g, stable over 10 cycles when overnight regeneration was conducted using  $\text{N}_2$  at 100 °C.<sup>307</sup> In general, all sorbents in this category can be fully regenerated under mild temperature conditions and are shown to maintain a constant capacity for several cycles in most of the studies. Efforts toward reducing the regeneration time will increase the productivity of these sorbents.

**3.6.3. Zeolite/Polymer.** Bhandari et al. developed hollow fibers with polymer “binder”, impregnated with high loadings of sulfur-selective zeolite sorbent “fillers” (see Figure 15).<sup>308</sup>

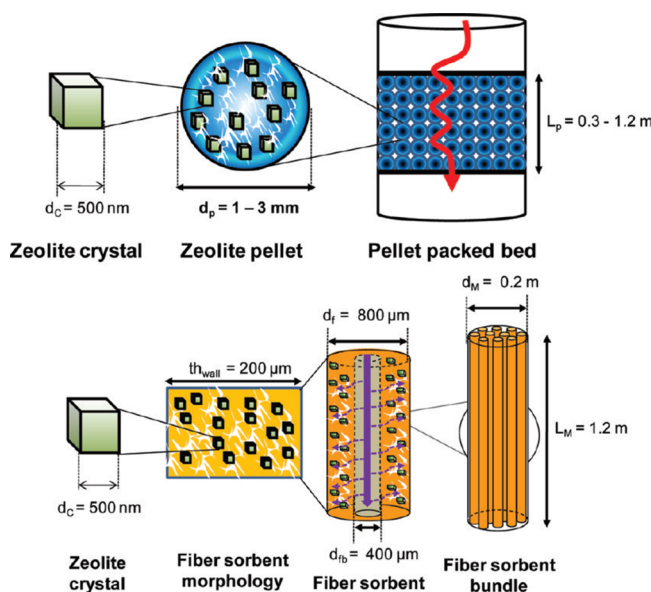


**Figure 15.** Typical dimensions and mode of creation in a pellet packed bed vs fiber sorbent module. Reprinted with permission from ref 308. Copyright 2010 American Chemical Society.

Cellulose acetate formed the binder and zeolite NaY formed the filler for these hollow fibers with high sorbent loadings and good strength. Although the hollow fiber morphology is representative of contact in a membrane process, it should be noted that the fibers here are used as adsorbents. The fiber-sorbent morphology was characterized using equilibrium sorption, gas permeation, SEM, and EDX. These sorbents were shown to be very effective for low-concentration (30 ppm)  $\text{H}_2\text{S}$  removal, especially when compared to a packed-bed process, and were found to be fully regenerable by application of heat (120 °C under  $\text{N}_2$ ).

**3.6.4. Metal–Organic Framework/Graphite Oxide.** It was envisioned that the GO and MOF composites would increase the dispersive forces in a highly porous MOF structure via dense nanoporous GO layers (5–46 wt%).<sup>186</sup> Petit and co-workers studied GO composites with HKUST-1 and found a

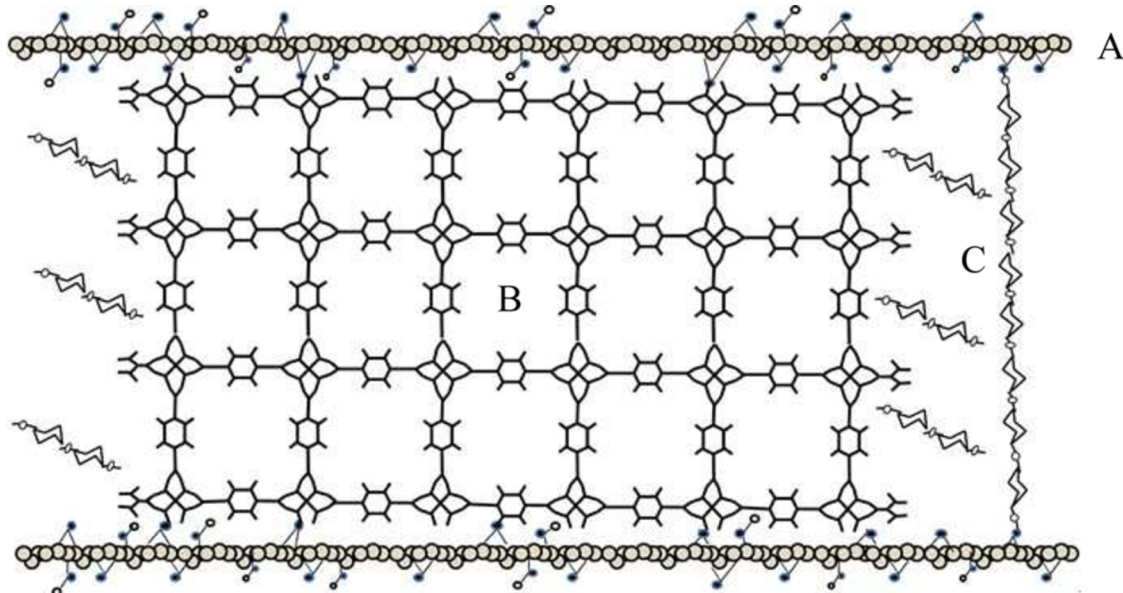


**Figure 16.** Schematic view of the glucose-promoted MOF-5/GO structure unit: (A) GO layer, (B) MOF-5, and (C) glucose polymer. Reprinted with permission from ref 310. Copyright 2012 American Chemical Society.

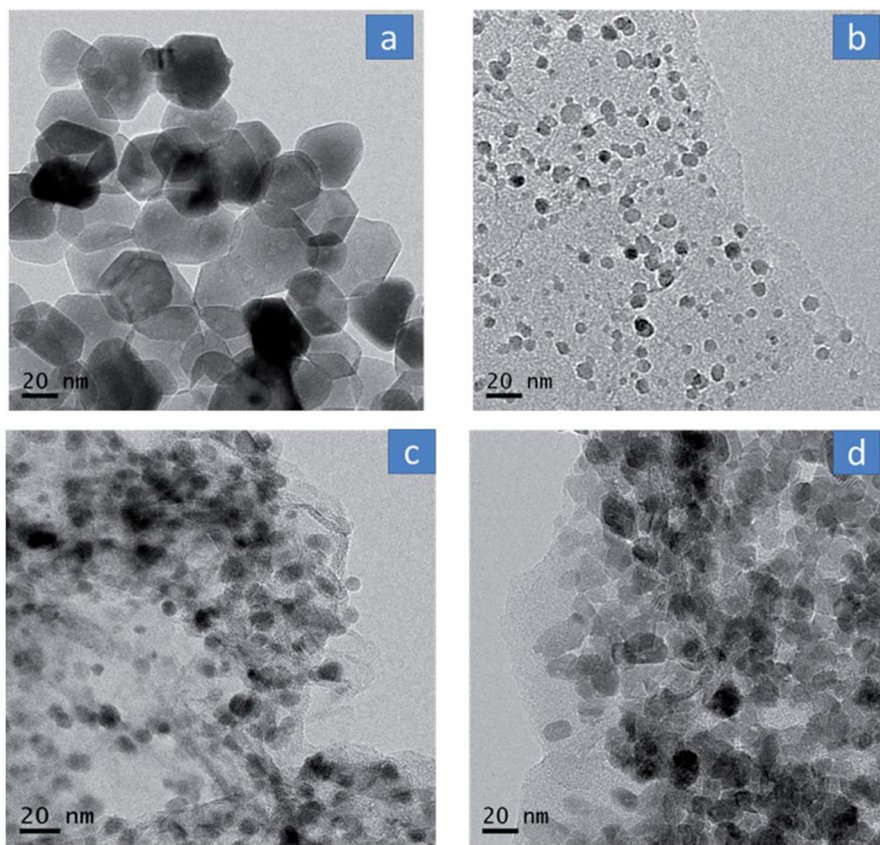


**Figure 17.** TEM images of (a) pristine ZnO nanoparticles, (b) TRGZ-1 (10 wt% ZnO), (c) TRGZ-2 (30 wt% ZnO), and (d) TRGZ-3 (50 wt% ZnO) graphene/ZnO nanohybrids synthesized by an *in situ* thermo-annealing method. Reproduced with permission from ref 311. Copyright 2016 The Royal Society of Chemistry.

synergistic effect on sorption capacity (9 mg/g for GO, 92 mg/g for HKUST-1, and 199 mg/g for composite with 5 wt% GO). The breakthrough capacities measured at room temperature using 1000 ppm H<sub>2</sub>S in moist air were not found to correlate with the measured porosity of the composites, suggesting a mechanism in addition to physisorption contributing to the

overall sorption. Indeed the adsorbent bed changed color from light blue (hydrated copper) to black (CuS). Ebrahim et al. found that adsorption capacities increased by 85% for composites with sulfur-doped graphite due to the presence of moisture compared to dry conditions.<sup>309</sup> Those authors suggested that, under moist conditions, water acts as a

“screening” factor, blocking the direct attack of  $\text{H}_2\text{S}/\text{SO}_2$  on the copper centers and preserving the structure to some degree. They found that the catalytic effect of the modified graphene phase results in the formation of  $\text{SO}_2$  with a much higher  $\text{H}_2\text{S}$  breakthrough capacity of  $241 \pm 6 \text{ mg/g}$ .

In another study, Huang et al. prepared composites using MOF-5 and GO in the presence of glucose.<sup>310</sup> GO enhanced the dispersive forces in MOF-5, as demonstrated by higher  $\text{H}_2\text{S}$  uptake, but beyond the optimal loading of 5.25%, GO led to collapse of the MOF crystal structure. At 5.25% GO loading, composites with and without glucose have surface areas of 1062 and  $295 \text{ m}^2/\text{g}$ , respectively; the respective breakthrough capacities of these materials using 100 ppm  $\text{H}_2\text{S}$  in  $\text{N}_2$  are 130.1 and 31.9 mg/g. The authors suggest that glucose can restrain the distortion of the composite material due to polymerization of glucose under hydrothermal conditions; these short polymers fill in the structure to support the framework, and some may even react with the functional groups on the GO (see Figure 16). While this approach provides a route to stabilize such composite materials, performance and structural reversibility of these sorbents on regeneration need to be investigated.

**3.6.5. Metal (Hydr)oxide/Graphite Oxide.** Several studies report on the Claus reaction between  $\text{H}_2\text{S}$  and air on composites of metal (hydr)oxide and GO,<sup>312–323</sup> with breakthrough  $\text{H}_2\text{S}$  capacities as high as 150 mg/g of adsorbent at 1000 ppm  $\text{H}_2\text{S}$  in air. Lonkar et al. demonstrated an easy *in situ* fabrication of nanostructured graphene/CuO<sup>324</sup> and graphene/ZnO<sup>311</sup> composites without the use of any solvents, toxic-reducing agents, or organic modifiers. The metal oxide particles in the presence of graphene had a size of sub-20 nm, compared to metal oxide particles of  $\sim 50$  nm synthesized by the same method (see Figure 17). At ambient temperature and with a feed composition of 0.15%  $\text{H}_2\text{S}$ , 0.41%  $\text{CO}_2$ , and 99.4%  $\text{CH}_4$ , a 50 wt% composite material led to over twice the capacity of pristine ZnO (see Table 10). Regeneration of these high-capacity materials with the advantage of easy synthesis is an important aspect that should be considered in the future.

**Table 10.  $\text{H}_2\text{S}$  Breakthrough Capacities of ZnO/GO Composites<sup>311</sup>**

wt% GO	$S_{\text{BET}}$ ( $\text{m}^2/\text{g}$ )	mg S/g
0	12.4	52.2
50	119	111
70	208	85.8
90	257	33.9
100	223	2.9

**3.6.6. Metal Oxide/Activated Carbon.** Fauteux-Lefebvre et al. embedded iron nanoparticles in carbon nanofilaments and tested these for  $\text{H}_2\text{S}$  removal under a wide range of operating conditions.<sup>325</sup> Fe K-edge spectra showed that iron was in its oxidized states ( $\text{Fe}_2\text{O}_3$  and  $\text{Fe}_3\text{O}_4$ ). Even at higher temperature of 300 °C, low breakthrough capacities were observed. Higher metal loadings of 28 wt% could not improve the  $\text{H}_2\text{S}$  uptake (see Table 11). Zhang and co-workers studied various loadings of MnO<sub>2</sub> on AC under a wide range of synthesis and operating conditions and observed capacities as high as 110 mg/g for a 50 wt% MnO<sub>2</sub> loading at only 20 ppm  $\text{H}_2\text{S}$ .<sup>326</sup> In another study, sorbents were prepared by finely dispersing mixed ZnO and CuO onto a commercial AC at fixed total metal loading (10 wt %) and Cu:Zn atomic ratios ranging from 0:1 to 1:1.<sup>327</sup> The

**Table 11.  $\text{H}_2\text{S}$  Breakthrough Capacities in Metal Oxide/Activated Carbon**

adsorbent	$S_{\text{BET}}$ ( $\text{m}^2/\text{g}$ )	mg S/g	T (°C)	composition	reference
18Fe-CNF	139	8	100	500 ppm $\text{H}_2\text{S}$ in He	Fauteux-Lefebvre et al. <sup>325</sup>
		22	300		
28Fe-CNF	145	8	100		
AC	580	14	40	20 ppm $\text{H}_2\text{S}$ in $\text{N}_2$	Zhang et al. <sup>326</sup>
50MnO <sub>2</sub> -AC	391	110			
AC	641	4.6	30	3000 ppm $\text{H}_2\text{S}$ in $\text{N}_2$	Balsamo et al. <sup>327</sup>
Cu <sub>0.7</sub> Zn <sub>1.0</sub> /AC	558	34			
Cu <sub>0.05</sub> Zn <sub>0.95</sub> /AC	520	37			
Cu <sub>0.1</sub> Zn <sub>0.9</sub> /AC	549	40			
Cu <sub>0.25</sub> Zn <sub>0.75</sub> /AC	555	40			
Cu <sub>0.5</sub> Zn <sub>0.5</sub> /AC	570	47			

surface area was hardly affected due to the high dispersion of the metal oxides; moderately high  $\text{H}_2\text{S}$  capacities could be achieved. Only 18–27% of the capacity could be regenerated at 400 °C, and even at a temperature of 620 °C, only 40–46% of the capacity could be regenerated.

Complete regeneration and reusability of an adsorbent may or may not be feasible; therefore, it is important to consider the eventual disposal of spent adsorbents. This becomes particularly important for  $\text{H}_2\text{S}$ -removal applications, since contact of an improperly disposed adsorbent with air or water may result in a concentrated release into the environment and can have very serious health implications. Some of the spent metal oxides, such as iron sulfide, can be pyrophoric and can release acid gases into the atmosphere. Dissolution of these gases in water bodies can have unacceptable effects on the ecosystem. Some of the methods for treating spent adsorbents include regeneration followed by inert purge, flooding with liquid water, and steam purging.<sup>328</sup> The cost of an adequate spent-adsorbent treatment method may have large bearings on this additional cost.

#### 4. MEMBRANE SEPARATION

As natural gas consumption is expected to nearly double in the coming 25 years and the raw natural gas has a varying composition depending on its origin, there is an opportunity for membrane technology to remove impurities including water, carbon dioxide, nitrogen, hydrogen sulfides, and other hydrocarbons.<sup>329</sup> Bhide and Stern investigated the relative economics of cellulose acetate (CA) membrane technology and gas absorption using DEA and found that the membrane process for  $\text{CO}_2$  removal is more economical to meet the 2% specification over the entire range of  $\text{CO}_2$  feed concentrations (>5%).<sup>330</sup> Presence of  $\text{H}_2\text{S}$  in the feed stream resulted in an increased separation cost for meeting the specifications of both  $\text{H}_2\text{S}$  and  $\text{CO}_2$  (4 ppm and 2%, respectively). Unlike the superior performance of membranes over the entire range of acid gas concentration for  $\text{CO}_2$  alone, the presence of  $\text{H}_2\text{S}$  allowed membranes to be economical only at higher total acid gas ( $\text{H}_2\text{S} + \text{CO}_2$ ) concentrations. While this analysis was carried out for CA membranes with  $S_{\text{CO}_2/\text{CH}_4} = 21$  and  $S_{\text{H}_2\text{S}/\text{CH}_4} = 50$ ,<sup>330</sup> it should be noted that the  $S_{\text{H}_2\text{S}/\text{CH}_4}$  values for such membranes range between only 15 and 30. Membranes with higher selectivities and permeabilities than the CA membranes employed in this economic analysis may significantly expand

**Table 12.** H<sub>2</sub>S Permeability and Permselectivity in Polymeric Membranes

polymer <sup>a</sup>	$P_{\text{H}_2\text{S}}$ (mol/(m <sup>2</sup> ·s·Pa))	$S_{\text{H}_2\text{S}/\text{CH}_4}$	$S_{\text{H}_2\text{S}/\text{CO}_2}$	T (°C)	p (bar)	CH <sub>4</sub> :CO <sub>2</sub> :H <sub>2</sub> S	reference
Nylon-6 (polyamide)	$3.0 \times 10^{-9}$			30	0.94	pure	Heilman et al. <sup>339</sup>
rubber hydrochloride	$5.3 \times 10^{-9}$			30	0.99		
PVB	$3.6 \times 10^{-7}$			30	0.85		
poly(vinyl trifluoroacetate)	$1.4 \times 10^{-8}$			30	1.0		
polyethylene	$5.8 \times 10^{-7}$			30	0.97		
PET	$6.1 \times 10^{-10}$			0	0.95		
	$7.3 \times 10^{-9}$			60	1.0		
PVDC	$1.4 \times 10^{-9}$			30	0.93		
PDMS + PEG + PSf	$2.6 \times 10^{-8}$	140	5.7	25	4.4	pure	Kulprathipanja et al. <sup>340</sup>
PDMS + PEG + PSf (glycerol)	$3.6 \times 10^{-8}$	162	8.1				
PDMS (Cl <sub>3</sub> C—CF <sub>3</sub> ) + PEG + PSf	(1.2–3.1) × 10 <sup>-8</sup>	115–185	5.4–5.9			pure	Kulprathipanja et al. <sup>341</sup>
PDMS + PSf	$4.7 \times 10^{-8}$	9.9	2.3				
CA		15–20		40	14.6	pure	Schell et al. <sup>332</sup>
PDMS	$2.9 \times 10^{-10}$	6.5	1.8	35	1.1	pure	Stern et al. <sup>342</sup>
Pebax 4011 + PSf		139–190	7.7–9.5	20	4.5	pure	Blume et al. <sup>343</sup>
Pebax 4011 + PVDF		51 41 52 48 50 48		23	28 68 68 68 68 68	99.9:0:0.097 95.79:4.12:0.087 94.9:4.12:0.986 87.34:10.8:1.83 91.77:8.14:0.095	Lokhandwala et al. <sup>344</sup>
poly(ether urethane) [PPG]	$1.1 \times 10^{-9}$	21	3.0	35	10.1	70.8:27.9:1.3	Chatterjee et al. <sup>333</sup>
poly(ether urethane) [PEG]	$1.2 \times 10^{-9}$	58	4.5			70.8:27.9:1.3	
poly(ether urethane urea) [PPG]	$2.7 \times 10^{-9}$	19	3.1			70.8:27.9:1.3	
poly(ether urethane urea) [PEG]	$8.8 \times 10^{-10}$	74	4.4			70.8:27.9:1.3	
Pebax MX 1074	$2 \times 10^{-9}$	54	4.5			70.8:27.9:1.3	
CA	$9.4 \times 10^{-12}$	19	0.9			65.29:6	
poly(ether urethane urea) [PEG]	$4.5 \times 10^{-10}$	102	4.6	20		70.8:27.9:1.3	
PVBTAF	$9.3 \times 10^{-9}$ $4.3 \times 10^{-9}$ $5.4 \times 10^{-9}$ $2.8 \times 10^{-9}$	7000 950 3300 2100		30	1.2 5.0 1.1 8.5	89.5:0:10.5 79.7:10:10.3	Quinn et al. <sup>345</sup>
PVBTAF-4CsF	$3.06 \times 10^{-8}$ $1.41 \times 10^{-8}$	n.d. n.d.	10 4.7		1.1 4.4	80.1:10:9.9	Quinn et al. <sup>346</sup>
PC/siloxane	$4.85 \times 10^{-11}$	10	2.8	20 ± 2		pure	Amirkhanov et al. <sup>347</sup>
poly(4-methyl pentene)	$3.35 \times 10^{-13}$	7.6	1.2				
PDMS				1.7	35	10.1	Wilks et al. <sup>348</sup>
Pebax 2533				2.1			
substituted-PPZ ( $T_g = 55$ °C)	$6 \times 10^{-11}$	4	0.74	30	2.1	pure	Orme et al. <sup>349</sup>
substituted-PPZ ( $T_g = 4$ °C)	$1 \times 10^{-10}$	27	4.1			3:3:3	Orme et al. <sup>350</sup>
substituted-PPZ ( $T_g = -63$ °C)	$3 \times 10^{-9}$	60	5.0				
substituted-PPZ ( $T_g = 4$ °C)	$4 \times 10^{-11}$	28	1.9				
substituted-PPZ ( $T_g = -63$ °C)	$3 \times 10^{-9}$	79	4.4				
PTMSP	$7.1 \times 10^{-8}$		1.2	23		0:10.5:1.5	Merkel et al. <sup>351</sup>
PDMS	$1.1 \times 10^{-8}$		1.5	21		0:11.7:0.7	
Pebax 1657			3.7				

Table 12. continued

polymer <sup>a</sup>	$P_{\text{H}_2\text{S}}$ (mol/(m <sup>2</sup> ·s·Pa))	$S_{\text{H}_2\text{S}/\text{CH}_4}$	$S_{\text{H}_2\text{S}/\text{CO}_2}$	T (°C)	p (bar)	CH <sub>4</sub> :CO <sub>2</sub> :H <sub>2</sub> S	reference
PC	$6.3 \times 10^{-12}$		0.23				
PSf	$1.1 \times 10^{-11}$		0.26				
Cytop	$3.8 \times 10^{-12}$		0.037			0:0:15	
TFE/PMVE/8CNVE			0.13	37		0:10.5:1.5	
Teflon AF 1600			0.15	23			
polyamide + PSf (before annealing)	$1.7 \times 10^{-8}$	40.5	3.16	30	10	pure	Sridhar et al. <sup>352</sup>
polyamide + PSf (after annealing)	$1.7 \times 10^{-8}$	49.1	3.41				
poly(ester urethane urea) + Teflon	$4.4 \times 10^{-8}$	43	3.79	35	10	91.6:5.4:3	Mohammadi et al. <sup>353</sup>
	$3.0 \times 10^{-8}$	27	2.72		30	91.6:5.4:3	
	$8.2 \times 10^{-8}$	43	3.91	55	10	91.6:5.4:3	
	$2.9 \times 10^{-8}$	12	1.90		30	91.6:5.4:3	
butadiene-sulfone	$5.7 \times 10^{-9}$	3.8		35	5	96.1:0:3.9	Saeidi et al. <sup>354</sup>
	$8.4 \times 10^{-9}$	8.1			15		
Cardo-type PIM	$7.3 \times 10^{-9}$	3.8		23	4.5	99.96:0:0.04	Chenar et al. <sup>355</sup>
	$9.4 \times 10^{-9}$	6.1			7.9		
PPO	$2.6 \times 10^{-8}$	3.1		23	4.5		
	$2.5 \times 10^{-9}$	4.1			7.9		
6F-PAI-1		12 ± 1	0.35	35	43	70:20:10	Vaughn et al. <sup>356</sup>
6F-PAI-2		6.9 ± 0.5	0.49			60:20:20	
6F-PAI-1		8.1	0.19		4.5	pure	
6F-PAI-2		10.3	0.21				
CA	$3.8 \times 10^{-11}$	30	1.0	35	35	60:20:20	Achoundong et al. <sup>334</sup>
GCV-modified CA	$6.8 \times 10^{-10}$	34	1.6				
(6FDA-DAM) <sub>m</sub> (6FDA-DABA) <sub>n</sub>	$1.3 \times 10^{-10}$	12	0.35			70.15:19.9:9.95	Kraftschik et al. <sup>357</sup>
PEGMC [DEG]	$2.0 \times 10^{-10}$	19	0.59	35	35	60:20:20	Kraftschik et al. <sup>358</sup>
PEGMC [TEG]	$2.0 \times 10^{-10}$	21	0.64				
PEGMC [TetraEG]	$1.6 \times 10^{-10}$	20	0.59				
(6FDA-DAM) <sub>m</sub> (6FDA-DABA) <sub>n</sub>	$3.3 \times 10^{-10}$	25	0.83				
		9.0	0.30		4.5	pure	
6F-PAI-2		9	0.32	35	15	60:20:20	Vaughn et al. <sup>359</sup>
6F-PAI-1		12	0.27				
		22	0.40	35	15	50:45:5	
Pebax SA01 MV 3000 (commercial PAI)		42	4.2	35	15	60:20:20	
		42	3.8	35	15	50:45:5	
		43		35	2.4	pure	
PIM-6FDA-OH		7		35	4.5	pure	Yi et al. <sup>360</sup>
	$1.7 \times 10^{-10}$	13	0.28		7	70:15:15	
	$4.2 \times 10^{-10}$	30	1.2		48.3		
(6FDA-mPDA)-(6FDA-durene)		15	0.41	22	34.5	60:10:1	Yahaya et al. <sup>361</sup>
		23	0.84			60:10:20	
PDMS + PESf	$4.3 \times 10^{-9}$	4.0		35	30	98.32:0:1.68	Saedi et al. <sup>362</sup>
	$3.1 \times 10^{-9}$	3.2	0.66			97.5:2.1:0.4	

<sup>a</sup>Abbreviations: DABA, 3,5-diaminobenzoic acid; DAM, 2,4-diaminomethylene; DEG, diethylene glycol; GCV, grafting and cross-linking using vinyltrimethoxysilane; PAI, polyamide-imide; PC, polycarbonate; PEGMC, poly(ethylene glycol) monoesterified cross-linkable; PESf, poly(ether sulfone); PET, poly(terephthalic ester); PIM, polymer of intrinsic microporosity; PMVE, perfluoromethyl vinyl ether; PPO, poly(2,6-dimethyl-1,4-phenylene oxide); PTMSP, poly(1-trimethylsilyl-1-propyne); PVB, poly(vinyl butyral); PVDC, poly(vinylidene chloride); PVDF, poly(vinylidene fluoride); Pebax, poly(ether amide) block copolymers; TEG, triethylene glycol; TFE, tetrafluoroethylene; TetraEG, tetraethylene glycol; mPDA, 1,3-phenylenediamine; n.d., CH<sub>4</sub> not detectable; 4CsF, four cesium fluoride per repeat unit; 6FDA, 2,2'-bis(3,4-dicarboxyphenyl)hexafluoropropane

Table 12. continued

dianhydride (same as 4,4'-hexafluoroisopropylidene diphthalic anhydride); 6F-PAI, 6FDA-3-aminobenzoic acid-4,4'-hexafluoroisopropylidene dianiline; 8CNVE, perfluoro-8-cyano-5-methyl-3,6-dioxa-1-octene.

the regime for superior membrane performance over gas absorption. Additionally, hybrid processes involving membranes for bulk acid gas removal, followed by chemical absorption or adsorption in the polishing step, can drive the overall process toward better economics.

#### 4.1. Polymeric Membranes

Approximating solubility with the Henry's law and diffusivity with the Fick's law, and approximating the concentrations on the permeate side to be negligible compared to that on the feed side, the permselectivity of a polymer membrane,  $S_{ij}$ , in differentiating two species,  $i$  and  $j$ , can be expressed as

$$S_{ij} = \frac{P_i}{P_j} = \frac{F_i/p_i}{F_j/p_j} = \frac{D_i K_i}{D_j K_j} \quad (7)$$

where  $P_i$ ,  $F_i$ ,  $p_i$ ,  $D_i$ , and  $K_i$  are the permeability, flux, partial pressure, Fick's diffusion constant, and Henry's constant for species  $i$ . The ratio  $D_i/D_j$  can be viewed as the transport selectivity indicating the relative speed of the two components and is mainly governed by the molecular shapes and sizes. The ratio  $K_i/K_j$  can be viewed as the sorption selectivity and is governed by the relative gas solubilities in the membrane material.

The glass transition temperature,  $T_g$ , characterizes the range of temperatures over which a hard and relatively brittle "glassy" amorphous state of the polymer transitions into a soft and viscous "rubbery" state. Polymer chains are trapped in a frozen state at  $T < T_g$  but  $T > T_g$  allows for significant motion of the chains. Glassy polymers offer size-selective separation by virtue of differential diffusivity; in contrast, rubbery polymers suffer reduced size selectivity from increased elasticity of the polymer chains. The kinetic diameters of  $\text{H}_2\text{S}$  (3.6 Å) and  $\text{CO}_2$  (3.3 Å) are smaller than that of  $\text{CH}_4$  (3.8 Å); this suggests the possibility of a diffusion-based selectivity. The critical temperatures for these gases are 373, 304, and 191 K, respectively, suggesting that, compared to methane, the acid gases will interact more strongly with the polymer and also allow for sorption-based selectivity. Although both rubbery and glassy polymers can separate  $\text{CO}_2$  and  $\text{H}_2\text{S}$  from natural gas, in practice,  $\text{CO}_2$  is best separated by glassy polymer membranes (maximizing size selectivity), whereas  $\text{H}_2\text{S}$ , which is larger and more condensable than  $\text{CO}_2$ , is best separated by rubbery polymer membranes (maximizing sorption selectivity).<sup>331</sup> Although plants based on glassy CA membranes ( $T_g \approx 110^\circ\text{C}$ ) are widely used for  $\text{CO}_2$  removal from natural gas, these membranes also possess  $S_{\text{H}_2\text{S}/\text{CH}_4} \approx 15-30$ .<sup>332-334</sup> The contribution of diffusion and sorption to this overall selectivity is unclear;  $\text{H}_2\text{S}/\text{CH}_4$  sorption isotherms will help understand the relative proportions of the two factors. Using CA to reduce  $\text{H}_2\text{S}$  to pipeline specifications (4 ppm) results in vast over-processing as far as the  $\text{CO}_2$  concentrations are concerned. Thus, just like liquid absorbents with a higher  $\text{H}_2\text{S}/\text{CO}_2$  selectivity, there is a need for membranes with higher  $S_{\text{H}_2\text{S}/\text{CO}_2}$ .

Permselectivity can be obtained either from a real mixture experiment or by modeling mixture transport using pure-gas permeabilities and sorption isotherms. While it is most common to report the ideal selectivity (ratio of pure-gas permeabilities), it may be possible to adopt a more

sophisticated approach to include the effects of multi-component sorption and diffusion.<sup>335,336</sup> It is well known in the literature that the assumption of ideality grossly over-predicts selectivity for polymeric membranes if one of the species strongly absorbs/adsorbs onto the polymer. Absorption-induced swelling of the polymer increases chain mobility and gas flux, a phenomenon commonly known as membrane plasticization. Increased chain mobility lowers  $T_g$ , potentially transforming a membrane from glassy to rubbery and adversely affecting the size-selective term,  $D_i/D_j$ .  $\text{CO}_2$ -induced swelling of CA membranes results in a much lower  $\text{CO}_2/\text{CH}_4$  mixture selectivity compared to the ideal selectivity (35 vs 50 at 4 atm); the effect is more pronounced at higher  $\text{CO}_2$  partial pressures (32 vs 80 at 12 atm).<sup>337</sup> Other impurities, such as light hydrocarbons, water, very low concentration of aromatics, etc., can also have a plasticization effect on membrane permeances. In addition to plasticization, glassy materials suffer from physical aging where the polymer chains slowly relax into a preferred high-density form by a reduction in free volume.<sup>338</sup> This type of aging effect can reduce membrane permeabilities significantly over the average 2–5-year life of a membrane used in natural gas service.<sup>331</sup>

Kulprathipanja et al. synthesized two-component membranes comprising of a mixture of polydimethylsiloxane (PDMS) and poly(ethylene glycol) (PEG) plasticizers, having molecular weights between 200 and 600, cast upon a porous polysulfone (PSf) support that was pre-treated with glycerol.<sup>340,341</sup> Glycerol alters the pores of the support, thus increasing the permeability of hydrogen-bonding  $\text{H}_2\text{S}$  (see Table 12). These membranes are of the asymmetric type; a very thin, dense surface layer or skin is supported upon an integrally attached, much thicker supporting layer. In this case, the selective skin is rubbery, while the support is glassy. The authors reported very high  $\text{H}_2\text{S}/\text{CH}_4$  ideal selectivities between 115 and 185; however, the mixed gas selectivities measured later are smaller by a factor of 4–8.<sup>344,363</sup> Both PDMS and PEG belong to the class of rubbery membranes with  $T_g = -127$  and  $-67^\circ\text{C}$ , respectively; therefore, it is unlikely that plasticization results in lower mixture selectivities. It is possible, however, that these strongly absorbing membranes are being operated at both feed and permeate pressures in the saturated loading regime. Several studies report ideal and mixture  $\text{H}_2\text{S}/\text{CH}_4$  selectivities in PDMS membranes of  $\leq 11$ ,<sup>341,342,362</sup> indicating the crucial role of PEG plasticizers in enhancing the selectivity toward  $\text{H}_2\text{S}$ . Unlike CA and PDMS membranes, these two-component membranes present high  $S_{\text{H}_2\text{S}/\text{CO}_2}$  as well, possibly by benefitting from the hydrogen-bonding character of  $\text{H}_2\text{S}$ . However, this raises concerns about the influence of  $\text{H}_2\text{O}$  impurities on such membranes, and this can be additionally important considering that PEG is soluble in  $\text{H}_2\text{O}$ . Molecular simulations can possibly explain the role of PEG and also the influence of impurities on membrane performance.

Another class of polymer membranes, commercially known as the Pebax membranes, are composed of ether-amide block copolymers, where the polyether block imparts the flexible character to the rigid polyamide block. Various grades of Pebax membranes have been tested for acid gas removal, and these membranes yield ideal and mixture  $S_{\text{H}_2\text{S}/\text{CH}_4}$  values in the ranges

140–190 and 35–70, respectively.<sup>333,343,344,359</sup> Similar to PDMS and PEG, the Pebax membranes also belong to the class of rubbery membranes with  $T_g < -50$  °C; as mentioned earlier, the drop in mixture selectivity compared to ideal selectivity may be due to operation in the saturated loading regime. These membranes demonstrate  $S_{H_2S/CO_2}$  between 3.4 and 4.5. The presence of H<sub>2</sub>O impurities was examined by using a feed gas stream saturated with H<sub>2</sub>O vapor; no detrimental effect on the selectivities was observed, but the fluxes decreased by 40–45%.<sup>364</sup> Chatterjee et al. synthesized two poly(ether urethanes) and two poly(ether urethane ureas) using PEG or poly(propylene glycol) (PPG) for the ether block; the polyurethanes are structurally related to the Pebax polymers.<sup>333</sup> Membranes with PEG blocks yield much higher H<sub>2</sub>S/CH<sub>4</sub> and H<sub>2</sub>S/CO<sub>2</sub> selectivities compared to the ones with PPG blocks, but with no significant difference in the permeabilities; this maybe attributed to the higher mass fraction of polar hydroxyl groups in PEG compared to PPG. Very high selectivities reaching up to 100 for H<sub>2</sub>S/CH<sub>4</sub> and 4.8 for H<sub>2</sub>S/CO<sub>2</sub> were observed by reducing the temperature from 35 to 20 °C.

Yet another class of rubbery membranes that offer high selectivity for H<sub>2</sub>S/CH<sub>4</sub> and H<sub>2</sub>S/CO<sub>2</sub> separation (60–80 and 4–9, respectively) are substituted polyphosphazenes (PPZ), where the substituents are predominantly 2-(2-methoxyethoxy)ethanol (MEE) and 4-methoxyphenol.<sup>349,350</sup> Orme et al. explained that the flexible backbone of PPZ has a low rotational energy barrier due to pπ–dπ bonding between nitrogen and phosphorus. Polyether pendant groups, such as MEE, are linear chains of sp<sup>3</sup>-hybridized atoms which have many degrees of rotational freedom; thus, they do not significantly hinder the inherent flexibility of the backbone.<sup>350</sup> On the other hand, aromatic substituents hinder the backbone flexibility, in turn increasing  $T_g$ . This work showed a surprising result that lowering  $T_g$  resulted in increased permeabilities and separation factors at the same time. Similar ideal and mixture selectivities suggest that these rubbery membranes are operated in the regime where the polymer is not saturated with the more strongly absorbing gas molecules: the operating pressure is only 2.1 bar as opposed to several tens of atmospheres for previously mentioned mixture experiments. MEE is hydrophilic and makes the PPZ hydrophilic; at 100% MEE substitution, the resulting PPZ is soluble in water. In contrast, aromatic substituents impart hydrophobicity. The effect of moisture in the feed stream on the performance of PPZ membranes remains to be investigated. These 100–200 μm thick membranes were supported on ceramic supports with 0.2 μm pores. Permeation properties of thin membranes are very different from those of thick films, and since the selective layer of membranes in industrial use is usually only 0.1–1.0 μm thick,<sup>365</sup> performance for thinner substituted-PPZ membranes remains to be seen.

Quinn and co-workers have explored facilitated transport membranes for selective removal of H<sub>2</sub>S from natural gas mixtures.<sup>345,346</sup> These membranes are based on the poly-electrolyte, poly(vinylbenzyltrimethyl ammonium fluoride) (PVBTAf), and show exceptionally high mixture selectivity for selective removal of H<sub>2</sub>S and CO<sub>2</sub> from CH<sub>4</sub> (>800 and >400, respectively). Using NMR data, the authors show that CO<sub>2</sub> reacts with hydrated fluoride ions to form mobile bicarbonate ions, HCO<sub>3</sub><sup>−</sup>. The permeance of both CO<sub>2</sub> and H<sub>2</sub>S increased with decreasing feed partial pressure of the respective gases, a phenomenon observed for membranes

operated in the saturated loading regime; permselectivity data imply that both CO<sub>2</sub> and H<sub>2</sub>S compete for the same reaction sites, hydrated fluoride ions.<sup>345</sup> The authors also report that the membranes show no deterioration after 30 days of continuous operation but react irreversibly with trace levels of sulfur-containing contaminants, such as CS<sub>2</sub> and COS, that are common to cylinder H<sub>2</sub>S. The permselectivity of these membranes was increased by 3–4 times without reduction in selectivity by using fluoride-containing salts such as cesium fluoride.<sup>346</sup> The performance of these membranes is very sensitive to the relative humidity of the feed stream.

Unlike conventional microporous materials such as zeolites and activated carbon, polymeric materials possess advantageous properties, such as solution-processability and precise control over chemical functionality. However, polymeric membranes suffer from large inherent densities and, as a result, low permeabilities in general. Budd and co-workers developed a new class of polymeric membranes that not only are solution-processable but also possess intrinsic microporosity.<sup>366</sup> This new class of materials, known as polymers of intrinsic microporosity (PIMs), are a result of contorted shape and extreme rigidity of planar units fused together by rigid spirocyclic linkers. These kinks at the spiro-centers prevent efficient packing to form a dense polymer matrix, which in turn results in a material with intrinsic microporosity.<sup>367</sup> These materials are microporous (pores smaller than 2 nm) and possess a considerable fraction of pores that are below 7 Å.<sup>368</sup> Hydroxyl-functionalized PIMs (PIM-6FDA-OH) demonstrated higher permeabilities than most traditional polyimides for sour gas sweetening application.<sup>360,369</sup> Annealed PIM-6FDA-OH films were shown to resist plasticization up to much higher pressures compared to unannealed films and other 6FDA-based polyimide materials. These films were dried under vacuum at 100 °C to remove any moisture prior to testing. However, since processed natural gas, although with low dew point temperatures, may contain finite moisture levels, future research for these very promising, but hydrophilic, membranes should consider the effects of moisture on gas sweetening.

Several other research groups have been investigating polymeric membranes for H<sub>2</sub>S removal, from the 1950s right up until today,<sup>334,339,347,348,351–359,361,370–373</sup> and the data from some of these papers is also presented in Table 12. To maximize the membrane area per unit volume, two main configurations are widely used: hollow fibers and flat sheets in the form of spiral-wound modules. Both these module types are commercially applied for CO<sub>2</sub> removal from natural gas.<sup>331</sup>

#### 4.2. Membranes for Gas–Liquid Contact

In general, synthesizing highly selective gas membranes that also offer high flux is an active area of industrial and academic research. An alternative technology that combines the advantages of high surface area per unit volume of membrane contactors with the selective absorption in amine-based liquid solutions was first developed for CO<sub>2</sub> capture in 1985 by Qi and Cussler.<sup>375,376</sup> Such gas–liquid interfaces may be achieved by flowing a gas on the outside of a membrane configuration such as a hollow fiber and with liquid flowing within its lumen (see Figure 18). These gas–liquid membrane contactors offer several advantages over conventional contacting devices, such as high surface area per unit contactor volume; independent control of gas and liquid flow rates without any flooding, loading, weeping, foaming, or entrainment problems; small size; known gas–liquid interfacial area; and being modular and easy

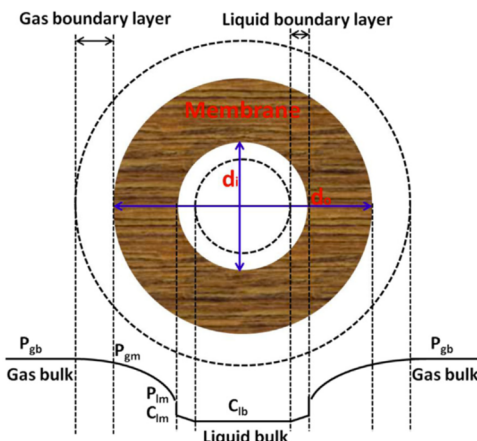


**Figure 18.** Cross section of a hollow fiber (gas on the shell side and liquid on the tube side).  $P$  and  $C$  are the gas partial pressure and liquid concentration, respectively. The subscripts  $gb$ ,  $gm$ ,  $lm$ , and  $lb$  represent gas bulk, gas–membrane interface, liquid–membrane interface, and liquid bulk, respectively. Reprinted with permission from ref 374. Copyright 2016 Elsevier.

to scale up or down.<sup>377</sup> Important aspects of membrane contactors for acid gas removal, including liquid absorbents, membrane characteristics, combination of membrane and

absorbent, mass transfer, and membrane modules, are critically discussed elsewhere by Mansourizadeh and Ismail.<sup>377</sup>

Asymmetric hollow-fiber membrane modules made of PSF and PESf, coupled with a concentrated alkaline NaOH solution, were investigated both experimentally and theoretically for the removal of H<sub>2</sub>S (see Table 13).<sup>378</sup> In general, the gas-phase diffusivity is about 4 orders of magnitude higher than the liquid-phase diffusivity. As a result, in the case of non-reactive absorption, the additional mass-transfer resistance contributed by a non-wetted membrane is significantly smaller than the resistance in the liquid phase. Thus, addition of a non-wetting membrane to a non-reactive gas–liquid system results in a negligible decrease in the overall mass-transfer coefficient. A non-wetting solvent–membrane combination can therefore greatly enhance the overall mass transfer ( $K_{\text{overall}} \times A$ ) of the soluble species from the gas phase to the liquid phase by virtue of higher surface area per unit volume ( $A$ ). Since reactive absorption in many cases shifts the rate-limiting step to the gas phase, having a wetted membrane can be beneficial over a non-wetted membrane in such cases. These are general guidelines and may vary from case to case, depending on the extent of equilibrium between a gas–liquid pair. In a subsequent study, Li et al. developed a PVDF membrane, and due to its excellent chemical resistance, much higher H<sub>2</sub>S feed concentration could be investigated.<sup>379</sup> Unlike other membrane-based processes such as ultra-filtration or molecular sieving, very small pressure

**Table 13. H<sub>2</sub>S Capture by Gas–Liquid Contact Using Hollow-Fiber Membrane Modules**

membrane	liquid	T (°C)	p (bar)	y <sub>H<sub>2</sub>S</sub> (ppm)	reference
PSF PESf	2.5 M NaOH	25	1–3.5	16–24	Li et al. <sup>378</sup>
PVDF	2.5 M NaOH 2 M Na <sub>2</sub> CO <sub>3</sub>	25	1–3.5 0.9–1.1 1.2–1.7	17.9–1159 1000	Li et al. <sup>379</sup> Wang et al. <sup>380</sup> Wang et al. <sup>381</sup>
ePTFE	H <sub>2</sub> O 0.1–2.0 M NaOH 0.1–2.0 M MEA 0.5 M DEA 0.5 M TETA	24	1–50	20000	Marzouk et al. <sup>382</sup>
PVDF PSF	0.84–2.0 M MDEA 0.84–1.84 M MDEA 0.84–1.0 M MDEA 0.84 M MDEA, 0.16 M DEA 0.84 M MDEA, 0.16 M MEA	25 25–45	1.3–1.6 1	1500–3100 1100–2200	Hedayat et al. <sup>383</sup>
ePTFE	H <sub>2</sub> O 0.1–2.0 M NaOH 0.5 M MEA 0.5 M DEA 0.5 M DETA	22	1–50	20000	Marzouk et al. <sup>384</sup>
PFA	H <sub>2</sub> O 0.1–2.0 M NaOH 0.5 M MEA 0.5 M DEA 0.5 M DETA				
PVDF	H <sub>2</sub> O 0.5 M MEA	25	N/A	250–1000	Rongwong et al. <sup>385</sup>

gradients need to be maintained across the gas–liquid interface, just enough to prevent bubbling of the gas in the liquid phase, since the driving force for mass transfer is the chemical potential (concentration) gradient. The effect of an alternate alkaline medium such as sodium carbonate ( $\text{Na}_2\text{CO}_3$ ) was also investigated, and complete removal of  $\text{H}_2\text{S}$  could be achieved with short residence times (<0.1 s).<sup>380</sup>  $\text{H}_2\text{S}$  removal in the presence of  $\text{CO}_2$  showed  $S_{\text{H}_2\text{S}/\text{CO}_2} = 180\text{--}200$ , about 1 order of magnitude higher than that reported for packed towers (10–30).<sup>381</sup> Note that here the selectivity is defined as the ratio of overall mass-transfer coefficients for  $\text{H}_2\text{S}$  and  $\text{CO}_2$  and may vary with the operating conditions of the packed tower and the membrane module. With the hollow fibers, the selectivity increased by 33% for a 6-fold increase in gas/liquid ratio and by 50% for a 3-fold increase in gas pressure, and was insensitive to the inlet concentration of  $\text{CO}_2$  over a wide range (5–25%).<sup>381</sup>

Marzouk et al. explored expanded polytetrafluoroethylene (ePTFE) hollow fibers for removal of high-concentration  $\text{H}_2\text{S}$  from a binary gas mixture (2%  $\text{H}_2\text{S}$  in  $\text{CH}_4$ ) at high pressures (up to 50 bar).<sup>382,384</sup> PTFE is a highly non-reactive polymer, mainly due to the strong strength of carbon–fluorine bonds; this non-reactivity allows the polymer to withstand highly corrosive  $\text{H}_2\text{S}$  environments. Additionally, fluorocarbons are known to be very hydrophobic, thus repelling water or water-containing solutions and in turn preventing wetting of the hollow fibers. It was observed that the ratio of flux in the case of NaOH solution to that in the case of distilled water (a physical absorbent) decreases from ~4.5 at 1 bar to ~1.35 at 50 bar. This seemingly small effect of alkaline solution at higher pressure amounts to ~75%  $\text{H}_2\text{S}$  removal for water and ~100%  $\text{H}_2\text{S}$  removal for 2 M NaOH solution. Performance for MEA was observed to be very similar to that for NaOH.  $\text{H}_2\text{S}$  flux rates were obtained with three different amines, i.e., MEA, DEA, and triethylenetetraamine (TETA), and it was shown that the flux followed the order TETA > MEA > DEA. TETA has four amino (Lewis base) sites, explaining its having the largest  $\text{H}_2\text{S}$  flux. The steric hindrance in MEA is lower compared to that in DEA, allowing better interaction of the Lewis base site with  $\text{H}_2\text{S}$ . The effect of simultaneous absorption of  $\text{CO}_2$  and  $\text{H}_2\text{S}$  from a pressurized  $\text{CO}_2\text{--H}_2\text{S}\text{--CH}_4$  gas mixture was investigated using ePTFE and a commercially available diblock polymer, poly(tetrafluoroethylene-co-perfluorinated alkyl vinyl ether) (PFA).<sup>384</sup> The results proved that the PFA fibers are superior to the more common ePTFE mainly because of their smaller dimensions, higher porosity, and higher hydrophobicity. Utilizing PFA fibers in the future would lead to substantial reduction in the membrane area (10 times) and/or significant enhancement in the acid gas removal efficiency. Since the contact angles for ePTFE and PFA are 111.3 and 118.6°, respectively, it is quite possible that a polymer with even higher hydrophobicity may further increase the membrane flux.

While liquid-phase resistance dominates mass transfer in the case of physisorption,<sup>384</sup> the gas-phase resistance dominates for reactive absorption in the liquid phase.<sup>383</sup> An increase in amine concentration in the absence of  $\text{CO}_2$  resulted in a decrease in the mass-transfer coefficient, and this was attributed to the enhanced wetting of the membrane resulting from reduced surface tension due to organic amines.<sup>383</sup> In the presence of  $\text{CO}_2$ , however, MDEA concentration enhanced the removal efficiency of  $\text{H}_2\text{S}$  as well as  $\text{CO}_2$ ; since MDEA is a tertiary amine, the  $\text{CO}_2$  molecules are not absorbed and stay in the gas–liquid interface within the membrane, hindering the

wetting of the membrane. The effect of temperature on the  $\text{H}_2\text{S}$  removal efficiency was small, but it substantially decreased the  $\text{CO}_2$  removal efficiency and consequently enhanced the  $\text{H}_2\text{S}$  selectivity.<sup>383</sup> Absorbent mixtures as well as acid gas mixtures affect the  $\text{H}_2\text{S}$  and  $\text{CO}_2$  removal efficiencies in complex ways. While the logic presented in the paper by Hedayat et al. makes sense, there are multiple phenomena going on in this system at the same time, and it is hard to deconvolute the problem; insights from molecular simulations, both equilibrium and non-equilibrium, can play a role in improving the understanding of the underlying phenomena.

Recently, Esquiroz-Molina et al. studied the effect of pH for alkaline NaOH solution on the mass transfer of  $\text{H}_2\text{S}$  in commercially available hollow-fiber membrane contactors made of hydrophobic polypropylene.<sup>386</sup> Theoretical gas side residence times were varied between 0.37 and 17 s, while the liquid side residence time was about 12 s. The authors determined a threshold pH of 10 ( $10^{-4}$  M), above which the reaction could be described as pseudo-first order with respect to  $\text{H}_2\text{S}$  due to an excess of reactive hydroxide ions. At pH > 10, the reactive absorption in the liquid phase increases the liquid-side mass-transfer coefficient enough to make the reaction gas-phase controlled. The authors propose a NaOH pH of 11 (0.001 M) to be economically attractive; this value is several orders of magnitude smaller than the concentrations previously investigated in the literature. It should be noted, however, that dilute solvents can reduce the cost of solvents but will greatly increase the regeneration cost of the spent absorbent. Such a reduction in concentration may be justifiable only for a very high value solvent.

Several groups have modeled  $\text{H}_2\text{S}$  removal using gas–liquid contact over hollow-fiber membrane modules.<sup>387–394</sup> Some of the models considered non-wetting and partial wetting conditions, where the gas mixture and the solvent, respectively, fill the membrane pores.<sup>388,394</sup> Axial and radial diffusion were considered inside the fiber, through the membrane, and within the shell using a two-dimensional (2D) mathematical model.<sup>388</sup> This 2D model was modified to account for the reversible reactions of all species involved in the chemical absorption of  $\text{H}_2\text{S}$  in aqueous carbonate solution<sup>389</sup> and then further extended to systems involving the presence of  $\text{CO}_2$ .<sup>390</sup> Amrei et al. presented a comprehensive model considering the entrance regions of momentum, energy, and mass transfers; compressibility of the gas phase as a function of gas-phase temperature, pressure, and composition; and variation of physical solubility of  $\text{CO}_2$  and  $\text{H}_2\text{S}$  as a function of gas–liquid interface temperature, pressure, and compositions.<sup>393</sup> Dynamic response of the membrane reactor to various types of pulses on the feed and solvent showed that the system was dynamically stable and reverted back to its previous operating point. It is worth noting that the modeling of flow in hollow-fiber contactors is not trivial. Inside the fiber, the assumption of a fully developed laminar parabolic velocity profile in a tube geometry works very well. However, due to poor knowledge of the shell-side geometry, the models for what happens on the outside of the hollow fibers may correlate one set of data but are rarely effective in general.<sup>395,396</sup> Another issue about hollow-fiber membranes that is not addressed in many studies is the unstable gas–liquid interface. To overcome this, Prasad and Sirkar put a higher static pressure on the phase which did not wet the membrane, pushing the interface back to a more stable location.<sup>397</sup> However, this may not work as well for polydisperse pores, and it is an issue that, if not addressed at the

design stage, may lead to considerable performance problems in actual practice.

In conclusion, hollow-fiber membrane contactors have shown some promise for selective H<sub>2</sub>S removal; especially the uncommon H<sub>2</sub>S/CO<sub>2</sub> selectivities are promising. A better understanding of the flow patterns may be obtained from reactive computational fluid dynamics. This will enable further insights into whether operating and design parameters such as wettability of the membrane have positive or detrimental effects in optimizing not only H<sub>2</sub>S capacity but also H<sub>2</sub>S/CH<sub>4</sub> and H<sub>2</sub>S/CO<sub>2</sub> selectivities.

#### 4.3. Ceramic Membranes

Ceramic membranes have the potential to precisely control transport properties of molecules with different sizes, shapes, and interaction strength, in turn allowing sieving at molecular length scales. Maghsoudi and Soltanieh investigated the simultaneous separation of H<sub>2</sub>S and CO<sub>2</sub> from CH<sub>4</sub> using a ceramic membrane of CHA-type zeolite.<sup>398</sup> Since polar impurities such as H<sub>2</sub>O, due to their large permanent dipole moments, may affect membrane performance, there is a considerable value attached to exploring high-silica zeolite membranes. An approximately 20 μm thick silica membrane was synthesized on a porous α-alumina disk, with repeating the crystallization process thrice to seal defects as judged from N<sub>2</sub> permeability tests. The elemental profiles for Al and Si along the cross section by EDX line scanning view showed that the zeolite layer has Si/Al ≈ 5. Before the actual permeance measurement, the feed and permeate sides were purged for 1 h with the desired feed and Ar, respectively, and Ar was also used as a carrier gas during the permeation measurements. Ternary mixture (2.13% CO<sub>2</sub>, 0.30% H<sub>2</sub>S in CH<sub>4</sub>) permeance was measured at room temperature, and the ratios of permeances for H<sub>2</sub>S/CH<sub>4</sub> and CO<sub>2</sub>/CH<sub>4</sub> were observed to be 3.24 and 5.3, respectively. When normalized by the ratio of feed concentrations, these values are 1050 and 240, respectively, suggesting that the potential for acid gas separation using zeolite membranes should be further explored.

#### 4.4. Carbon-Based Membranes

Pristine graphene is a two-dimensional, single-atomic-layer, hexagonal lattice of sp<sup>2</sup>-hybridized carbon atoms that is completely impervious to liquids and gases, including atoms as small as helium (2.6 Å).<sup>399</sup> Perforated graphene membranes with sub-nanometer micropores, also known as “porous graphene membranes”, have shown promise for numerous separation applications.<sup>400–408</sup> Nanoporous defect formation in single-atomic layers of graphene using high-resolution TEM was reported by Hashimoto et al.<sup>409</sup> In another approach, “bottom-up” synthesis has also been demonstrated using phenylene rings as building units to form porous graphene.<sup>410</sup> Although porous graphene membranes have been explored for the selective molecular sieving of He, H<sub>2</sub>, CO<sub>2</sub>, Ar, O<sub>2</sub>, N<sub>2</sub>, CO, and CH<sub>4</sub>, there is no experimental measurement for H<sub>2</sub>S, which should be explored in the future.

It is important to note here that a successful gas separation using a single-layer graphene membrane has not been reported. Most measurements are for a few-layers-thick graphene oxide membranes. This is likely to have strong implications on separations involving polar species such as H<sub>2</sub>S due to the different binding affinities of polar species toward pristine graphene surface compared to the functionalized surface of graphene oxide. Lei et al. carried out MD simulations to probe the effect of the charges around the pore on the separation of a

H<sub>2</sub>S/CH<sub>4</sub> mixture using a porous graphene membrane.<sup>411</sup> The pore was formed by deleting 12 C atoms from the center of the sheet in the simulation box, and partial charges of -0.241 and +0.241 e were assigned to the carbon atoms in the first and second 12-carbon shells. For the charged-pore membrane, the flux nearly doubled for H<sub>2</sub>S and nearly halved for CH<sub>4</sub>, resulting in a 4-fold increase in selectivity compared to the uncharged-pore membrane. In another simulation study, Sun et al. investigated different pore sizes and shapes for graphene membranes and found H<sub>2</sub>S/CH<sub>4</sub> selectivities in excess of 100 at reasonably high permeances.<sup>412</sup>

Another class of carbon-based membranes, carbon molecular sieve (CMS) membranes, which are prepared by the carbonization of polymeric precursors, have shown promising CO<sub>2</sub>/CH<sub>4</sub> selectivity (35–190) at high CO<sub>2</sub> flux of 10<sup>-6</sup>–10<sup>-8</sup> mol/(m<sup>2</sup>·s·Pa).<sup>413,414</sup> The utility of such membranes for selective H<sub>2</sub>S removal from natural gas streams remains to be explored.

Very recently, Wenz and Koros introduced a postsynthetic modification method using aromatic amines to bridge the sp<sup>2</sup> domains in CMS membranes with the goal to prevent relaxation of the CMS to suppress physical aging (see Figure 19).<sup>415</sup> However, the modifications were found insufficient to

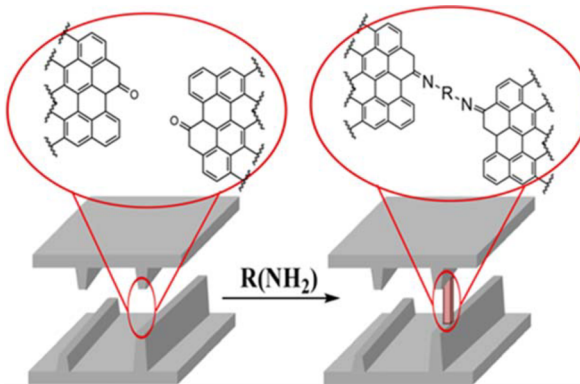


**Figure 19.** Schematic of amine doping concept, using the carbonyl functional groups as example reaction site. Reprinted with permission from ref 415. Copyright 2017 American Institute of Chemical Engineers.

yield aging-resistant membranes. This is an emerging field, and hopefully new synthetic techniques to prevent collapsing of CMS will emerge in the future.

Gilani and co-workers used vertically aligned CNT (VACNT) membranes,<sup>416</sup> functionalized with different amine groups, for separation of binary H<sub>2</sub>S/CH<sub>4</sub> mixtures (see Figure 20).<sup>417</sup> Permselectivity values between 2.5 and 3 and H<sub>2</sub>S permeabilities between 3 × 10<sup>-7</sup> and 8 × 10<sup>-7</sup> mol/(m<sup>2</sup>·s·Pa) were observed, depending on the choice of functional groups. Linear amines with a short carbon chain length lead to a higher selectivity and H<sub>2</sub>S permeability; the order of selectivity and H<sub>2</sub>S permeability of membranes was obtained as butylamine > dodecylamine > sec-butylamine > octadecylamine.

Controlling aggregation of individual carbon membrane units, ensuring uniformity of thickness, and tuning precise distribution of defects are important challenges in the area of carbon-based membranes that are still not fully mature. Goh et al. have recently reviewed carbon-based membranes with a focus on water purification and identified five strategic areas for future research, namely, concentration polarization, fouling, stability, scalability, and cost.<sup>252</sup> Stacked graphene and surface-

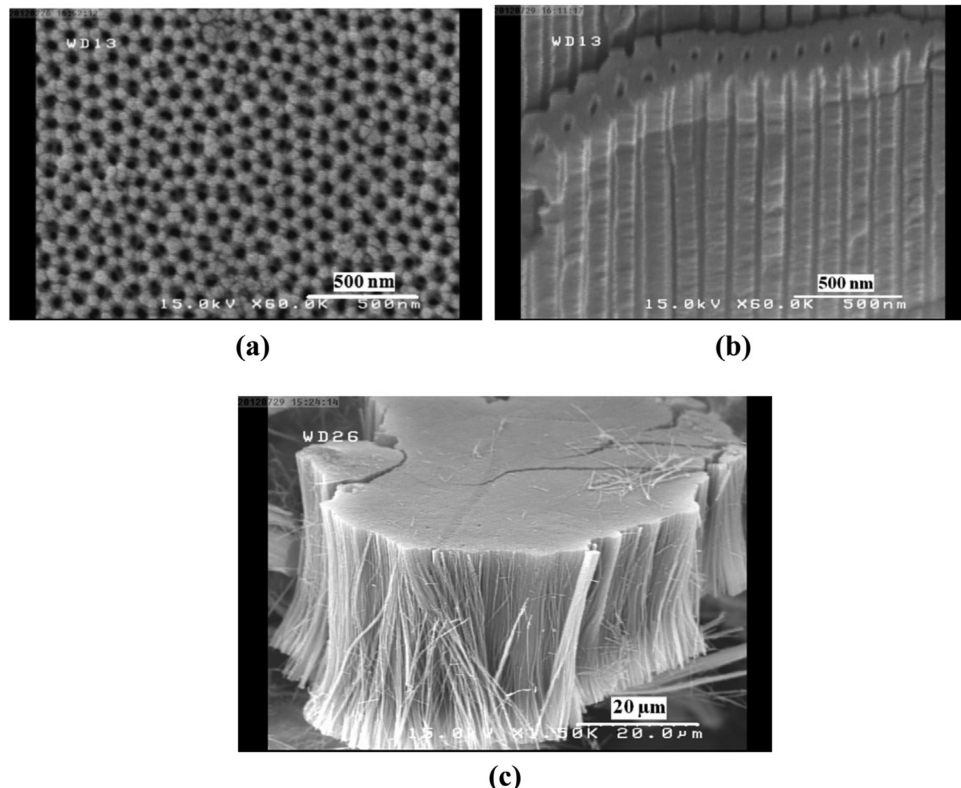


**Figure 20.** FESEM micrograph of (a) surface of anodic aluminum oxide (AAO) template, (b) cross section of AAO, and (c) VACNTs after removing AAO. Reprinted with permission from ref 417. Copyright 2016 Elsevier.

modified graphene are much more stable and scalable compared to single-layer graphene. Similarly, randomly aligned CNTs are more scalable compared to VACNT. Like in most research fields, even in carbon-based membranes, the pursuit of advanced performance faces competing characteristics such as scalability, stability, and cost-effectiveness.

#### 4.5. Composite Membranes

Supported ionic liquid membranes (SILMs) consist of an IL embedded in a solid polymer matrix (support). SILMs with 1-butyl-3-methylimidazolium tetrafluoroborate as the IL for its superior affinity to acidic gases, and PVDF as the polymer matrix for its hydrophobicity as well as stable physical and chemical properties, were tried for selective H<sub>2</sub>S removal.<sup>418,419</sup> The permeability coefficients increased dramatically, especially for H<sub>2</sub>S, with an increase in the IL content of the membrane. This increase may be due to enhancement in diffusion, since solubility does not vary much with IL loading.

Wang et al. computationally studied the separation of an H<sub>2</sub>S/CH<sub>4</sub> mixture in the UiO-66(Zr)-(COOH)<sub>2</sub> MOF membrane and the mixed matrix membranes (MMMs) composed of polymer as the continuous phase and MOF as the dispersed phase.<sup>420</sup> GCMC simulations using generic force fields that are known to show reasonable adsorption estimates for MOFs were used to obtain equilibrium loading at the conditions of interest. MD simulations were then employed to calculate diffusivities considering framework flexibility, and equivalent results were obtained from simulations in the canonical and the microcanonical ensembles. With a combination of atomistic simulations and the Maxwell–Stefan formulation for permeation,<sup>421</sup> H<sub>2</sub>S/CH<sub>4</sub> permselectivities of ~200 for UiO-66(Zr)-(COOH)<sub>2</sub>, 2–50 for the different polymers, and between 2 and 60 for MMMs were estimated.

Note that, for modeling the separation performance of MMMs, the permeability values of H<sub>2</sub>S/CH<sub>4</sub> mixtures through polymeric membranes were taken from the experimental data available in the literature, while those through the MOF phase were taken from the simulation results. It was found that, for polymers with much lower H<sub>2</sub>S permeabilities compared to the MOF, MOF addition into its matrix increases the permeability by about an order of magnitude for 50% volume fraction of the MOF and the selectivity remains almost unchanged at the polymer permselectivity. However, for polymers with H<sub>2</sub>S permeabilities not lower than 2 orders of magnitude compared to the MOF permeability, both selectivity and permeability of the polymer increase upon MOF addition. In a subsequent study, Li et al. carried out molecular simulations using generic MOF force fields (shown to have worked reasonably accurately in many previous studies) to study the adsorption and membrane performance of UiO-66(Zr) and its functionalized derivatives for H<sub>2</sub>S removal from binary mixtures with CH<sub>4</sub> and CO<sub>2</sub>.<sup>422</sup> UiO-66-(COOH)<sub>2</sub> and UiO-66-COOH performed better than other functionalized derivatives; however, the performance of these adsorbents/membranes containing hydrophilic functional groups, in the presence of moisture, remains to be seen.

#### 5. CRYOGENIC DISTILLATION

Although the phase behavior of the CH<sub>4</sub>/H<sub>2</sub>S system was studied extensively in the 1950s,<sup>423–425</sup> there has been renewed interest in the study of these systems at additional state points, especially at higher pressures, in the past couple of years.<sup>426–428</sup> Coquelet et al. investigated phase equilibria from −87 to 40 °C up to 140 bar,<sup>426</sup> and Perez et al. measured the mixture densities between −20 and 20 °C and up to pressures of 300

bar.<sup>428</sup> Lange et al. also explored the complete *pT* diagram of the methane–hydrogen sulfide system down 70 K and for pressures up to 2500 bar by tuning the parameters within a solid–liquid–vapor equation of state and validating against the available experimental data.<sup>427</sup>

Total, Institut Francais du Petrole, and its fully owned subsidiary, Prosernat, have developed a cryogenic process for bulk H<sub>2</sub>S removal from very sour gases, the SPREX (Special PRe-Extraction) process.<sup>429</sup> The pre-treatment step reduces the H<sub>2</sub>S content in the gas by producing a partially sweetened gas which can then be processed by a smaller sized amine sweetening unit; it also produces high-pressure liquid H<sub>2</sub>S (50–65 bar) that can be easily re-injected into a geological reservoir. The minimum overhead temperature is limited to about –30 °C, so as to remain above the hydrate formation temperature, ruling out the necessity of installing a dehydration unit upstream of the Sprex column. This temperature of –30 °C limits the H<sub>2</sub>S concentration in the distillate to about 10%. However, the authors also describe an enhanced version, where the temperature can be reduced to –65 °C without crystallizing CO<sub>2</sub> or H<sub>2</sub>S, thereby reducing the H<sub>2</sub>S content in the overhead stream to 2–3%. The triple point of H<sub>2</sub>S is about –85 °C, suggesting that the process is very close to where it can practically be, even if pre-drying is carried out to completely remove the moisture.

For many chemical separations, distillation has been the most straightforward and often long-lasting choice, unless an obvious better choice of separation was available. It is intriguing that, in the development of separation processes for gas sweetening, distillation has come into the picture only in the past decade or so. Distillation, in general, is a very energy-intensive process that requires boiling and condensing of the entire feed stream (a number of times for systems with low relative volatilities). However, for a raw gas stream (4.5 million S·m<sup>3</sup>/day) containing 35% H<sub>2</sub>S and 7% CO<sub>2</sub>, the capital expenditure, power consumption, and steam consumption of the amine process and the SPREX + amine process were reported to be 153 and 128 MM US\$, 52 and 30 MW, and 46 and 34 MW, respectively.<sup>429</sup> This shows that distillation can indeed be more cost-effective and energy-efficient as a pre-treatment step, compared to amine absorption, for bulk acid gas removal.<sup>429</sup>

## 6. OUTLOOK AND PERSPECTIVES

Considering the wide range of hydrogen sulfide concentrations in different natural gas reservoirs, a need for a portfolio of efficient (multi-step) separation processes is evident. In addition to H<sub>2</sub>S removal, other competing goals such as CO<sub>2</sub> removal, removal of other organic sulfur compounds, and moisture removal need to be considered where necessary. Before one can quantitatively compare many of the emerging materials described in this Review, further detailed investigations of these materials under conditions of interest (as discussed at appropriate places throughout the Review) are essential.

As far as liquid absorbents are concerned, processes based on alkanolamines have matured and been perfected over the past several decades. New research on amines for acid gas capture is evolving around developing solid supports, such as mesoporous silica, to uniformly disperse the amine functionalities, either physically or chemically bonded by silane chemistry, and to benefit from the advantages of adsorptive separations over absorptive separations. Since CO<sub>2</sub> is more acidic than H<sub>2</sub>S, developing H<sub>2</sub>S-selective alkanolamines was a big challenge that

was overcome for liquid absorbents. Similar breakthroughs for supported amines will be essential for efficient H<sub>2</sub>S capture. One such promising attempt employs variations in the operating conditions for a two-column setup: the first column at high temperature for absorption of CO<sub>2</sub>, and the second column at low temperature for removal of H<sub>2</sub>S without over-processing for CO<sub>2</sub>.<sup>300</sup> Adsorbents where aminopolymers are polymerized *in situ* on a porous support have not yet been tried for H<sub>2</sub>S capture, and this could constitute an important future investigation.

Ionic liquids are an emerging class of absorbents for selective acid gas removal; emphasis on understanding their structure and performance should remain the focus of fundamental investigations, and cost comparisons with commercial liquid solvents will help understand the true potential of these new liquids for sweetening applications. Deep eutectic solvents are another new class of absorbents; although these are explored only for CO<sub>2</sub> capture as of today, future studies may investigate H<sub>2</sub>S removal using these solvents. In addition to the performance metrics of capacity and selectivity, operational aspects, such as lowering the viscosity and aquatic toxicity of these new classes of solvents, are also likely to play an important role in the development of these new technologies.

Mixed metal oxides for reactive H<sub>2</sub>S removal have evolved empirically in most cases, and very little is known in the literature about the fundamental mechanisms governing improved performance. Some progress has been shown in the ZnO and Cu–Zn–O mixed oxide sulfidation mechanisms using TEM and *in situ* synchrotron XRD. An even better understanding of these reaction mechanisms may assist in designing mixed oxides with not only a high degree of regenerability but also structural reversibility on regeneration. The latter is more important for a stable bed performance over the life of the adsorbent. Some of the MOFs investigated in the literature have shown very high H<sub>2</sub>S capacities. Knowledge of thermal conductivities and specific heats of these materials becomes essential in the design of adsorption beds involving high exothermicity. In case of cation-exchanged zeolites, structural characterization of metallic species to elucidate whether these are located at catalytic ion-exchange sites or just as extra-framework metal oxides should help in understanding the performance on more fundamental grounds. Most literature studies on utilizing solids for mass separation focus on designing sorbents with higher selectivities and capacities; emphasis should also be levied on factors such as structural and performance regenerability, stability in the presence of strongly adsorbing/reacting impurities, heats of adsorption, specific heat capacities, and thermal conductivities. Future adsorbent screening should try to incorporate these diverse properties in the selection criteria.

Significant development has occurred in the scientific and technological improvement of polymeric membranes for sour gas sweetening. Synthesis and performance studies of thin membranes made from some of the promising polymeric materials should be undertaken in order to assess the potential of these membranes for commercial application. There is only one report in the literature using zeolitic membranes for H<sub>2</sub>S separation;<sup>398</sup> the results from this study seem to be promising and should be explored further. Use of porous graphene and carbon molecular sieve membranes for H<sub>2</sub>S capture also constitute an area of future investigation in the field. Mixed-matrix membranes composed of MOFs dispersed in polymeric materials have been modeled using theory and simulations.

Experimental and theoretical development of these next-generation membranes for gas sweetening will remain the research focus for the next decade or so.

Sulfur is mainly used in the production of sulfuric acid. Other uses of sulfur include manufacture of vulcanized rubber, building materials, inorganic chemicals, dyes, skin treatment ointments, matches, explosives, fertilizers, agrochemicals, fungicides, and fumigants. It is also useful in the bleaching of paper, extraction of minerals, and processing of wastewater. In recent years, increased processing of highly sour gas fields in the Middle East regions has resulted in a large surplus of sulfur, and research is being focused on developing new commercial applications of sulfur, such as battery materials and increased sulfur content of common plastics and building materials. Thus, the overall economics of highly sour gas wells may depend not only on the economics of acid gas removal but also on what one decides to do with the sulfur. Whether one can find high-value applications for sulfur, or store mountains of sulfur as inventory for future increase in demand, or maybe even reinject the H<sub>2</sub>S gas into depleted wells are the different aspects that may influence the choice of an H<sub>2</sub>S-removal process. Detailed economic analysis of competing bulk H<sub>2</sub>S removal processes, such as polymeric membrane separations, cryogenic distillation, all-silica zeolitic adsorbents, and combinations thereof, may help researchers arrive at the commercially optimal solution.

## AUTHOR INFORMATION

### Corresponding Author

\*E-mail: siepmann@umn.edu.

### ORCID

J. Ilja Siepmann: 0000-0003-2534-4507

### Notes

The authors declare no competing financial interest.

### Biographies

Mansi Shah received her bachelors degree (2012) in Chemical Engineering from the Institute of Chemical Technology (formerly known as UDCT), Mumbai. She is currently a Chemical Engineering Ph.D. candidate at the University of Minnesota and is advised by M. Tsapatsis and J. I. Siepmann. Her doctoral thesis focuses on integration of molecular simulations and experiments for the development of new materials and processes for gas separation.

Michael Tsapatsis joined the Department of Chemical Engineering and Materials Science at the University of Minnesota in September 2003 as a professor and currently holds the Amundson Chair. He received an Engineering Diploma (1988) from the University of Patras, Greece, and M.S. (1991) and Ph.D. (1994) degrees from the California Institute of Technology (Caltech) working with G. R. Gavalas. He was a postdoctoral fellow with M. E. Davis at Caltech (1993–1994). Before joining the University of Minnesota, he was a faculty member in the Chemical Engineering Department at the University of Massachusetts Amherst (1994–2003). He is a fellow of the American Association for the Advancement of Science and a member of the National Academy of Engineering.

J. Ilja Siepmann is a Distinguished McKnight University Professor and a Distinguished Teaching Professor and holds the Merck Professorship in Chemistry at the University of Minnesota. He received his Ph.D. in Chemistry from the University of Cambridge. Before joining the University of Minnesota in 1994, Dr. Siepmann carried out postdoctoral research at the IBM Zurich Research Laboratory, the

Royal/Shell Laboratory in Amsterdam, and the University of Pennsylvania's Laboratory for the Research on the Structure of Matter. His scientific interests are focused on particle-based simulations of complex chemical systems, including the predictions of phase and sorption equilibria and of thermophysical properties, the understanding of retention in chromatography, and the investigation of microheterogeneous fluids and nucleation phenomena.

## ACKNOWLEDGMENTS

The authors gratefully acknowledge discussions with Edward Cussler on membranes for gas–liquid contact. This research is supported by the U.S. Department of Energy, Office of Basic Energy Sciences, Division of Chemical Sciences, Geosciences and Biosciences under Award DE-FG02-12ER16362. M.T. acknowledges support through the Center for Gas Separations Relevant to Clean Energy Technologies, an Energy Frontier Research Center funded by the U.S. Department of Energy, Office of Science, Basic Energy Sciences under Award DE-SC000105. M.S.S. gratefully acknowledges financial support from University of Minnesota through a Graduate School Doctoral Dissertation Fellowship.

## REFERENCES

- (1) United States Department of Labor, Occupational Safety and Health Administration. Hydrogen Sulfide, Hazards, <https://www.osha.gov/SLTC/hydrogensulfide/hazards.html> [accessed May 5, 2017].
- (2) Hammer, G.; Lübecke, T.; Kettner, R.; Pillarella, M. R.; Recknagel, H.; Commichau, A.; Neumann, H.; Paczynska-Lahme, B. *Natural Gas. Ullmann's Encyclopedia of Industrial Chemistry*; Wiley-VCH Verlag GmbH & Co. KGaA: Weinheim, 2006.
- (3) Awe, O. W.; Zhao, Y.; Nzhou, A.; Minh, D. P.; Lyczko, N. A Review of Biogas Utilisation, Purification and Upgrading Technologies. *Waste Biomass Valorization* **2017**, *8*, 267–283.
- (4) U.S. Department of Energy, The National Energy Technology Laboratory. Gasification Introduction, Syngas Composition, <https://www.netl.doe.gov/research/coal/energy-systems/gasification/gasifipedia/syngas-composition> [accessed May 5, 2017].
- (5) Emission Factor and Inventory Group, Office of Air Quality Planning and Standards. Petroleum Industry. *Compilation of Air Pollutant Emission Factors. Vol. 1: Stationary Point and Area Sources*, AP-42, 5th ed.; U.S. Environmental Protection Agency: Research Triangle Park, NC, January 1995; Chapter 5.
- (6) Gamson, B. W.; Elkins, R. H. Sulfur from Hydrogen Sulfide. *Chem. Eng. Prog.* **1953**, *49*, 203–215.
- (7) Sumida, K.; Rogow, D. L.; Mason, J. A.; McDonald, T. M.; Bloch, E. D.; Herm, Z. R.; Bae, T.-H.; Long, J. R. Carbon Dioxide Capture in Metal-Organic Frameworks. *Chem. Rev.* **2012**, *112*, 724–781.
- (8) Pera-Titus, M. Porous Inorganic Membranes for CO<sub>2</sub> Capture. *Chem. Rev.* **2014**, *114*, 1413–1492.
- (9) Sanz-Pérez, E. S.; Murdock, C. R.; Didas, S. A.; Jones, C. W. Direct Capture of CO<sub>2</sub> from Ambient Air. *Chem. Rev.* **2016**, *116*, 11840–11876.
- (10) Tabatabaei-Mohammadi, A. A Review of the Applications of Membrane Separation Technology in Natural Gas Treatment. *Sep. Sci. Technol.* **1999**, *34*, 2095–2111.
- (11) Abatzoglou, N.; Boivin, S. A Review of Biogas Purification Processes. *Biofuels, Bioprod. Biorefin.* **2009**, *3*, 42–71.
- (12) Wiheeb, A. D.; Shamsudin, I. K.; Ahmad, M. A.; Murat, M. N.; Kim, J.; Othman, M. R. Present Technologies for Hydrogen Sulfide Removal from Gaseous Mixtures. *Rev. Chem. Eng.* **2013**, *29*, 449–470.
- (13) Wang, L.; Yang, R. T. New Nanostructured Sorbents for Desulfurization of Natural Gas. *Front. Chem. Sci. Eng.* **2014**, *8*, 8–19.
- (14) Ahmed, I.; Jhung, S. H. Adsorptive Desulfurization and Denitrogenation Using Metal-Organic Frameworks. *J. Hazard. Mater.* **2016**, *301*, 259–276.

- (15) Vellingiri, K.; Deep, A.; Kim, K.-H. Metal-Organic Frameworks as a Potential Platform for Selective Treatment of Gaseous Sulfur Compounds. *ACS Appl. Mater. Interfaces* **2016**, *8*, 29835–29857.
- (16) George, G.; Bhoria, N.; AlHallaq, S.; Abdala, A.; Mittal, V. Polymer Membranes for Acid Gas Removal from Natural Gas. *Sep. Purif. Technol.* **2016**, *158*, 333–356.
- (17) Muñoz, R.; Meier, L.; Diaz, I.; Jeison, D. A Review on the State-of-the-Art of Physical/Chemical and Biological Technologies for Biogas Upgrading. *Rev. Environ. Sci. Bio/Technol.* **2015**, *14*, 727–759.
- (18) Jensen, A. B.; Webb, C. Treatment of H<sub>2</sub>S-Containing Gases: A Review of Microbiological Alternatives. *Enzyme Microb. Technol.* **1995**, *17*, 2–10.
- (19) Syed, M.; Soreanu, G.; Falletta, P.; Béland, M. Removal of Hydrogen Sulfide from Gas Streams Using Biological Processes - A Review. *Can. Biosyst. Eng.* **2006**, *48*, 2.
- (20) Piéplu, A.; Saur, O.; Lavalle, J.-C.; Legendre, O.; Nédez, C. Claus Catalysis and H<sub>2</sub>S Selective Oxidation. *Catal. Rev.: Sci. Eng.* **1998**, *40*, 409–450.
- (21) Pandey, R. A.; Malhotra, S. Desulfurization of Gaseous Fuels with Recovery of Elemental Sulfur: An Overview. *Crit. Rev. Environ. Sci. Technol.* **1999**, *29*, 229–268.
- (22) Eow, J. S. Recovery of Sulfur from Sour Acid Gas: A Review of the Technology. *Environ. Prog.* **2002**, *21*, 143–162.
- (23) Reverberi, A. P.; Klemeš, J. J.; Varbanov, P. S.; Fabiano, B. A Review on Hydrogen Production from Hydrogen Sulphide by Chemical and Photochemical Methods. *J. Cleaner Prod.* **2016**, *136*, 72–80.
- (24) Bottoms, R. R. Process for Separating Acidic Gases. U.S. Patent US1,783,901, 1930.
- (25) Frazier, H. D.; Kohl, A. L. Selective Absorption of Hydrogen Sulfide from Gas Streams. *Ind. Eng. Chem.* **1950**, *42*, 2288–2292.
- (26) Carey, T. R.; Hermes, J. E.; Rochelle, G. T. A Model of Acid Gas Absorption/Stripping Using Methylidiethanolamine with Added Acid. *Gas Sep. Purif.* **1991**, *5*, 95–109.
- (27) Mandal, B. P.; Biswas, A. K.; Bandyopadhyay, S. S. Selective Absorption of H<sub>2</sub>S from Gas Streams Containing H<sub>2</sub>S and CO<sub>2</sub> into Aqueous Solutions of N-Methylidiethanolamine and 2-Amino-2-Methyl-1-Propanol. *Sep. Purif. Technol.* **2004**, *35*, 191–202.
- (28) Saha, A. K.; Bandyopadhyay, S. S.; Saju, P.; Biswas, A. K. Selective Removal of Hydrogen Sulfide from Gases Containing Hydrogen Sulfide and Carbon Dioxide by Absorption into Aqueous Solutions of 2-Amino-2-methyl-1-propanol. *Ind. Eng. Chem. Res.* **1993**, *32*, 3051–3055.
- (29) Sartori, G.; Savage, D. W. Sterically Hindered Amines for Carbon Dioxide Removal from Gases. *Ind. Eng. Chem. Fundam.* **1983**, *22*, 239–249.
- (30) Suleiman, H.; Maulud, A. S.; Man, Z. Review and Selection Criteria of Classical Thermodynamic Models for Acid Gas Absorption in Aqueous Alkanolamines. *Rev. Chem. Eng.* **2015**, *31*, 599–639.
- (31) Kohl, A. L.; Nielsen, R. B. *Gas Purification*, 5th ed.; Gulf Publishing Co.: Houston, TX, 1997.
- (32) Minkkinen, A.; Larue, J. Y. M.; Patel, S.; Levier, J.-F. Methanol Gas-Treating Scheme Offers Economics, Versatility. *Oil Gas J.* **1992**, 90.
- (33) Ranke, G.; Mohr, V. H. The Rectisol Wash: New Developments in Acid Gas Removal from Synthesis Gas. In *Acid and Sour Gas Treating Processes*; Newman, S. A., Ed.; Gulf Publishing Co.: Houston, TX, 1985; pp 80–111.
- (34) Burr, B.; Lyddon, L. A Comparison of Physical Solvents for Acid Gas Removal, 87th Annual Gas Processors Association Convention, Grapevine, TX, March 2008.
- (35) Hochgesand, G. Rectisol and Purisol. *Ind. Eng. Chem.* **1970**, *62*, 37–43.
- (36) Roberts, B. E.; Mather, A. E. Solubility of H<sub>2</sub>S and CO<sub>2</sub> in Sulfolane. *Can. J. Chem. Eng.* **1988**, *66*, 519–520.
- (37) Dunn, C. L.; Freitas, E. R.; Goodenbour, J. W.; Henderson, H. T.; Papadopoulos, M. N. Sulfinol Process. *Oil Gas J.* **1964**, *62*, 95–98.
- (38) Rivas, O. R.; Prausnitz, J. M. Sweetening of Sour Natural Gases by Mixed-Solvent Absorption: Solubilities of Ethane, Carbon Dioxide, and Hydrogen Sulfide in Mixtures of Physical and Chemical Solvents. *AIChE J.* **1979**, *25*, 975–984.
- (39) Roberts, B. E.; Mather, A. E. Solubility of CO<sub>2</sub> and H<sub>2</sub>S in a Mixed Solvent. *Chem. Eng. Commun.* **1988**, *72*, 201–211.
- (40) Macgregor, R. J.; Mather, A. E. Equilibrium Solubility of H<sub>2</sub>S and CO<sub>2</sub> and Their Mixtures in a Mixed Solvent. *Can. J. Chem. Eng.* **1991**, *69*, 1357–1366.
- (41) Jenab, M. H.; Abdi, M. A.; Najibi, S. H.; Vahidi, M.; Matin, N. S. Solubility of Carbon Dioxide in Aqueous Mixtures of N-Methylidiethanolamine + Piperazine + Sulfolane. *J. Chem. Eng. Data* **2005**, *50*, 583–586.
- (42) Mokhatab, S.; Poe, W. A.; Mark, J. Y. *Handbook of Natural Gas Transmission and Processing*; Gulf Professional Publishing, 2012.
- (43) Lei, Z.; Dai, C.; Chen, B. Gas Solubility in Ionic Liquids. *Chem. Rev.* **2014**, *114*, 1289–1326.
- (44) Karadas, F.; Atilhan, M.; Aparicio, S. Review on the Use of Ionic Liquids (ILs) as Alternative Fluids for CO<sub>2</sub> Capture and Natural Gas Sweetening. *Energy Fuels* **2010**, *24*, 5817–5828.
- (45) Bara, J. E. *Green Solvents II*; Springer: Berlin, 2012; pp 155–167.
- (46) Kumar, S.; Cho, J. H.; Moon, I. Ionic Liquid-Amine Blends and CO<sub>2</sub> BOLs: Prospective Solvents for Natural Gas Sweetening and CO<sub>2</sub> Capture Technology-A Review. *Int. J. Greenhouse Gas Control* **2014**, *20*, 87–116.
- (47) Jou, F.-Y.; Mather, A. E. Solubility of Hydrogen Sulfide in [bmim][PF<sub>6</sub>]. *Int. J. Thermophys.* **2007**, *28*, 490–495.
- (48) Anthony, J. L.; Maginn, E. J.; Brennecke, J. F. Solubilities and Thermodynamic Properties of Gases in the Ionic Liquid 1-n-Butyl-3-Methylimidazolium Hexafluorophosphate. *J. Phys. Chem. B* **2002**, *106*, 7315–7320.
- (49) Jalili, A. H.; Rahmati-Rostami, M.; Ghotbi, C.; Hosseini-Jenab, M.; Ahmadi, A. N. Solubility of H<sub>2</sub>S in Ionic Liquids [bmim][PF<sub>6</sub>], [bmim][BF<sub>4</sub>], and [bmim][Tf<sub>2</sub>N]. *J. Chem. Eng. Data* **2009**, *54*, 1844–1849.
- (50) Raeissi, S.; Peters, C. J. High Pressure Phase Behaviour of Methane in 1-Butyl-3-Methylimidazolium Bis-(trifluoromethylsulfonyl)imide. *Fluid Phase Equilib.* **2010**, *294*, 67–71.
- (51) Jacquemin, J.; Gomes, M. F. C.; Husson, P.; Majer, V. Solubility of Carbon Dioxide, Ethane, Methane, Oxygen, Nitrogen, Hydrogen, Argon, and Carbon Monoxide in 1-Butyl-3-Methylimidazolium Tetrafluoroborate Between Temperatures 283 and 343 K and at Pressures Close to Atmospheric. *J. Chem. Thermodyn.* **2006**, *38*, 490–502.
- (52) Rahmati-Rostami, M.; Ghotbi, C.; Hosseini-Jenab, M.; Ahmadi, A. N.; Jalili, A. H. Solubility of H<sub>2</sub>S in Ionic Liquids [hmim][PF<sub>6</sub>], [hmim][BF<sub>4</sub>], and [hmim][Tf<sub>2</sub>N]. *J. Chem. Thermodyn.* **2009**, *41*, 1052–1055.
- (53) Finotello, A.; Bara, J. E.; Camper, D.; Noble, R. D. Room-Temperature Ionic Liquids: Temperature Dependence of Gas Solubility Selectivity. *Ind. Eng. Chem. Res.* **2008**, *47*, 3453–3459.
- (54) Sakhaeinia, H.; Taghikhani, V.; Jalili, A. H.; Mehdizadeh, A.; Safekordi, A. A. Solubility of H<sub>2</sub>S in 1-(2-Hydroxyethyl)-3-Methylimidazolium Ionic Liquids with Different Anions. *Fluid Phase Equilib.* **2010**, *298*, 303–309.
- (55) Shokouhi, M.; Adibi, M.; Jalili, A. H.; Hosseini-Jenab, M.; Mehdizadeh, A. Solubility and Diffusion of H<sub>2</sub>S and CO<sub>2</sub> in the Ionic Liquid 1-(2-Hydroxyethyl)-3-Methylimidazolium Tetrafluoroborate. *J. Chem. Eng. Data* **2010**, *55*, 1663–1668.
- (56) Sakhaeinia, H.; Jalili, A. H.; Taghikhani, V.; Safekordi, A. A. Solubility of H<sub>2</sub>S in Ionic Liquids 1-Ethyl-3-methylimidazolium Hexafluorophosphate ([emim][PF<sub>6</sub>]) and 1-Ethyl-3-methylimidazolium Bis(trifluoromethyl)sulfonylimide ([emim][Tf<sub>2</sub>N]). *J. Chem. Eng. Data* **2010**, *55*, 5839–5845.
- (57) Jalili, A. H.; Mehdizadeh, A.; Shokouhi, M.; Ahmadi, A. N.; Hosseini-Jenab, M.; Fatemianassab, F. Solubility and Diffusion of CO<sub>2</sub> and H<sub>2</sub>S in the Ionic Liquid 1-Ethyl-3-Methylimidazolium Ethylsulfate. *J. Chem. Thermodyn.* **2010**, *42*, 1298–1303.
- (58) Jalili, A. H.; Safavi, M.; Ghotbi, C.; Mehdizadeh, A.; Hosseini-Jenab, M.; Taghikhani, V. Solubility of CO<sub>2</sub>, H<sub>2</sub>S, and Their Mixture in

- the Ionic Liquid 1-Octyl-3-Methylimidazolium Bis (Trifluoromethyl) Sulfonylimide. *J. Phys. Chem. B* **2012**, *116*, 2758–2774.
- (59) Huang, K.; Cai, D.-N.; Chen, Y.-L.; Wu, Y.-T.; Hu, X.-B.; Zhang, Z.-B. Thermodynamic Validation of 1-Alkyl-3-Methylimidazolium Carboxylates as Task-Specific Ionic Liquids for H<sub>2</sub>S Absorption. *AIChE J.* **2013**, *59*, 2227–2235.
- (60) Huang, K.; Zhang, X.-M.; Xu, Y.; Wu, Y.-T.; Hu, X.-B.; Xu, Y. Protic Ionic Liquids for the Selective Absorption of H<sub>2</sub>S from CO<sub>2</sub>: Thermodynamic Analysis. *AIChE J.* **2014**, *60*, 4232–4240.
- (61) Huang, K.; Zhang, X.-M.; Hu, X.-B.; Wu, Y.-T. Hydrophobic Protic Ionic Liquids Tethered with Tertiary Amine Group for Highly Efficient and Selective Absorption of H<sub>2</sub>S from CO<sub>2</sub>. *AIChE J.* **2016**, *62*, 4480–4490.
- (62) Pomelli, C. S.; Chiappe, C.; Vidis, A.; Laurenczy, G.; Dyson, P. J. Influence of the Interaction Between Hydrogen Sulfide and Ionic Liquids on Solubility: Experimental and Theoretical Investigation. *J. Phys. Chem. B* **2007**, *111*, 13014–13019.
- (63) Singh, R.; Marin-Rimoldi, E.; Maginn, E. J. A Monte Carlo Simulation Study To Predict the Solubility of Carbon Dioxide, Hydrogen, and Their Mixture in the Ionic Liquids 1-Alkyl-3-Methylimidazolium Bis(trifluoromethanesulfonyl) Amide ([C<sub>n</sub>mim]<sup>+</sup>·[Tf<sub>2</sub>N]<sup>-</sup>], n = 4, 6. *Ind. Eng. Chem. Res.* **2015**, *54*, 4385–4395.
- (64) Budhathoki, S.; Shah, J. K.; Maginn, E. J. Molecular Simulation Study of the Solubility, Diffusivity and Permselectivity of Pure and Binary Mixtures of CO<sub>2</sub> and CH<sub>4</sub> in the Ionic Liquid 1-n-Butyl-3-Methylimidazolium Bis(trifluoromethylsulfonyl) Imide. *Ind. Eng. Chem. Res.* **2015**, *54*, 8821–8828.
- (65) Sánchez-Badillo, J.; Gallo, M.; Alvarado, S.; Glossman-Mitnik, D. Solvation Thermodynamic Properties of Hydrogen Sulfide in [C<sub>4</sub>mim][PF<sub>6</sub>],[C<sub>4</sub>mim][BF<sub>4</sub>], and [C<sub>4</sub>mim][Cl] Ionic Liquids, Determined by Molecular Simulations. *J. Phys. Chem. B* **2015**, *119*, 10727–10737.
- (66) Ramdin, M.; Balaji, S. P.; Vicent-Luna, J. M.; Gutiérrez-Sevillano, J. J.; Calero, S.; de Loos, T. W.; Vlugt, T. J. H. Solubility of the Precombustion Gases CO<sub>2</sub>, CH<sub>4</sub>, CO, H<sub>2</sub>, N<sub>2</sub>, and H<sub>2</sub>S in the Ionic Liquid [bmim][Tf<sub>2</sub>N] from Monte Carlo Simulations. *J. Phys. Chem. C* **2014**, *118*, 23599–23604.
- (67) Jamali, S. H.; Ramdin, M.; Becker, T. M.; Torres-Knoop, A.; Dubbeldam, D.; Buijs, W.; Vlugt, T. J. H. Solubility of Sulfur Compounds in Commercial Physical Solvents and an Ionic Liquid from Monte Carlo Simulations. *Fluid Phase Equilib.* **2017**, *433*, 50–55.
- (68) Heintz, Y. J.; Sehabiague, L.; Morsi, B. I.; Jones, K. L.; Luebke, D. R.; Pennline, H. W. Hydrogen Sulfide and Carbon Dioxide Removal from Dry Fuel Gas Streams Using an Ionic Liquid as a Physical Solvent. *Energy Fuels* **2009**, *23*, 4822–4830.
- (69) Carvalho, P. J.; Coutinho, J. A. P. Non-Ideality of Solutions of NH<sub>3</sub>, SO<sub>2</sub>, and H<sub>2</sub>S in Ionic Liquids and the Prediction of Their Solubilities Using the Flory-Huggins Model. *Energy Fuels* **2010**, *24*, 6662–6666.
- (70) Camper, D.; Bara, J.; Koval, C.; Noble, R. Bulk-Fluid Solubility and Membrane Feasibility of Rmim-Based Room-Temperature Ionic Liquids. *Ind. Eng. Chem. Res.* **2006**, *45*, 6279–6283.
- (71) Scovazzo, P. Determination of the Upper Limits, Benchmarks, and Critical Properties for Gas Separations Using Stabilized Room Temperature Ionic Liquid Membranes (SILMs) for the Purpose of Guiding Future Research. *J. Membr. Sci.* **2009**, *343*, 199–211.
- (72) Carvalho, P. J.; Coutinho, J. A. P. The Polarity Effect Upon the Methane Solubility in Ionic Liquids: A Contribution for the Design of Ionic Liquids for Enhanced CO<sub>2</sub>/CH<sub>4</sub> and H<sub>2</sub>S/CH<sub>4</sub> Selectivities. *Energy Environ. Sci.* **2011**, *4*, 4614–4619.
- (73) Alcalde, R.; Garcia, G.; Atilhan, M.; Aparicio, S. Systematic Study on the Viscosity of Ionic Liquids: Measurement and Prediction. *Ind. Eng. Chem. Res.* **2015**, *54*, 10918–10924.
- (74) Koller, T. M.; Heller, A.; Rausch, M. H.; Wasserscheid, P.; Economou, I. G.; Fröba, A. P. Mutual and Self-Diffusivities in Binary Mixtures of [EMIM][B(CN)<sub>4</sub>] with Dissolved Gases by Using Dynamic Light Scattering and Molecular Dynamics Simulations. *J. Phys. Chem. B* **2015**, *119*, 8583–8592.
- (75) Bates, E. D.; Mayton, R. D.; Ntai, I.; Davis, J. H. CO<sub>2</sub> Capture by a Task-Specific Ionic Liquid. *J. Am. Chem. Soc.* **2002**, *124*, 926–927.
- (76) Shiflett, M. B.; Yokozeki, A. Phase Behavior of Carbon Dioxide in Ionic Liquids: [emim][Acetate],[emim][Trifluoroacetate], and [emim][Acetate]+[emim][Trifluoroacetate] Mixtures. *J. Chem. Eng. Data* **2009**, *54*, 108–114.
- (77) Huang, K.; Cai, D.-N.; Chen, Y.-L.; Wu, Y.-T.; Hu, X.-B.; Zhang, Z.-B. Dual Lewis Base Functionalization of Ionic Liquids for Highly Efficient and Selective Capture of H<sub>2</sub>S. *ChemPlusChem* **2014**, *79*, 241–249.
- (78) Greaves, T. L.; Drummond, C. J. Protic Ionic Liquids: Properties and Applications. *Chem. Rev.* **2008**, *108*, 206–237.
- (79) Freire, M. G.; Santos, L. M. N. B. F.; Fernandes, A. M.; Coutinho, J. A. P.; Marrucho, I. M. An Overview of the Mutual Solubilities of Water-Imidazolium-Based Ionic Liquids Systems. *Fluid Phase Equilib.* **2007**, *261*, 449–454.
- (80) Rogers, R. D.; Seddon, K. R. Ionic Liquids-Solvents of the Future? *Science* **2003**, *302*, 792–793.
- (81) Guo, B.; Duan, E.; Zhong, Y.; Gao, L.; Zhang, X.; Zhao, D. Absorption and Oxidation of H<sub>2</sub>S in Caprolactam Tetrabutyl Ammonium Bromide Ionic Liquid. *Energy Fuels* **2011**, *25*, 159–161.
- (82) Heldebrant, D. J.; Yonker, C. R.; Jessop, P. G.; Phan, L. Organic Liquid CO<sub>2</sub> Capture Agents with High Gravimetric CO<sub>2</sub> Capacity. *Energy Environ. Sci.* **2008**, *1*, 487–493.
- (83) Heldebrant, D. J.; Yonker, C. R.; Jessop, P. G.; Phan, L. Reversible Uptake of COS, CS<sub>2</sub>, and SO<sub>2</sub>: Ionic Liquids with O-Alkylxanthate, O-Alkylthiocarbonyl, and O-Alkylsulfite Anions. *Chem. - Eur. J.* **2009**, *15*, 7619–7627.
- (84) Koech, P. K.; Rainbolt, J. E.; Bearden, M. D.; Zheng, F.; Heldebrant, D. J. Chemically Selective Gas Sweetening Without Thermal-Swing Regeneration. *Energy Environ. Sci.* **2011**, *4*, 1385–1390.
- (85) Abbott, A. P.; Capper, G.; Davies, D. L.; Munro, H. L.; Rasheed, R. K.; Tambyrajah, V. Preparation of Novel, Moisture-Stable, Lewis-Acidic Ionic Liquids Containing Quaternary Ammonium Salts With Functional Side Chains. *Chem. Commun.* **2001**, 2010–2011.
- (86) Smith, E. L.; Abbott, A. P.; Ryder, K. S. Deep Eutectic Solvents (DESs) and Their Applications. *Chem. Rev.* **2014**, *114*, 11060–11082.
- (87) Li, X.; Hou, M.; Han, B.; Wang, X.; Zou, L. Solubility of CO<sub>2</sub> in a Choline Chloride + Urea Eutectic Mixture. *J. Chem. Eng. Data* **2008**, *53*, 548–550.
- (88) Sarmad, S.; Xie, Y.; Mikkola, J.-P.; Ji, X. Screening of Deep Eutectic Solvents (DESs) as Green CO<sub>2</sub> Sorbents: From Solubility to Viscosity. *New J. Chem.* **2017**, *41*, 290–301.
- (89) Aissaoui, T.; Al Nashef, I. M.; Qureshi, U. A.; Benguerba, Y. Potential Applications of Deep Eutectic Solvents in Natural Gas Sweetening for CO<sub>2</sub> Capture. *Rev. Chem. Eng.* **2017**, DOI: 10.1515/revece-2016-0013.
- (90) Rahmati-Rostami, M.; Behzadi, B.; Ghotbi, C. Thermodynamic Modeling of Hydrogen Sulfide Solubility in Ionic Liquids Using Modified SAFT-VR and PC-SAFT Equations of State. *Fluid Phase Equilib.* **2011**, *309*, 179–189.
- (91) Llovel, F.; Marcos, R. M.; MacDowell, N.; Vega, L. F. Modeling the Absorption of Weak Electrolytes and Acid Gases with Ionic Liquids Using the Soft-SAFT Approach. *J. Phys. Chem. B* **2012**, *116*, 7709–7718.
- (92) Shahriari, R.; Dehghani, M. R.; Behzadi, B. A Modified Polar PHSC Model for Thermodynamic Modeling of Gas Solubility in Ionic Liquids. *Fluid Phase Equilib.* **2012**, *313*, 60–72.
- (93) Jalili, A. H.; Shokouhi, M.; Maurer, G.; Hosseini-Jenab, M. Solubility of CO<sub>2</sub> and H<sub>2</sub>S in the Ionic Liquid 1-Ethyl-3-Methylimidazolium Tris (Pentafluoroethyl) Trifluorophosphate. *J. Chem. Thermodyn.* **2013**, *67*, 55–62.
- (94) Safavi, M.; Ghotbi, C.; Taghikhani, V.; Jalili, A. H.; Mehdizadeh, A. Study of the Solubility of CO<sub>2</sub>, H<sub>2</sub>S and Their Mixture in the Ionic Liquid 1-Octyl-3-Methylimidazolium Hexafluorophosphate: Experimental and Modelling. *J. Chem. Thermodyn.* **2013**, *65*, 220–232.

- (95) Faúndez, C. A.; Díaz-Valdés, J. F.; Valderrama, J. O. Testing Solubility Data of H<sub>2</sub>S and SO<sub>2</sub> in Ionic Liquids for Sulfur-Removal Processes. *Fluid Phase Equilib.* **2014**, *375*, 152–160.
- (96) Ji, X.; Held, C.; Sadowski, G. Modeling Imidazolium-Based Ionic Liquids With ePC-SAFT. Part II. Application to H<sub>2</sub>S and Synthesis-Gas Components. *Fluid Phase Equilib.* **2014**, *363*, 59–65.
- (97) Haghtalab, A.; Kheiri, A. High Pressure Measurement Equation of State for Solubility of Carbon Dioxide and Hydrogen Sulfide in 1-Butyl-3-Methylimidazolium Acetate. *J. Chem. Thermodyn.* **2015**, *89*, 41–50.
- (98) Llorell, F.; Oliveira, M. B.; Coutinho, J. A. P.; Vega, L. F. Solubility of Greenhouse and Acid Gases on the [C<sub>4</sub>mim][MeSO<sub>4</sub>] Ionic Liquid for Gas Separation and CO<sub>2</sub> Conversion. *Catal. Today* **2015**, *255*, 87–96.
- (99) Vega, L. F.; Vilaseca, O.; Llorell, F.; Andreu, J. S. Modeling Ionic Liquids and the Solubility of Gases in Them: Recent Advances and Perspectives. *Fluid Phase Equilib.* **2010**, *294*, 15–30.
- (100) Ahmadi, M. A.; Haghbakhsh, R.; Soleimani, R.; Bajestani, M. B. Estimation of H<sub>2</sub>S Solubility in Ionic Liquids Using a Rigorous Method. *J. Supercrit. Fluids* **2014**, *92*, 60–69.
- (101) Shafiei, A.; Ahmadi, M. A.; Zaheri, S. H.; Baghban, A.; Amirfakhrin, A.; Soleimani, R. Estimating Hydrogen Sulfide Solubility in Ionic Liquids Using a Machine Learning Approach. *J. Supercrit. Fluids* **2014**, *95*, 525–534.
- (102) Ahmadi, M.-A.; Pouladi, B.; Javvi, Y.; Alfkhanji, S.; Soleimani, R. Connectionist Technique Estimates H<sub>2</sub>S Solubility in Ionic Liquids Through a Low Parameter Approach. *J. Supercrit. Fluids* **2015**, *97*, 81–87.
- (103) Hamzehie, M.; Fattah, M.; Najibi, H.; Van der Bruggen, B.; Mazinani, S. Application of artificial neural networks for estimation of solubility of acid gases (H<sub>2</sub>S and CO<sub>2</sub>) in 32 commonly ionic liquid and amine solutions. *J. Nat. Gas Sci. Eng.* **2015**, *24*, 106–114.
- (104) Zhao, Y.; Gao, H.; Zhang, X.; Huang, Y.; Bao, D.; Zhang, S. Hydrogen Sulfide Solubility in Ionic Liquids (ILs): An Extensive Database and a New ELM Model Mainly Established by Imidazolium-Based ILs. *J. Chem. Eng. Data* **2016**, *61*, 3970–3978.
- (105) Mortazavi-Manesh, S.; Satyro, M. A.; Marriott, R. A. Screening Ionic Liquids as Candidates for Separation of Acid Gases: Solubility of Hydrogen Sulfide, Methane, and Ethane. *AIChE J.* **2013**, *59*, 2993–3005.
- (106) Tennyson, R. N.; Schaaf, R. P. Guidelines can Help Choose Proper Process for Gas-Treating Plants. *Oil Gas J.* **1977**, *75*, 78–86.
- (107) Bureau, A. C.; Olden, M. J. F. Operation of the Frodingham Desulfurizing Plant at Exeter. *Chem. Eng. (London)*. **1967**, 206.
- (108) Phillipson, J. J. Desulfurization. *Catalyst Handbook*; Wolf Scientific Books: London, 1970.
- (109) Vamvuka, D.; Arvanitidis, C.; Zachariadis, D. Flue Gas Desulfurization at High Temperatures: A Review. *Environ. Eng. Sci.* **2004**, *21*, 525–548.
- (110) Cheah, S.; Carpenter, D. L.; Magrini-Bair, K. A. Review of Mid-to High-Temperature Sulfur Sorbents for Desulfurization of Biomass- and Coal-Derived Syngas. *Energy Fuels* **2009**, *23*, 5291–5307.
- (111) Westmoreland, P. R.; Harrison, D. P. Evaluation of Candidate Solids for High-Temperature Desulfurization of Low-Btu Gases. *Environ. Sci. Technol.* **1976**, *10*, 659–661.
- (112) Elseviers, W. F.; Verelst, H. Transition Metal Oxides for Hot Gas Desulphurisation. *Fuel* **1999**, *78*, 601–612.
- (113) Rodriguez, J. A.; Chaturvedi, S.; Kuhn, M.; Hrbek, J. Reaction of H<sub>2</sub>S and S<sub>2</sub> with Metal/Oxide Surfaces: Band-Gap Size and Chemical Reactivity. *J. Phys. Chem. B* **1998**, *102*, 5511–5519.
- (114) Rodriguez, J. A.; Jirsak, T.; Chaturvedi, S. Reaction of H<sub>2</sub>S with MgO (100) and Cu/MgO (100) Surfaces: Band-Gap Size and Chemical Reactivity. *J. Chem. Phys.* **1999**, *111*, 8077–8087.
- (115) Van Nisselrooy, P. F. M. T.; Lagas, J. A. Superclaus Reduces SO<sub>2</sub> Emission by the Use of a New Selective Oxidation Catalyst. *Catal. Today* **1993**, *16*, 263–271.
- (116) Polychronopoulou, K.; Galisteo, F. C.; Granados, M. L.; Fierro, J. L. G.; Bakas, T.; Efstratiou, A. M. Novel Fe-Mn-Zn-Ti-O Mixed-Metal Oxides for the Low-Temperature Removal of H<sub>2</sub>S from Gas Streams in the Presence of H<sub>2</sub>, CO<sub>2</sub>, and H<sub>2</sub>O. *J. Catal.* **2005**, *236*, 205–220.
- (117) Xue, M.; Chitrakar, R.; Sakane, K.; Ooi, K. Screening of Adsorbents for Removal of H<sub>2</sub>S at Room Temperature. *Green Chem.* **2003**, *5*, 529–534.
- (118) Casarin, M.; Maccato, C.; Vittadini, A. An LCAO-LDF Study of the Chemisorption of H<sub>2</sub>O and H<sub>2</sub>S on ZnO (0001) and ZnO (10̄10). *Surf. Sci.* **1997**, *377*–379, 587–591.
- (119) Goel, J.; Meyer, B. The Interaction of H<sub>2</sub>S with the ZnO (10̄10) Surface. *Phys. Chem. Chem. Phys.* **2013**, *15*, 8373–8382.
- (120) Song, J.; Niu, X.; Ling, L.; Wang, B. A Density Functional Theory Study on the Interaction Mechanism Between H<sub>2</sub>S and the α-Fe<sub>2</sub>O<sub>3</sub> (0001) Surface. *Fuel Process. Technol.* **2013**, *115*, 26–33.
- (121) Chen, H.-T.; Choi, Y.; Liu, M.; Lin, M. C. A First-Principles Analysis for Sulfur Tolerance of CeO<sub>2</sub> in Solid Oxide Fuel Cells. *J. Phys. Chem. C* **2007**, *111*, 11117–11122.
- (122) Huang, W.-F.; Chen, H.-T.; Lin, M. C. Density Functional Theory Study of the Adsorption and Reaction of H<sub>2</sub>S on TiO<sub>2</sub> Rutile (110) and Anatase (101) Surfaces. *J. Phys. Chem. C* **2009**, *113*, 20411–20420.
- (123) Jia, M.-Y.; Xu, B.; Ding, X.-L.; He, S.-G.; Ge, M.-F. Experimental and Theoretical Study of the Reactions Between Manganese Oxide Cluster Anions and Hydrogen Sulfide. *J. Phys. Chem. C* **2012**, *116*, 24184–24192.
- (124) Jia, M.-Y.; Xu, B.; Ding, X.-L.; Zhao, Y.-X.; He, S.-G.; Ge, M.-F. Experimental and Theoretical Study of the Reactions Between Vanadium Oxide Cluster Cations and Hydrogen Sulfide. *J. Phys. Chem. C* **2012**, *116*, 9043–9048.
- (125) Jia, M.-Y.; Xu, B.; Deng, K.; He, S.-G.; Ge, M.-F. Consecutive Oxygen-for-Sulfur Exchange Reactions between Vanadium Oxide Cluster Anions and Hydrogen Sulfide. *J. Phys. Chem. A* **2014**, *118*, 8106–8114.
- (126) Zhang, R.; Liu, H.; Li, J.; Ling, L.; Wang, B. A Mechanistic Study of H<sub>2</sub>S Adsorption and Dissociation on Cu<sub>2</sub>O (111) Surfaces: Thermochemistry, Reaction Barrier. *Appl. Surf. Sci.* **2012**, *258*, 9932–9943.
- (127) Sun, S.; Zhang, D.; Li, C.; Wang, Y. DFT Study on the Adsorption and Dissociation of H<sub>2</sub>S on CuO (111) Surface. *RSC Adv.* **2015**, *5*, 21806–21811.
- (128) Jia, M.-Y.; Luo, Z.; He, S.-G.; Ge, M.-F. Oxygen-Sulfur Exchange and the Gas-Phase Reactivity of Cobalt Sulfide Cluster Anions with Molecular Oxygen. *J. Phys. Chem. A* **2014**, *118*, 8163–8169.
- (129) Bagheri, Z.; Moradi, M. DFT Study on the Adsorption and Dissociation of Hydrogen Sulfide on MgO Nanotube. *Struct. Chem.* **2014**, *25*, 495–501.
- (130) Jia, M.-Y.; Ding, X.-L.; He, S.-G.; Ge, M.-F. Experimental and Theoretical Study of the Reactions between MO<sub>2</sub><sup>-</sup> (M = Fe, Co, Ni, Cu, and Zn) Cluster Anions and Hydrogen Sulfide. *J. Phys. Chem. A* **2013**, *117*, 8377–8387.
- (131) Baird, T.; Denny, P. J.; Hoyle, R.; McMonagle, F.; Stirling, D.; Tweedy, J. Modified Zinc Oxide Absorbents for Low-Temperature Gas Desulfurisation. *J. Chem. Soc., Faraday Trans.* **1992**, *88*, 3375–3382.
- (132) Baird, T.; Campbell, K. C.; Holliman, P. J.; Hoyle, R. W.; Huxam, M.; Stirling, D.; Williams, B. P.; Morris, M. Cobalt-zinc oxide absorbents for low temperature gas desulfurisation. *J. Mater. Chem.* **1999**, *9*, 599–605.
- (133) Carnes, C. L.; Klabunde, K. J. Unique Chemical Reactivities of Nanocrystalline Metal Oxides Toward Hydrogen Sulfide. *Chem. Mater.* **2002**, *14*, 1806–1811.
- (134) Habibi, R.; Rashidi, A. M.; Daryan, J. T.; Zadeh, A. M. A. Study of the Rod-Like and Spherical Nano-ZnO Morphology on H<sub>2</sub>S Removal from Natural Gas. *Appl. Surf. Sci.* **2010**, *257*, 434–439.
- (135) Garces, H. F.; Galindo, H. M.; Garces, L. J.; Hunt, J.; Morey, A.; Suib, S. L. Low Temperature H<sub>2</sub>S Dry-Desulfurization with Zinc Oxide. *Microporous Mesoporous Mater.* **2010**, *127*, 190–197.
- (136) Garces, H. F.; Espinal, A. E.; Suib, S. L. Tunable Shape Microwave Synthesis of Zinc Oxide Nanospheres and Their

- Desulfurization Performance Compared with Nanorods and Platelet-Like Morphologies for the Removal of Hydrogen Sulfide. *J. Phys. Chem. C* **2012**, *116*, 8465–8474.
- (137) Davidson, J. M.; Lawrie, C. H.; Sohail, K. Kinetics of the Absorption of Hydrogen Sulfide by High Purity and Doped High Surface Area Zinc Oxide. *Ind. Eng. Chem. Res.* **1995**, *34*, 2981–2989.
- (138) Novochinskii, I. I.; Song, C.; Ma, X.; Liu, X.; Shore, L.; Lampert, J.; Farrauto, R. J. Low-Temperature  $H_2S$  Removal from Steam-Containing Gas Mixtures with ZnO for Fuel Cell Application. 1. ZnO Particles and Extrudates. *Energy Fuels* **2004**, *18*, 576–583.
- (139) Yagi, S.; Kunii, D. Studies on Combustion of Carbon Particles in Flames and Fluidized Beds. *Symp. (Int.) Combust., [Proc.]* **1955**, *5*, 231–244.
- (140) Szekely, J.; Evans, J. W. A Structural Model for Gas-Solid Reactions with a Moving Boundary. *Chem. Eng. Sci.* **1970**, *25*, 1091–1107.
- (141) Gibson, J. B., III; Harrison, D. P. The Reaction Between Hydrogen Sulfide and Spherical Pellets of Zinc Oxide. *Ind. Eng. Chem. Process Des. Dev.* **1980**, *19*, 231–237.
- (142) Ranade, P. V.; Harrison, D. P. The Variable Property Grain Model Applied to the Zinc Oxide-Hydrogen Sulfide Reaction. *Chem. Eng. Sci.* **1981**, *36*, 1079–1089.
- (143) Evans, J.; Corker, J. M.; Hayter, C. E.; Oldman, R. J.; Williams, B. P. In Situ Sulfur K-Edge X-Ray Absorption Spectroscopy of the Reaction of Zinc Oxide with Hydrogen Sulfide. *Chem. Commun.* **1996**, 1431–1432.
- (144) Hayter, C. E.; Evans, J.; Corker, J. M.; Oldman, R. J.; Williams, B. P. Sulfur K-Edge X-Ray Absorption Spectroscopy Study of the Reaction of Zinc Oxide with Hydrogen Sulfide. *J. Mater. Chem.* **2002**, *12*, 3172–3177.
- (145) Samokhvalov, A.; Tatchuk, B. J. Characterization of Active Sites, Determination of Mechanisms of  $H_2S$ , COS and  $CS_2$  Sorption and Regeneration of ZnO Low-Temperature Sorbents: Past, Current and Perspectives. *Phys. Chem. Chem. Phys.* **2011**, *13*, 3197–3209.
- (146) Neveux, L.; Chiche, D.; Bazer-Bachi, D.; Favergon, L.; Pijolat, M. New Insight on the ZnO Sulfidation Reaction: Evidences for an Outward Growth Process of the ZnS Phase. *Chem. Eng. J.* **2012**, *181*–182, 508–515.
- (147) Neveux, L.; Chiche, D.; Perez-Pellitero, J.; Favergon, L.; Gay, A.-S.; Pijolat, M. New Insight into the ZnO Sulfidation Reaction: Mechanism and Kinetics Modeling of the ZnS Outward Growth. *Phys. Chem. Chem. Phys.* **2013**, *15*, 1532–1545.
- (148) Skrzypski, J.; Bezverkhyy, I.; Heintz, O.; Bellat, J.-P. Low Temperature  $H_2S$  Removal with Metal-Doped Nanostructure ZnO Sorbents: Study of the Origin of Enhanced Reactivity in Cu-Containing Materials. *Ind. Eng. Chem. Res.* **2011**, *50*, 5714–5722.
- (149) Jiang, D.; Su, L.; Ma, L.; Yao, N.; Xu, X.; Tang, H.; Li, X. Cu-Zn-Al Mixed Metal Oxides Derived from Hydroxycarbonate Precursors for  $H_2S$  Removal at Low Temperature. *Appl. Surf. Sci.* **2010**, *256*, 3216–3223.
- (150) Bezverkhyy, I.; Skrzypski, J.; Safanova, O.; Bellat, J.-P. Sulfidation Mechanism of Pure and Cu-Doped ZnO Nanoparticles at Moderate Temperature: TEM and In Situ XRD Studies. *J. Phys. Chem. C* **2012**, *116*, 14423–14430.
- (151) Baird, T.; Campbell, K. C.; Holliman, P. J.; Hoyle, R.; Stirling, D.; Williams, P. B. Mixed Co-Zn-Al Oxides as Absorbents for Low-Temperature Gas Desulfurisation. *J. Chem. Soc., Faraday Trans.* **1995**, *91*, 3219–3230.
- (152) Polychronopoulou, K.; Fierro, J. L. G.; Efstratiou, A. M. Novel Zn-Ti-based Mixed Metal Oxides for Low-Temperature Adsorption of  $H_2S$  from Industrial Gas Streams. *Appl. Catal., B* **2005**, *57*, 125–137.
- (153) Fen, L.; Bo, Y.; Jie, Z.; Anxi, J.; Chunhong, S.; Xiangji, K.; Xin, W. Study on Desulfurization Efficiency and Products of Ce-Doped Nanosized ZnO Desulfurizer at Ambient Temperature. *J. Rare Earths* **2007**, *25*, 306–310.
- (154) Westmoreland, P. R.; Gibson, J. B.; Harrison, D. P. Comparative Kinetics of High-Temperature Reaction Between Hydrogen Sulfide and Selected Metal Oxides. *Environ. Sci. Technol.* **1977**, *11*, 488–491.
- (155) Davidson, J. M.; Denny, P. J.; Lawrie, C. H. Autocatalysis by Water in the Reaction of Hydrogen Sulphide with Zinc Oxide. *J. Chem. Soc., Chem. Commun.* **1989**, 1695–1696.
- (156) Liu, C.; Zhang, R.; Wei, S.; Wang, J.; Liu, Y.; Li, M.; Liu, R. Selective Removal of  $H_2S$  from Biogas Using a Regenerable Hybrid  $TiO_2$ /Zeolite Composite. *Fuel* **2015**, *157*, 183–190.
- (157) Liu, D.; Chen, S.; Fei, X.; Huang, C.; Zhang, Y. Regenerable CuO-Based Adsorbents for Low Temperature Desulfurization Application. *Ind. Eng. Chem. Res.* **2015**, *54*, 3556–3562.
- (158) Fan, H.-L.; Sun, T.; Zhao, Y.-P.; Shangguan, J.; Lin, J.-Y. Three-Dimensionally Ordered Macroporous Iron Oxide for Removal of  $H_2S$  at Medium Temperatures. *Environ. Sci. Technol.* **2013**, *47*, 4859–4865.
- (159) Huang, G.; He, E.; Wang, Z.; Fan, H.; Shangguan, J.; Croiset, E.; Chen, Z. Synthesis and Characterization of  $\gamma$ - $Fe_2O_3$  for  $H_2S$  Removal at Low Temperature. *Ind. Eng. Chem. Res.* **2015**, *54*, 8469–8478.
- (160) Wang, L.-J.; Fan, H.-L.; Shangguan, J.; Croiset, E.; Chen, Z.; Wang, H.; Mi, J. Design of a Sorbent to Enhance Reactive Adsorption of Hydrogen Sulfide. *ACS Appl. Mater. Interfaces* **2014**, *6*, 21167–21177.
- (161) Pahalagedara, L. R.; Poyraz, A. S.; Song, W.; Kuo, C.-H.; Pahalagedara, M. N.; Meng, Y.-T.; Suib, S. L. Low Temperature Desulfurization of  $H_2S$ : High Sorption Capacities by Mesoporous Cobalt Oxide via Increased  $H_2S$  Diffusion. *Chem. Mater.* **2014**, *26*, 6613–6621.
- (162) Chung, J. B.; Chung, J. S. Desulfurization of  $H_2S$  Using Cobalt-Containing Sorbents at Low Temperatures. *Chem. Eng. Sci.* **2005**, *60*, 1515–1523.
- (163) Pouralhosseini, S. Making ZnO Adsorption More Affordable to Remove  $H_2S$  by Changing the Catalysts Regeneration Method. *Pet. Sci. Technol.* **2013**, *31*, 62–67.
- (164) McCarty, J. G.; Wise, H. Thermodynamics of Sulfur Chemisorption on Metals. I. Alumina-Supported Nickel. *J. Chem. Phys.* **1980**, *72*, 6332–6337.
- (165) McCarty, J. G.; Wise, H. Thermodynamics of Sulfur Chemisorption on Metals. II. Alumina-Supported Ruthenium. *J. Chem. Phys.* **1981**, *74*, 5877–5880.
- (166) McCarty, J. G.; Wise, H. Thermodynamics of Sulfur Chemisorption on Metals. III. Iron and Cobalt. *J. Chem. Phys.* **1982**, *76*, 1162–1167.
- (167) McCarty, J. G.; Sancier, K. M.; Wise, H. Thermodynamics of Sulfur Chemisorption on Metals: IV. Alumina-Supported Platinum. *J. Catal.* **1983**, *82*, 92–97.
- (168) Den Besten, I. E.; Selwood, P. W. The Chemisorption of Hydrogen Sulfide, Methyl Sulfide, and Cyclohexene on Supported Nickel Catalysts. *J. Catal.* **1962**, *1*, 93–102.
- (169) Oliphant, J. L.; Fowler, R. W.; Pannell, R. B.; Bartholomew, C. H. Chemisorption of Hydrogen Sulfide on Nickel and Ruthenium Catalysts: I. Desorption Isotherms. *J. Catal.* **1978**, *51*, 229–242.
- (170) Murray, E. P.; Tsai, T.; Barnett, S. A. A Direct-Methane Fuel Cell with a Ceria-Based Anode. *Nature* **1999**, *400*, 649–651.
- (171) Li, L.; King, D. L.; Liu, J.; Huo, Q.; Zhu, K.; Wang, C.; Gerber, M.; Stevens, D.; Wang, Y. Stabilization of Metal Nanoparticles in Cubic Mesostructured Silica and its Application in Regenerable Deep Desulfurization of Warm Syngas. *Chem. Mater.* **2009**, *21*, 5358–5364.
- (172) Yaghi, O. M.; Li, G.; Li, H. Selective Binding and Removal of Guests in a Microporous Metal-Organic Framework. *Nature* **1995**, *378*, 703–707.
- (173) Eddaoudi, M.; Kim, J.; Rosi, N.; Vodak, D.; Wachter, J.; O'Keeffe, M.; Yaghi, O. M. Systematic Design of Pore Size and Functionality in Isoreticular MOFs and Their Application in Methane Storage. *Science* **2002**, *295*, 469–472.
- (174) Deng, H.; Grunder, S.; Cordova, K. E.; Valente, C.; Furukawa, H.; Hmadedh, M.; Gándara, F.; Whalley, A. C.; Liu, Z.; Asahina, S.; Kazumori, H.; O'Keeffe, M.; Terasaki, O.; Stoddart, J. F.; Yaghi, O. M. Large-Pore Apertures in a Series of Metal-Organic Frameworks. *Science* **2012**, *336*, 1018–1023.

- (175) Huang, B. L.; Ni, Z.; Millward, A.; McGaughey, A. J. H.; Uher, C.; Kaviany, M.; Yaghi, O. Thermal Conductivity of a Metal-Organic Framework (MOF-5): Part II. Measurement. *Int. J. Heat Mass Transfer* **2007**, *50*, 405–411.
- (176) DeCoste, J. B.; Peterson, G. W. Metal-Organic Frameworks for Air Purification of Toxic Chemicals. *Chem. Rev.* **2014**, *114*, 5695–5727.
- (177) Barea, E.; Montoro, C.; Navarro, J. A. R. Toxic Gas Removal - Metal-Organic Frameworks for the Capture and Degradation of Toxic Gases and Vapours. *Chem. Soc. Rev.* **2014**, *43*, 5419–5430.
- (178) Hamon, L.; Serre, C.; Devic, T.; Loiseau, T.; Millange, F.; Férey, G.; de Weireld, G. Comparative Study of Hydrogen Sulfide Adsorption in the MIL-53 (Al, Cr, Fe), MIL-47 (V), MIL-100 (Cr), and MIL-101 (Cr) Metal-Organic Frameworks at Room Temperature. *J. Am. Chem. Soc.* **2009**, *131*, 8775–8777.
- (179) Hamon, L.; Leclerc, H.; Ghoufi, A.; Oliviero, L.; Travert, A.; Lavalley, J.-C.; Devic, T.; Serre, C.; Férey, G.; De Weireld, G.; Vimont, A.; Maurin, G. Molecular Insight into the Adsorption of  $\text{H}_2\text{S}$  in the Flexible MIL-53 (Cr) and Rigid MIL-47 (V) MOFs: Infrared Spectroscopy Combined to Molecular Simulations. *J. Phys. Chem. C* **2011**, *115*, 2047–2056.
- (180) Han, L.; Budge, M.; Greaney, P. A. Relationship Between Thermal Conductivity and Framework Architecture in MOF-5. *Comput. Mater. Sci.* **2014**, *94*, 292–297.
- (181) Babaei, H.; McGaughey, A. J. H.; Wilmer, C. E. Effect of Pore Size and Shape on the Thermal Conductivity of Metal-Organic Frameworks. *Chem. Sci.* **2017**, *8*, 583–589.
- (182) Vaesen, S.; Guillerm, V.; Yang, Q.; Wiersum, A. D.; Marszalek, B.; Gil, B.; Vimont, A.; Daturi, M.; Devic, T.; Llewellyn, P. L.; Serre, C.; Maurin, G.; De Weireld, G. A Robust Amino-Functionalized Titanium (IV) Based MOF for Improved Separation of Acid Gases. *Chem. Commun.* **2013**, *49*, 10082–10084.
- (183) Wynnyk, K. G.; Hojjati, B.; Pirzadeh, P.; Marriott, R. A. High-Pressure Sour Gas Adsorption on Zeolite 4A. *Adsorption* **2017**, *23*, 149–162.
- (184) Yang, Q.; Vaesen, S.; Vishnuvarthan, M.; Ragon, F.; Serre, C.; Vimont, A.; Daturi, M.; De Weireld, G.; Maurin, G. Probing the Adsorption Performance of the Hybrid Porous MIL-68 (Al): A Synergic Combination of Experimental and Modelling Tools. *J. Mater. Chem.* **2012**, *22*, 10210–10220.
- (185) Chui, S. S.-Y.; Lo, S. M.-F.; Charmant, J. P. H.; Orpen, A. G.; Williams, I. D. A Chemically Functionalizable Nanoporous Material [ $\text{Cu}_3(\text{TMA})_2(\text{H}_2\text{O})_2$ ]. *Science* **1999**, *283*, 1148–1150.
- (186) Petit, C.; Mendoza, B.; Bandosz, T. J. Hydrogen Sulfide Adsorption on MOFs and MOF/Graphite Oxide Composites. *ChemPhysChem* **2010**, *11*, 3678–3684.
- (187) Watanabe, T.; Sholl, D. S. Molecular Chemisorption on Open Metal Sites in  $\text{Cu}_3(\text{Benzene}(\text{carboxylate}))_2$ : A Spatially Periodic Density Functional Theory Study. *J. Chem. Phys.* **2010**, *133*, 094509.
- (188) Gutiérrez-Sevillano, J. J.; Martín-Calvo, A.; Dubbeldam, D.; Calero, S.; Hamad, S. Adsorption of Hydrogen Sulphide on Metal-Organic Frameworks. *RSC Adv.* **2013**, *3*, 14737–14749.
- (189) Supronowicz, B.; Mavrandonakis, A.; Heine, T. Interaction of Small Gases with the Unsaturated Metal Centers of the HKUST-1 Metal Organic Framework. *J. Phys. Chem. C* **2013**, *117*, 14570–14578.
- (190) Li, Y.; Wang, L.-J.; Fan, H.-L.; Shangguan, J.; Wang, H.; Mi, J. Removal of Sulfur Compounds by a Copper-Based Metal Organic Framework Under Ambient Conditions. *Energy Fuels* **2015**, *29*, 298–304.
- (191) Peterson, G. W.; Britt, D. K.; Sun, D. T.; Mahle, J. J.; Browne, M.; Demasky, T.; Smith, S.; Jenkins, A.; Rossin, J. A. Multifunctional Purification and Sensing of Toxic Hydride Gases by CuBTC Metal-Organic Framework. *Ind. Eng. Chem. Res.* **2015**, *54*, 3626–3633.
- (192) Ethiraj, J.; Bonino, F.; Lamberti, C.; Bordiga, S.  $\text{H}_2\text{S}$  Interaction with HKUST-1 and ZIF-8 MOFs: A Multitechnique Study. *Microporous Mesoporous Mater.* **2015**, *207*, 90–94.
- (193) Wang, X.-L.; Fan, H.-L.; Tian, Z.; He, E.-Y.; Li, Y.; Shangguan, J. Adsorptive Removal of Sulfur Compounds Using IRMOF-3 at Ambient Temperature. *Appl. Surf. Sci.* **2014**, *289*, 107–113.
- (194) Allan, P. K.; Wheatley, P. S.; Aldous, D.; Mohideen, M. I.; Tang, C.; Hriljac, J. A.; Megson, I. L.; Chapman, K. W.; De Weireld, G.; Vaesen, S.; Morris, R. E. Metal-Organic Frameworks for the Storage and Delivery of Biologically Active Hydrogen Sulfide. *Dalton Trans.* **2012**, *41*, 4060–4066.
- (195) Chavan, S.; Bonino, F.; Valenzano, L.; Civalleri, B.; Lamberti, C.; Acerbi, N.; Cavka, J. H.; Leistner, M.; Bordiga, S. Fundamental Aspects of  $\text{H}_2\text{S}$  Adsorption on CPO-27-Ni. *J. Phys. Chem. C* **2013**, *117*, 15615–15622.
- (196) Peng, X.; Cao, D. Computational Screening of Porous Carbons, Zeolites, and Metal Organic Frameworks for Desulfurization and Decarburetion of Biogas, Natural Gas, and Flue Gas. *AIChE J.* **2013**, *59*, 2928–2942.
- (197) Belmabkhout, Y.; et al. Metal-Organic Frameworks to Satisfy Gas Upgrading Demands: Fine-tuning the soc-MOF platform for the Operative Removal of  $\text{H}_2\text{S}$ . *J. Mater. Chem. A* **2017**, *5*, 3293–3303.
- (198) Burtch, N. C.; Jasuja, H.; Walton, K. S. Water Stability and Adsorption in Metal-Organic Frameworks. *Chem. Rev.* **2014**, *114*, 10575–10612.
- (199) Pang, S. H.; Han, C.; Sholl, D. S.; Jones, C. W.; Lively, R. P. Facet-Specific Stability of ZIF-8 in the Presence of Acid Gases Dissolved in Aqueous Solutions. *Chem. Mater.* **2016**, *28*, 6960–6967.
- (200) Huang, X.-C.; Lin, Y.-Y.; Zhang, J.-P.; Chen, X.-M. Ligand-Directed Strategy for Zeolite-Type Metal-Organic Frameworks: Zinc (II) Imidazolates with Unusual Zeolitic Topologies. *Angew. Chem.* **2006**, *118*, 1587–1589.
- (201) Park, K. S.; Ni, Z.; Côté, A. P.; Choi, J. Y.; Huang, R.; Uribe-Romo, F. J.; Chae, H. K.; O'Keeffe, M.; Yaghi, O. M. Exceptional Chemical and Thermal Stability of Zeolitic Imidazolate Frameworks. *Proc. Natl. Acad. Sci. U. S. A.* **2006**, *103*, 10186–10191.
- (202) Liu, Y.; Ma, Y.; Zhao, Y.; Sun, X.; Gándara, F.; Furukawa, H.; Liu, Z.; Zhu, H.; Zhu, C.; Suenaga, K.; Oleynikov, P.; Alshammari, A. S.; Zhang, X.; Terasaki, O.; Yaghi, O. M. Weaving of Organic Threads into a Crystalline Covalent Organic Framework. *Science* **2016**, *351*, 365–369.
- (203) Ben, T.; Ren, H.; Ma, S.; Cao, D.; Lan, J.; Jing, X.; Wang, W.; Xu, J.; Deng, F.; Simmons, J. M.; Qiu, S.; Zhu, G. Targeted Synthesis of a Porous Aromatic Framework with High Stability and Exceptionally High Surface Area. *Angew. Chem.* **2009**, *121*, 9621–9624.
- (204) Baerlocher, C.; McCusker, L. B. Database of Zeolite Structures, <http://www.iza-structure.org/databases/>; 2017.
- (205) Shah, M. S.; Tsapatsis, M.; Siepmann, J. I. Identifying Optimal Zeolitic Sorbents for Sweetening of Highly Sour Natural Gas. *Angew. Chem., Int. Ed.* **2016**, *55*, 5938–5942.
- (206) Flanigen, E. M.; Bennett, J. M.; Grose, R. W.; Cohen, J. P.; Patton, R. L.; Kirchner, R. M.; Smith, J. V. Silicalite, a New Hydrophobic Crystalline Silica Molecular Sieve. *Nature* **1978**, *271*, 512–516.
- (207) Maghsoudi, H.; Soltanieh, M.; Bozorgzadeh, H.; Mohamadalizadeh, A. Adsorption Isotherms and Ideal Selectivities of Hydrogen Sulfide and Carbon Dioxide over Methane for the Si-CHA Zeolite: Comparison of Carbon Dioxide and Methane Adsorption with the All-silica DD3R Zeolite. *Adsorption* **2013**, *19*, 1045–1053.
- (208) Shah, M. S.; Tsapatsis, M.; Siepmann, J. I. Monte Carlo Simulations Probing the Adsorptive Separation of Hydrogen Sulfide/Methane Mixtures using All-silica Zeolites. *Langmuir* **2015**, *31*, 12268–12278.
- (209) Shah, M. S.; Tsapatsis, M.; Siepmann, J. I. Development of Transferable Potentials for Phase Equilibria Model for Hydrogen Sulfide. *J. Phys. Chem. B* **2015**, *119*, 7041–7052.
- (210) Martin, M. G.; Siepmann, J. I. Transferable Potentials for Phase Equilibria. 1. United-Atom Description of n-Alkanes. *J. Phys. Chem. B* **1998**, *102*, 2569–2577.
- (211) Bai, P.; Tsapatsis, M.; Siepmann, J. I. TraPPE-zeo: Transferable Potentials for Phase Equilibria Force Field for All-silica Zeolites. *J. Phys. Chem. C* **2013**, *117*, 24375–24387.
- (212) Liu, T.; First, E. L.; Hasan, M. M. F.; Floudas, C. A. A Multi-Scale Approach for the Discovery of Zeolites for Hydrogen Sulfide Removal. *Comput. Chem. Eng.* **2016**, *93*, 63.

- (213) Kerr, G. T.; Johnson, G. C. Catalytic Oxidation of Hydrogen Sulfide to Sulfur over a Crystalline Aluminosilicate. *J. Phys. Chem.* **1960**, *64*, 381–382.
- (214) Dudzik, Z.; Ziôlek, M. The Specific Catalytic Activity of Sodium Faujasites in H<sub>2</sub>S Oxidation. *J. Catal.* **1978**, *51*, 345–354.
- (215) Ozekmekci, M.; Salkic, G.; Fellah, M. F. Use of Zeolites for the Removal of H<sub>2</sub>S: A Mini-Review. *Fuel Process. Technol.* **2015**, *139*, 49–60.
- (216) Deo, A. V.; Dalla Lana, I. G.; Habgood, H. W. Infrared Studies of the Adsorption and Surface Reactions of Hydrogen Sulfide and Sulfur Dioxide on Some Aluminas and Zeolites. *J. Catal.* **1971**, *21*, 270–281.
- (217) Förster, H.; Schuldt, M. Infrared Spectroscopic Study of the Adsorption of Hydrogen Sulfide on Zeolites NaA and NaCaA. *J. Colloid Interface Sci.* **1975**, *52*, 380–385.
- (218) Karge, H. G.; Raskó, J. Hydrogen Sulfide Adsorption on Faujasite-Type Zeolites with Systematically Caried Si-Al Ratios. *J. Colloid Interface Sci.* **1978**, *64*, 522–532.
- (219) Karge, H. G.; Ziôlek, M.; Łaniecki, M. U.V./Vis and I.R. Spectroscopic Study of Hydrogen Sulphide Adsorption on Faujasite-Type Zeolites. *Zeolites* **1987**, *7*, 197–202.
- (220) Howard, J.; Kadir, Z. A. The Adsorption of H<sub>2</sub>S on Some Transition Metal Exchanged Zeolites: An Infrared Study. *Spectrochim. Acta, Part A* **1985**, *41*, 825–831.
- (221) Garcia, C. L.; Lercher, J. A. Adsorption of Hydrogen Sulfide on ZSMS Zeolites. *J. Phys. Chem.* **1992**, *96*, 2230–2235.
- (222) Lechert, H.; Hennig, H. J. The Behavior of the Proton and <sup>23</sup>Na-Resonances in Zeolites of the Faujasite Type Depending on the Occupancy of Hydrogen Sulfide. *Z. Phys. Chem.* **1971**, *76*, 319–327.
- (223) Ziôlek, M. Adsorption of H<sub>2</sub>S and SO<sub>2</sub> over Faujasite Type Zeolites. *Bull. Polym. Acad. Sci., Chem.* **1984**, *32*, 285–291.
- (224) Sigot, L.; Ducom, G.; Germain, P. Adsorption of Hydrogen Sulfide (H<sub>2</sub>S) on Zeolite (Z): Retention Mechanism. *Chem. Eng. J.* **2016**, *287*, 47–53.
- (225) Fellah, M. F. Adsorption of Hydrogen Sulfide as Initial Step of H<sub>2</sub>S Removal: A DFT Study on Metal Exchanged ZSM-12 Clusters. *Fuel Process. Technol.* **2016**, *144*, 191–196.
- (226) Hernández-Maldonado, A. J.; Yang, R. T.; Chinn, D.; Munson, C. L. Partially Calcined Gismondine Type Silicoaluminophosphate SAPO-43: Isopropylamine Elimination and Separation of Carbon Dioxide, Hydrogen Sulfide, and Water. *Langmuir* **2003**, *19*, 2193–2200.
- (227) Crespo, D.; Qi, G.; Wang, Y.; Yang, F. H.; Yang, R. T. Superior Sorbent for Natural Gas Desulfurization. *Ind. Eng. Chem. Res.* **2008**, *47*, 1238–1244.
- (228) Hutson, N. D.; Reisner, B. A.; Yang, R. T.; Toby, B. H. Silver Ion-Exchanged Zeolites Y, X, and Low-Silica X: Observations of Thermally Induced Cation/Cluster Migration and the Resulting Effects on the Equilibrium Adsorption of Nitrogen. *Chem. Mater.* **2000**, *12*, 3020–3031.
- (229) Kumar, P.; Sung, C.; Muraza, O.; Cococcioni, M.; Al Hashimi, S.; McCormick, A.; Tsapatsis, M. H<sub>2</sub>S Adsorption by Ag and Cu Ion Exchanged Faujasites. *Microporous Mesoporous Mater.* **2011**, *146*, 127–133.
- (230) Sung, C.; Al Hashimi, S.; McCormick, A.; Tsapatsis, M.; Cococcioni, M. Density Functional Theory Study on the Adsorption of H<sub>2</sub>S and Other Claus Process Tail Gas Components on Copper-and Silver-Exchanged Y Zeolites. *J. Phys. Chem. C* **2012**, *116*, 3561–3575.
- (231) Sung, C.-Y.; Al Hashimi, S.; McCormick, A.; Cococcioni, M.; Tsapatsis, M. A DFT Study on Multivalent Cation-Exchanged Y Zeolites as Potential Selective Adsorbent for H<sub>2</sub>S. *Microporous Mesoporous Mater.* **2013**, *172*, 7–12.
- (232) Fellmuth, P.; Lutz, W.; Bülow, M. Influence of Weakly Coordinated Cations and Basic Sites Upon the Reaction of H<sub>2</sub>S and CO<sub>2</sub> on Zeolites. *Zeolites* **1987**, *7*, 367–371.
- (233) Lutz, W.; Suckow, M.; Bülow, M. Adsorption of Hydrogen Sulphide on Molecular Sieves: No Enrichment in the Presence of Carbon Dioxide. *Gas Sep. Purif.* **1990**, *4*, 190–196.
- (234) Bülow, M.; Lutz, W.; Suckow, M. The Mutual Transformation of Hydrogen Sulphide and Carbonyl Sulphide and its Role for Gas Desulphurization Processes with Zeolitic Molecular Sieve Sorbents. *Stud. Surf. Sci. Catal.* **1999**, *120*, 301–345.
- (235) Kuznicki, S. M. Large-pored Crystalline Titanium Molecular Sieve Zeolites. U.S. Patent US4,853,202, 1989.
- (236) Rezaei, S.; Tavana, A.; Sawada, J. A.; Wu, L.; Junaid, A. S.; Kuznicki, S. M. Novel Copper-Exchanged Titanosilicate Adsorbent for Low Temperature H<sub>2</sub>S Removal. *Ind. Eng. Chem. Res.* **2012**, *51*, 12430–12434.
- (237) Rezaei, S.; Jarligo, M. O. D.; Wu, L.; Kuznicki, S. M. Breakthrough Performances of Metal-Exchanged Nanotitanate ETS-2 Adsorbents for Room Temperature Desulfurization. *Chem. Eng. Sci.* **2015**, *123*, 444–449.
- (238) Roller, D.; Bläsing, M.; Dreger, I.; Yazdanbakhsh, F.; Sawada, J. A.; Kuznicki, S. M.; Müller, M. Removal of Hydrogen Sulfide by Metal-Doped Nanotitanate under Gasification-Like Conditions. *Ind. Eng. Chem. Res.* **2016**, *55*, 3871–3878.
- (239) Turk, A.; Sakalis, E.; Lessuck, J.; Karamitsos, H.; Rago, O. Ammonia Injection Enhances Capacity of Activated Carbon for Hydrogen Sulfide and Methyl Mercaptan. *Environ. Sci. Technol.* **1989**, *23*, 1242–1245.
- (240) Turk, A.; Sakalis, E.; Rago, O.; Karamitsos, H. Activated Carbon Systems for Removal of Light Gases. *Ann. N. Y. Acad. Sci.* **1992**, *661*, 221–228.
- (241) Adib, F.; Bagreev, A.; Bandosz, T. J. Effect of Surface Characteristics of Wood-Based Activated Carbons on Adsorption of Hydrogen Sulfide. *J. Colloid Interface Sci.* **1999**, *214*, 407–415.
- (242) Bagreev, A.; Adib, F.; Bandosz, T. J. Initial Heats of H<sub>2</sub>S Adsorption on Activated Carbons: Effect of Surface Features. *J. Colloid Interface Sci.* **1999**, *219*, 327–332.
- (243) Bandosz, T. J. Effect of Pore Structure and Surface Chemistry of Virgin Activated Carbons on Removal of Hydrogen Sulfide. *Carbon* **1999**, *37*, 483–491.
- (244) Adib, F.; Bagreev, A.; Bandosz, T. J. Adsorption/Oxidation of Hydrogen Sulfide on Nitrogen-Containing Activated Carbons. *Langmuir* **2000**, *16*, 1980–1986.
- (245) Adib, F.; Bagreev, A.; Bandosz, T. J. Analysis of the Relationship Between H<sub>2</sub>S Removal Capacity and Surface Properties of Unimpregnated Activated Carbons. *Environ. Sci. Technol.* **2000**, *34*, 686–692.
- (246) Bandosz, T. J. On the Adsorption/Oxidation of Hydrogen Sulfide on Activated Carbons at Ambient Temperatures. *J. Colloid Interface Sci.* **2002**, *246*, 1–20.
- (247) Tian, S.; Mo, H.; Zhang, R.; Ning, P.; Zhou, T. Enhanced Removal of Hydrogen Sulfide from a Gas Stream by 3-Amino-propyltriethoxysilane-Surface-Functionalized Activated Carbon. *Adsorption* **2009**, *15*, 477–488.
- (248) Bagreev, A.; Rahman, H.; Bandosz, T. J. Study of H<sub>2</sub>S Adsorption and Water Regeneration of Spent Coconut-Based Activated Carbon. *Environ. Sci. Technol.* **2000**, *34*, 4587–4592.
- (249) Bagreev, A.; Rahman, H.; Bandosz, T. J. Thermal Regeneration of a Spent Activated Carbon Previously Used as Hydrogen Sulfide Adsorbent. *Carbon* **2001**, *39*, 1319–1326.
- (250) Boudou, J.-P.; Chehimi, M.; Broniek, E.; Siemieniewska, T.; Bimer, J. Adsorption of H<sub>2</sub>S or SO<sub>2</sub> on an Activated Carbon Cloth Modified by Ammonia Treatment. *Carbon* **2003**, *41*, 1999–2007.
- (251) Bagreev, A.; Rahman, H.; Bandosz, T. J. Wood-Based Activated Carbons as Adsorbents of Hydrogen Sulfide: A Study of Adsorption and Water Regeneration Processes. *Ind. Eng. Chem. Res.* **2000**, *39*, 3849–3855.
- (252) Goh, K.; Karahan, H. E.; Wei, L.; Bae, T.-H.; Fane, A. G.; Wang, R.; Chen, Y. Carbon Nanomaterials for Advancing Separation Membranes: A Strategic Perspective. *Carbon* **2016**, *109*, 694–710.
- (253) Guan, L.; Suenaga, K.; Iijima, S. Smallest Carbon Nanotube Assigned with Atomic Resolution Accuracy. *Nano Lett.* **2008**, *8*, 459–462.
- (254) Rinzler, A. G.; Liu, J.; Dai, H.; Nikolaev, P.; Huffman, C. B.; Rodriguez-Macias, F. J.; Boul, P. J.; Lu, A. H.; Heymann, D.; Colbert,

- D. T.; Lee, R. S.; Fischer, J. E.; Rao, A. M.; Eklund, P. C.; Smalley, E. R. Large-Scale Purification of Single-Wall Carbon Nanotubes: Process, Product, and Characterization. *Appl. Phys. A: Mater. Sci. Process.* **1998**, *67*, 29–37.
- (255) Williams, K. A.; Eklund, P. C. Monte Carlo Simulations of H<sub>2</sub> Physisorption in Finite-Diameter Carbon Nanotube Ropes. *Chem. Phys. Lett.* **2000**, *320*, 352–358.
- (256) Zhang, Y.-H.; Han, L.-F.; Xiao, Y.-H.; Jia, D.-Z.; Guo, Z.-H.; Li, F. Understanding Dopant and Defect Effect on H<sub>2</sub>S Sensing Performances of Graphene: A First-Principles Study. *Comput. Mater. Sci.* **2013**, *69*, 222–228.
- (257) Castellanos Águila, J. E.; Hernández Cocoletzi, H.; Hernández Cocoletzi, G. A Theoretical Analysis of the Role of Defects in the Adsorption of Hydrogen Sulfide on Graphene. *AIP Adv.* **2013**, *3*, 032118.
- (258) Borisova, D.; Antonov, V.; Proykova, A. Hydrogen Sulfide Adsorption on a Defective Graphene. *Int. J. Quantum Chem.* **2013**, *113*, 786–791.
- (259) Hegde, V. I.; Shirodkar, S. N.; Tit, N.; Waghmare, U. V.; Yamani, Z. H. First Principles Analysis of Graphene and Its Ability to Maintain Long-Ranged Interaction with H<sub>2</sub>S. *Surf. Sci.* **2014**, *621*, 168–174.
- (260) Ganji, M. D.; Sharifi, N.; Ardjmand, M.; Ahangari, M. G. Pt-Decorated Graphene as Superior Media for H<sub>2</sub>S Adsorption: A First-Principles Study. *Appl. Surf. Sci.* **2012**, *261*, 697–704.
- (261) Sharma, S.; Verma, A. S. A Theoretical Study of H<sub>2</sub>S Adsorption on Graphene Doped with B, Al and Ga. *Phys. B* **2013**, *427*, 12–16.
- (262) Ganji, M. D.; Sharifi, N.; Ahangari, M. G. Adsorption of H<sub>2</sub>S Molecules on Non-Carbonic and Decorated Carbonic Graphenes: A van der Waals Density Functional Study. *Comput. Mater. Sci.* **2014**, *92*, 127–134.
- (263) Zhang, H.-p.; Luo, X.-g.; Song, H.-t.; Lin, X.-y.; Lu, X.; Tang, Y. DFT Study of Adsorption and Dissociation Behavior of H<sub>2</sub>S on Fe-Doped Graphene. *Appl. Surf. Sci.* **2014**, *317*, 511–516.
- (264) Mohammadi-Manesh, E.; Vaezzadeh, M.; Saeidi, M. Cu-and CuO-Decorated Graphene As a Nanosensor for H<sub>2</sub>S Detection at Room Temperature. *Surf. Sci.* **2015**, *636*, 36–41.
- (265) Pang, J.; Ma, X.; Yang, Q.; Meng, R.; Tan, C.; Sun, X.; Chen, X. Enhancement of H<sub>2</sub>S Detection in Impurity-Doped Graphene. *Int. Conf. Electron. Packag. Technol.* **2016**, 803–806.
- (266) Faye, O.; Raj, A.; Mittal, V.; Beye, A. C. H<sub>2</sub>S Adsorption on Graphene in the Presence of Sulfur: A Density Functional Theory Study. *Comput. Mater. Sci.* **2016**, *117*, 110–119.
- (267) Wang, W.; Peng, X.; Cao, D. Capture of Trace Sulfur Gases from Binary Mixtures by Single-Walled Carbon Nanotube Arrays: A Molecular Simulation Study. *Environ. Sci. Technol.* **2011**, *45*, 4832–4838.
- (268) Chen, J.-J.; Li, W.-W.; Li, X.-L.; Yu, H.-Q. Improving Biogas Separation and Methane Storage with Multilayer Graphene Nanostructure via Layer Spacing Optimization and Lithium Doping: A Molecular Simulation Investigation. *Environ. Sci. Technol.* **2012**, *46*, 10341–10348.
- (269) Gholampour, F.; Yeganegi, S. Molecular Simulation Study on the Adsorption and Separation of Acidic Gases in a Model Nanoporous Carbon. *Chem. Eng. Sci.* **2014**, *117*, 426–435.
- (270) Lei, G.; Liu, C.; Li, Q.; Xu, X. Graphyne Nanostructure as a Potential Adsorbent for Separation of H<sub>2</sub>S/CH<sub>4</sub> Mixture: Combining Grand Canonical Monte Carlo Simulations with Ideal Adsorbed Solution Theory. *Fuel* **2016**, *182*, 210–219.
- (271) Huang, L.; Seredych, M.; Bandosz, T. J.; van Duin, A. C. T.; Lu, X.; Gubbins, K. E. Controllable Atomistic Graphene Oxide Model and Its Application in Hydrogen Sulfide Removal. *J. Chem. Phys.* **2013**, *139*, 194707.
- (272) Mohamadalizadeh, A.; Towfighi, J.; Rashidi, A.; Mohajeri, A.; Golkar, M. Modification of Carbon Nanotubes for H<sub>2</sub>S Sorption. *Ind. Eng. Chem. Res.* **2011**, *50*, 8050–8057.
- (273) Yanagisawa, T.; Shimizu, T.; Kuroda, K.; Kato, C. The Preparation of Alkyltriaethylaminonium-Kaneinite Complexes and Their Conversion to Microporous Materials. *Bull. Chem. Soc. Jpn.* **1990**, *63*, 988–992.
- (274) Kresge, C. T.; Leonowicz, M. E.; Roth, W. J.; Vartuli, J. C.; Beck, J. S. Ordered Mesoporous Molecular Sieves Synthesized by a Liquid-Crystal Template Mechanism. *Nature* **1992**, *359*, 710–712.
- (275) Wang, X.; Sun, T.; Yang, J.; Zhao, L.; Jia, J. Low-Temperature H<sub>2</sub>S Removal from Gas Streams with SBA-15 Supported ZnO Nanoparticles. *Chem. Eng. J.* **2008**, *142*, 48–55.
- (276) Wang, X.; Jia, J.; Zhao, L.; Sun, T. Mesoporous SBA-15 Supported Iron Oxide: A Potent Catalyst for Hydrogen Sulfide Removal. *Water, Air, Soil Pollut.* **2008**, *193*, 247–257.
- (277) Dhage, P.; Samokhvalov, A.; Repala, D.; Duin, E. C.; Bowman, M.; Tatarchuk, B. J. Copper-Promoted ZnO/SiO<sub>2</sub> Regenerable Sorbents for the Room Temperature Removal of H<sub>2</sub>S from Reformate Gas Streams. *Ind. Eng. Chem. Res.* **2010**, *49*, 8388–8396.
- (278) Dhage, P.; Samokhvalov, A.; McKee, M. L.; Duin, E. C.; Tatarchuk, B. J. Reactive Adsorption of Hydrogen Sulfide by Promoted Sorbents Cu-ZnO/SiO<sub>2</sub>: Active Sites by Experiment and Simulation. *Surf. Interface Anal.* **2013**, *45*, 865–872.
- (279) Yang, H.; Tatarchuk, B. Novel-Doped Zinc Oxide Sorbents for Low Temperature Regenerable Desulfurization Applications. *AIChE J.* **2010**, *56*, 2898–2904.
- (280) Dhage, P.; Samokhvalov, A.; Repala, D.; Duin, E. C.; Tatarchuk, B. J. Regenerable Fe-Mn-ZnO/SiO<sub>2</sub> Sorbents for Room Temperature Removal of H<sub>2</sub>S from Fuel Reformates: Performance, Active Sites, Operando Studies. *Phys. Chem. Chem. Phys.* **2011**, *13*, 2179–2187.
- (281) Hussain, M.; Abbas, N.; Fino, D.; Russo, N. Novel Mesoporous Silica Supported ZnO Adsorbents for the Desulphurization of Biogas at Low Temperatures. *Chem. Eng. J.* **2012**, *188*, 222–232.
- (282) Elyassi, B.; Al Wahedi, Y.; Rajabbeigi, N.; Kumar, P.; Jeong, J. S.; Zhang, X.; Kumar, P.; Balasubramanian, V. V.; Katsiotis, M. S.; Mkhyoyan, K. A.; Boukos, N.; Hashimi, S. A.; Tsapatsis, M. A High-Performance Adsorbent for Hydrogen Sulfide Removal. *Microporous Mesoporous Mater.* **2014**, *190*, 152–155.
- (283) Montes, D.; Tocuyo, E.; González, E.; Rodríguez, D.; Solano, R.; Atencio, R.; Ramos, M. A.; Moronta, A. Reactive H<sub>2</sub>S Chemisorption on Mesoporous Silica Molecular Sieve-Supported CuO or ZnO. *Microporous Mesoporous Mater.* **2013**, *168*, 111–120.
- (284) Liu, G.; Huang, Z.-H.; Kang, F. Preparation of ZnO/SiO<sub>2</sub> Gel Composites and Their Performance of H<sub>2</sub>S Removal at Room Temperature. *J. Hazard. Mater.* **2012**, *215–216*, 166–172.
- (285) Mureddu, M.; Ferino, I.; Rombi, E.; Cutrufello, M. G.; Deiana, P.; Ardu, A.; Musinu, A.; Piccaluga, G.; Cannas, C. ZnO/SBA-15 Composites for Mid-Temperature Removal of H<sub>2</sub>S: Synthesis, Performance and Regeneration Studies. *Fuel* **2012**, *102*, 691–700.
- (286) Mureddu, M.; Ferino, I.; Musinu, A.; Ardu, A.; Rombi, E.; Cutrufello, M. G.; Deiana, P.; Fantauzzi, M.; Cannas, C. MeO<sub>x</sub>/SBA-15 (Me = Zn, Fe): Highly Efficient Nanosorbents for Mid-Temperature H<sub>2</sub>S Removal. *J. Mater. Chem. A* **2014**, *2*, 19396–19406.
- (287) Li, L.; Sun, T. H.; Shu, C. H.; Zhang, H. B. Low Temperature H<sub>2</sub>S Removal with 3-D Structural Mesoporous Molecular Sieves Supported ZnO from Gas Stream. *J. Hazard. Mater.* **2016**, *311*, 142–150.
- (288) Prieto, G.; Zečević, J.; Friedrich, H.; de Jong, K. P.; de Jongh, P. E. Towards Stable Catalysts By Controlling Collective Properties of Supported Metal Nanoparticles. *Nat. Mater.* **2013**, *12*, 34–39.
- (289) Li, W.; Choi, S.; Dresel, J. H.; Hornbostel, M.; Krishnan, G.; Eisenberger, P. M.; Jones, C. W. Steam-Stripping for Regeneration of Supported Amine-Based CO<sub>2</sub> Adsorbents. *ChemSusChem* **2010**, *3*, 899–903.
- (290) Hicks, J. C.; Dresel, J. H.; Fauth, D. J.; Gray, M. L.; Qi, g.; Jones, C. W. Designing Adsorbents for CO<sub>2</sub> Capture from Flue Gas-Hyperbranched Aminosilicas Capable of Capturing CO<sub>2</sub> Reversibly. *J. Am. Chem. Soc.* **2008**, *130*, 2902–2903.
- (291) Jones, C. W. C. O. CO<sub>2</sub> Capture from Dilute Gases as a Component of Modern Global Carbon Management. *Annu. Rev. Chem. Biomol. Eng.* **2011**, *2*, 31–52.

- (292) Huang, H. Y.; Yang, R. T.; Chinn, D.; Munson, C. L. Amine-grafted MCM-48 and Silica Xerogel as Superior Sorbents for Acidic Gas Removal from Natural Gas. *Ind. Eng. Chem. Res.* **2003**, *42*, 2427–2433.
- (293) Zhou, L.; Zhong, L.; Yu, M.; Zhou, Y. Sorption and Desorption of a Minor Amount of  $\text{H}_2\text{S}$  on Silica Gel Covered with a Film of Triethanolamine. *Ind. Eng. Chem. Res.* **2004**, *43*, 1765–1767.
- (294) Zhou, L.; Zhong, L.; Su, W.; Sun, Y.; Zhou, Y. Experimental Study of Removing Trace  $\text{H}_2\text{S}$  Using Solvent Coated Adsorbent for PSA. *AIChE J.* **2006**, *52*, 2066–2071.
- (295) Chu, X.; Cheng, Z.; Zhao, Y.; Xu, J.; Zhong, H.; Zhang, W.; L.; Zhou, S.; Zhu, F.; Zhou, v; Zhou, L. Study on Sorption Behaviors of  $\text{H}_2\text{S}$  by Triethanolamine-Modified Mesoporous Molecular Sieve SBA-15. *Ind. Eng. Chem. Res.* **2012**, *51*, 4407–4413.
- (296) Xue, Q.; Liu, Y. Removal of Minor Concentration of  $\text{H}_2\text{S}$  on MDEA-Modified SBA-15 for Gas Purification. *J. Ind. Eng. Chem.* **2012**, *18*, 169–173.
- (297) Xu, X.; Novochinskii, I.; Song, C. Low-Temperature Removal of  $\text{H}_2\text{S}$  by Nanoporous Composite of Polymer-Mesoporous Molecular Sieve MCM-41 as Adsorbent for Fuel Cell Applications. *Energy Fuels* **2005**, *19*, 2214–2215.
- (298) Wang, X.; Ma, X.; Sun, L.; Song, C. A Nanoporous Polymeric Sorbent for Deep Removal of  $\text{H}_2\text{S}$  from Gas Mixtures for Hydrogen Purification. *Green Chem.* **2007**, *9*, 695–702.
- (299) Wang, X.; Ma, X.; Xu, X.; Sun, L.; Song, C. Mesoporous-Molecular-Sieve-Supported Polymer Sorbents for Removing  $\text{H}_2\text{S}$  from Hydrogen Gas Streams. *Top. Catal.* **2008**, *49*, 108–117.
- (300) Ma, X.; Wang, X.; Song, C. Molecular Basket Sorbents for Separation of  $\text{CO}_2$  and  $\text{H}_2\text{S}$  from Various Gas Streams. *J. Am. Chem. Soc.* **2009**, *131*, 5777–5783.
- (301) Yoosuk, B.; Wongsanga, T.; Prasarakich, P.  $\text{CO}_2$  and  $\text{H}_2\text{S}$  Binary Sorption on Polyamine Modified Fumed Silica. *Fuel* **2016**, *168*, 47–53.
- (302) First, E. L.; Hasan, M. M. F.; Floudas, C. A. Discovery of Novel Zeolites for Natural Gas Purification through Combined Material Screening and Process Optimization. *AIChE J.* **2014**, *60*, 1767–1785.
- (303) Chen, Q.; Fan, F.; Long, D.; Liu, X.; Liang, X.; Qiao, W.; Ling, L. Poly(ethyleneimine)-Loaded Silica Monolith with a Hierarchical Pore Structure for  $\text{H}_2\text{S}$  Adsorptive Removal. *Ind. Eng. Chem. Res.* **2010**, *49*, 11408–11414.
- (304) Belmabkhout, Y.; de Weireld, G.; Sayari, A. Amine-Bearing Mesoporous Silica for  $\text{CO}_2$  and  $\text{H}_2\text{S}$  Removal from Natural Gas and Biogas. *Langmuir* **2009**, *25*, 13275–13278.
- (305) Belmabkhout, Y.; Heymans, N.; de Weireld, G.; Sayari, A. Simultaneous Adsorption of  $\text{H}_2\text{S}$  and  $\text{CO}_2$  on Triamine-Grafted Pore-Expanded Mesoporous MCM-41 Silica. *Energy Fuels* **2011**, *25*, 1310–1315.
- (306) Serna-Guerrero, R.; Belmabkhout, Y.; Sayari, A. Modeling  $\text{CO}_2$  Adsorption on Amine-Functionalized Mesoporous Silica: 1. A Semi-Empirical Equilibrium Model. *Chem. Eng. J.* **2010**, *161*, 173–181.
- (307) Anbia, M.; Babaei, M. Novel Amine Modified Nanoporous SBA-15 Sorbent for the Removal of  $\text{H}_2\text{S}$  from Gas Streams in the Presence of  $\text{CH}_4$ . *Int. J. Eng., Trans. B* **2014**, *27*, 1697–1704.
- (308) Bhandari, D. A.; Bessho, N.; Koros, W. J. Hollow Fiber Sorbents for Desulfurization of Natural Gas. *Ind. Eng. Chem. Res.* **2010**, *49*, 12038–12050.
- (309) Ebrahim, A. M.; Jagiello, J.; Bandosz, T. J. Enhanced Reactive Adsorption of  $\text{H}_2\text{S}$  on Cu-BTC/S-and N-Doped GO Composites. *J. Mater. Chem. A* **2015**, *3*, 8194–8204.
- (310) Huang, Z.-H.; Liu, G.; Kang, F. Glucose-Promoted Zn-Based Metal-Organic Framework/Graphene Oxide Composites for Hydrogen Sulfide Removal. *ACS Appl. Mater. Interfaces* **2012**, *4*, 4942–4947.
- (311) Lonkar, S. P.; Pillai, V.; Abdala, A.; Mittal, V. In Situ Formed Graphene/ZnO Nanostructured Composites for Low Temperature Hydrogen Sulfide Removal from Natural Gas. *RSC Adv.* **2016**, *6*, 81142–81150.
- (312) Seredysh, M.; Bandosz, T. J. Reactive Adsorption of Hydrogen Sulfide on Graphite Oxide/ $\text{Zr}(\text{OH})_4$  Composites. *Chem. Eng. J.* **2011**, *166*, 1032–1038.
- (313) Seredysh, M.; Mabayoje, O.; Bandosz, T. J. Visible-Light-Enhanced Interactions of Hydrogen Sulfide with Composites of Zinc (Oxy)hydroxide with Graphite Oxide and Graphene. *Langmuir* **2012**, *28*, 1337–1346.
- (314) Mabayoje, O.; Seredysh, M.; Bandosz, T. J. Cobalt (Hydr)-oxide/Graphite Oxide Composites: Importance of Surface Chemical Heterogeneity for Reactive Adsorption of Hydrogen Sulfide. *J. Colloid Interface Sci.* **2012**, *378*, 1–9.
- (315) Mabayoje, O.; Seredysh, M.; Bandosz, T. J. Enhanced Reactive Adsorption of Hydrogen Sulfide on the Composites of Graphene/Graphite Oxide with Copper (Hydr)oxychlorides. *ACS Appl. Mater. Interfaces* **2012**, *4*, 3316–3324.
- (316) Mabayoje, O.; Seredysh, M.; Bandosz, T. J. Enhanced Adsorption of Hydrogen Sulfide on Mixed Zinc/Cobalt Hydroxides: Effect of Morphology and an Increased Number of Surface Hydroxyl Groups. *J. Colloid Interface Sci.* **2013**, *405*, 218–225.
- (317) Mabayoje, O.; Seredysh, M.; Bandosz, T. J. Reactive Adsorption of Hydrogen Sulfide on Visible Light Photoactive Zinc (Hydr)oxygen/Graphite Oxide and Zinc (Hydr)oxychloride/Graphite Oxide Composites. *Appl. Catal., B* **2013**, *132-133*, 321–331.
- (318) Arcibar-Orozco, J. A.; Wallace, R.; Mitchell, J. K.; Bandosz, T. J. Role of Surface Chemistry and Morphology in the Reactive Adsorption of  $\text{H}_2\text{S}$  on Iron (Hydr)oxygen/Graphite Oxide Composites. *Langmuir* **2015**, *31*, 2730–2742.
- (319) Giannakoudakis, D. A.; Bandosz, T. J. Zinc (Hydr)oxygen/Graphite Oxide/AuNPs Composites: Role of Surface Features in  $\text{H}_2\text{S}$  Reactive Adsorption. *J. Colloid Interface Sci.* **2014**, *436*, 296–305.
- (320) Florent, M.; Bandosz, T. J. Effects of Surface Heterogeneity of Cobalt Oxyhydroxide/Graphite Oxide Composites on Reactive Adsorption of Hydrogen Sulfide. *Microporous Mesoporous Mater.* **2015**, *204*, 8–14.
- (321) Florent, M.; Wallace, R.; Bandosz, T. J. Removal of Hydrogen Sulfide at Ambient Conditions on Cadmium/GO-Based Composite Adsorbents. *J. Colloid Interface Sci.* **2015**, *448*, 573–581.
- (322) Giannakoudakis, D. A.; Jiang, M.; Bandosz, T. J. Highly Efficient Air Desulfurization on Self-Assembled Bundles of Copper Hydroxide Nanorods. *ACS Appl. Mater. Interfaces* **2016**, *8*, 31986–31994.
- (323) Song, H. S.; Park, M. G.; Ahn, W.; Lim, S. N.; Yi, K. B.; Croiset, E.; Chen, Z.; Nam, S. C. Enhanced Adsorption of Hydrogen Sulfide and Regeneration Ability on the Composites of Zinc Oxide with Reduced Graphite Oxide. *Chem. Eng. J.* **2014**, *253*, 264–273.
- (324) Lonkar, S. P.; Pillai, V. V.; Stephen, S.; Abdala, A.; Mittal, V. Facile In Situ Fabrication of Nanostructured Graphene-CuO Hybrid with Hydrogen Sulfide Removal Capacity. *Nano-Micro Lett.* **2016**, *8*, 312–319.
- (325) Fauteux-Lefebvre, C.; Abatzoglou, N.; Braidy, N.; Hu, Y. Carbon Nanofilaments Functionalized with Iron Oxide Nanoparticles for In-Depth Hydrogen Sulfide Adsorption. *Ind. Eng. Chem. Res.* **2015**, *54*, 9230–9237.
- (326) Zhang, J.; Wang, L.; Song, H.; Song, H. Adsorption of Low-Concentration  $\text{H}_2\text{S}$  on Manganese Dioxide-Loaded Activated Carbon. *Res. Chem. Intermed.* **2015**, *41*, 6087–6104.
- (327) Balsamo, M.; Cimino, S.; de Falco, G.; Erto, A.; Lisi, L. ZnO-CuO Supported on Activated Carbon for  $\text{H}_2\text{S}$  Removal at Room Temperature. *Chem. Eng. J.* **2016**, *304*, 399–407.
- (328) UOP LLC. Handling of Zeolite Molecular Sieve Adsorbents in Process Units, UOPS085, April 2009; <https://www.uop.com/?document=uop-molsiv-handling-procedures-brochure&download=1>.
- (329) Pullumbi, P. Gas Separation by Polymer Membranes: Research Activity and Industrial Applications. In *Membrane Reactor Engineering: Applications for a Greener Process Industry*; Basile, A., De Falco, M., Centi, G., Iaquaniello, G., Eds.; John Wiley & Sons: New York, 2016; p 259.
- (330) Bhide, B. D.; Stern, S. A. Membrane Processes for the Removal of Acid Gases from Natural Gas. II. Effects of Operating Conditions, Economic Parameters, and Membrane Properties. *J. Membr. Sci.* **1993**, *81*, 239–252.

- (331) Baker, R. W.; Lokhandwala, K. Natural Gas Processing with Membranes: An Overview. *Ind. Eng. Chem. Res.* **2008**, *47*, 2109–2121.
- (332) Schell, W. J.; Wensley, C. G.; Chen, M. S. K.; Venugopal, K. G.; Miller, B. D.; Stuart, J. A. Recent Advances in Cellulosic Membranes for Gas Separation and Pervaporation. *Gas Sep. Purif.* **1989**, *3*, 162–169.
- (333) Chatterjee, G.; Houde, A. A.; Stern, S. A. Poly(Ether Urethane) and Poly(Ether Urethane Urea) Membranes with High  $\text{H}_2\text{S}/\text{CH}_4$  Selectivity. *J. Membr. Sci.* **1997**, *135*, 99–106.
- (334) Achoundong, C. S. K.; Bhuwania, N.; Burgess, S. K.; Karvan, O.; Johnson, J. R.; Koros, W. J. Silane Modification of Cellulose Acetate Dense Films as Materials for Acid Gas Removal. *Macromolecules* **2013**, *46*, 5584–5594.
- (335) Brun, J. P.; Larchet, C.; Melet, R.; Bulvestre, G. Modelling of the Pervaporation of Binary Mixtures Through Moderately Swelling, Non-Reacting Membranes. *J. Membr. Sci.* **1985**, *23*, 257–283.
- (336) Story, B. J.; Koros, W. J. Comparison of Three Models for Permeation of  $\text{CO}_2/\text{CH}_4$  Mixtures in Poly(phenylene oxide). *J. Polym. Sci., Part B: Polym. Phys.* **1989**, *27*, 1927–1948.
- (337) Donohue, M. D.; Minhas, B. S.; Lee, S. Y. Permeation Behavior of Carbon Dioxide-Methane Mixtures in Cellulose Acetate Membranes. *J. Membr. Sci.* **1989**, *42*, 197–214.
- (338) Huang, Y.; Paul, D. R. Physical Aging of Thin Glassy Films Monitored by Gas Permeability. *Polymer* **2004**, *45*, 8377–8393.
- (339) Heilman, W.; Tammela, V.; Meyer, J. A.; Stannett, V.; Szwarc, M. Permeability of Polymer Films to Hydrogen Sulfide Gas. *Ind. Eng. Chem.* **1956**, *48*, 821–824.
- (340) Kulprathipanja, S. Separation of Polar Gases from Nonpolar Gases. U.S. Patent US4,606,740, 1986.
- (341) Kulprathipanja, S.; Kulkarni, S. S. Separation of polar gases from nonpolar gases. U.S. Patent US4,608,060, 1986.
- (342) Stern, S. A.; Bhide, B. D. Permeability of Silicone Polymers to Ammonia and Hydrogen Sulfide. *J. Appl. Polym. Sci.* **1989**, *38*, 2131–2147.
- (343) Blume, I.; Pinna, I. Composite Membrane, Method of Preparation and Use. U.S. Patent US4,963,165, 1990.
- (344) Lokhandwala, K. A.; Baker, R. W.; Amo, K. D. Sour Gas Treatment Process. U.S. Patent US5,407,467, 1995.
- (345) Quinn, R.; Laciak, D. V. Polyelectrolyte Membranes for Acid Gas Separations. *J. Membr. Sci.* **1997**, *131*, 49–60.
- (346) Quinn, R.; Laciak, D. V.; Pez, G. P. Polyelectrolyte-Salt Blend Membranes for Acid Gas Separations. *J. Membr. Sci.* **1997**, *131*, 61–69.
- (347) Amirkhanov, D. M.; Kotenko, A. A.; Tul'skii, M. N.; Chelyak, M. M. Hollow Fibres for Removal and Concentration of Hydrogen Sulfide from Gas Mixtures by the Membrane Method. *Fibre Chem.* **2001**, *33*, 67–72.
- (348) Wilks, B.; Rezac, M. E. Properties of Rubbery Polymers for the Recovery of Hydrogen Sulfide from Gasification Gases. *J. Appl. Polym. Sci.* **2002**, *85*, 2436–2444.
- (349) Orme, C. J.; Klaehn, J. R.; Stewart, F. F. Gas Permeability and Ideal Selectivity of Poly[Bis-(Phenoxy)Phosphazene], Poly[Bis-(4-Tert-Butylphenoxy)Phosphazene], and Poly[Bis-(3, 5-di-Tert-Butylphenoxy)<sub>1.2</sub>(Chloro)<sub>0.8</sub>Phosphazene]. *J. Membr. Sci.* **2004**, *238*, 47–55.
- (350) Orme, C. J.; Stewart, F. F. Mixed Gas Hydrogen Sulfide Permeability and Separation Using Supported Polyphosphazene Membranes. *J. Membr. Sci.* **2005**, *253*, 243–249.
- (351) Merkel, T. C.; Toy, L. G. Comparison of Hydrogen Sulfide Transport Properties in Fluorinated and Nonfluorinated Polymers. *Macromolecules* **2006**, *39*, 7591–7600.
- (352) Sridhar, S.; Smitha, B.; Mayor, S.; Prathab, B.; Aminabhavi, T. M. Gas Permeation Properties of Polyamide Membrane Prepared by Interfacial Polymerization. *J. Mater. Sci.* **2007**, *42*, 9392–9401.
- (353) Mohammadi, T.; Moghadam, M. T.; Saeidi, M.; Mahdyarfar, M. Acid Gas Permeation Behavior through Poly(Ester Urethane Urea) Membrane. *Ind. Eng. Chem. Res.* **2008**, *47*, 7361–7367.
- (354) Saeidi, M.; Moghadam, M. T.; Mahdyarfar, M.; Mohammadi, T. Gas Permeation Properties of Seragel Membrane. *Asia-Pac. J. Chem. Eng.* **2010**, *5*, 324–329.
- (355) Chenar, M. P.; Savoji, H.; Soltanieh, M.; Matsuura, T.; Tabe, S. Removal of Hydrogen Sulfide from Methane Using Commercial Polyphenylene Oxide and Cardo-Type Polyimide Hollow Fiber Membranes. *Korean J. Chem. Eng.* **2011**, *28*, 902–913.
- (356) Vaughn, J.; Koros, W. J. Effect of the Amide Bond Diamine Structure on the  $\text{CO}_2$ ,  $\text{H}_2\text{S}$ , and  $\text{CH}_4$  Transport Properties of a Series of Novel 6FDA-Based Polyamide-Imines for Natural Gas Purification. *Macromolecules* **2012**, *45*, 7036–7049.
- (357) Kraftschik, B.; Koros, W. J.; Johnson, J. R.; Karvan, O. Dense Film Polyimide Membranes for Aggressive Sour Gas Feed Separations. *J. Membr. Sci.* **2013**, *428*, 608–619.
- (358) Kraftschik, B.; Koros, W. J. Cross-Linkable Polyimide Membranes for Improved Plasticization Resistance and Permselectivity in Sour Gas Separations. *Macromolecules* **2013**, *46*, 6908–6921.
- (359) Vaughn, J. T.; Koros, W. J. Analysis of Feed Stream Acid Gas Concentration Effects on the Transport Properties and Separation Performance of Polymeric Membranes for Natural Gas Sweetening: A Comparison Between a Glassy and Rubbery Polymer. *J. Membr. Sci.* **2014**, *465*, 107–116.
- (360) Yi, S.; Ma, X.; Pinna, I.; Koros, W. J. A High-Performance Hydroxyl-Functionalized Polymer of Intrinsic Microporosity for an Environmentally Attractive Membrane-Based Approach to Decontamination of Sour Natural Gas. *J. Mater. Chem. A* **2015**, *3*, 22794–22806.
- (361) Yahaya, G. O.; Qahtani, M. S.; Ammar, A. Y.; Bahamdan, A. A.; Ameen, A. W.; Alhajry, R. H.; Sultan, M. M. B.; Hamad, F. Aromatic Block Co-Polyimide Membranes for Sour Gas Feed Separations. *Chem. Eng. J.* **2016**, *304*, 1020–1030.
- (362) Saedi, S.; Madaeni, S. S.; Shamsabadi, A. A. PDMS Coated Asymmetric PES Membrane for Natural Gas Sweetening: Effect of Preparation and Operating Parameters on Performance. *Can. J. Chem. Eng.* **2014**, *92*, 892–904.
- (363) Li, N. N.; Funk, E. W.; Chang, Y. A.; Kulkarni, S. S.; Swamikannu, A. X.; White, L. S. *Membrane Separation Processes in the Petrochemical Industry: Phase II, April 1, 1984–October 30, 1985*, DOE/ID/12422-2; U.S. Department of Energy, Sept 30, 1987.
- (364) Lokhandwala, K. A.; Baker, R. W. Sour Gas Treatment Process Including Membrane and Non-Membrane Treatment Steps. U.S. Patent US5,407,466, 1995.
- (365) Baker, R. W.; Low, B. T. Gas Separation Membrane Materials: A Perspective. *Macromolecules* **2014**, *47*, 6999–7013.
- (366) Budd, P. M.; Elabas, E. S.; Ghanem, B. S.; Makhseed, S.; McKeown, N. B.; Msayib, K. J.; Tattershall, C. E.; Wang, D. Solution-Processed, Organophilic Membrane Derived from a Polymer of Intrinsic Microporosity. *Adv. Mater.* **2004**, *16*, 456–459.
- (367) McKeown, N. B.; Budd, P. M. Polymers of Intrinsic Microporosity (PIMs): Organic Materials for Membrane Separations, Heterogeneous Catalysis and Hydrogen Storage. *Chem. Soc. Rev.* **2006**, *35*, 675–683.
- (368) Swaidan, R.; Ghanem, B. S.; Litwiller, E.; Pinna, I. Pure- and Mixed-Gas  $\text{CO}_2/\text{CH}_4$  Separation Properties of PIM-1 and an Amidoxime-Functionalized PIM-1. *J. Membr. Sci.* **2014**, *457*, 95–102.
- (369) Ma, X.; Swaidan, R.; Belmabkhout, Y.; Zhu, Y.; Litwiller, E.; Jouiad, M.; Pinna, I.; Han, Y. Synthesis and Gas Transport Properties of Hydroxyl-Functionalized Polyimides with Intrinsic Microporosity. *Macromolecules* **2012**, *45*, 3841–3849.
- (370) Heyd, R. L.; McCandless, F. P. Separation of  $\text{H}_2\text{S}$  from  $\text{N}_2$  by Selective Permeation through Polymeric Membranes. *J. Membr. Sci.* **1977**, *2*, 375–389.
- (371) Hao, J.; Rice, P. A.; Stern, S. A. Upgrading Low-Quality Natural Gas with  $\text{H}_2\text{S}$ - and  $\text{CO}_2$ -Selective Polymer Membranes: Part I. Process Design and Economics of Membrane Stages without Recycle Streams. *J. Membr. Sci.* **2002**, *209*, 177–206.
- (372) Hao, J.; Rice, P. A.; Stern, S. A. Upgrading Low-Quality Natural Gas with  $\text{H}_2\text{S}$ - and  $\text{CO}_2$ -Selective Polymer Membranes: Part II. Process Design, Economics, and Sensitivity Study of Membrane Stages with Recycle Streams. *J. Membr. Sci.* **2008**, *320*, 108–122.

- (373) Ren, X.; Ren, J.; Deng, M. Poly(Amide-6-b-Ethylene Oxide) Membranes for Sour Gas Separation. *Sep. Purif. Technol.* **2012**, *89*, 1–8.
- (374) Zhao, S.; Feron, P. H. M.; Deng, L.; Favre, E.; Chabanon, E.; Yan, S.; Hou, J.; Chen, V.; Qi, H. Status and Progress of Membrane Contactors in Post-Combustion Carbon Capture: A State-of-the-Art Review of New Developments. *J. Membr. Sci.* **2016**, *511*, 180–206.
- (375) Qi, Z.; Cussler, E. L. Microporous Hollow Fibers for Gas Absorption: I. Mass Transfer in the Liquid. *J. Membr. Sci.* **1985**, *23*, 321–332.
- (376) Qi, Z.; Cussler, E. L. Microporous Hollow Fibers for Gas Absorption: II. Mass Transfer Across the Membrane. *J. Membr. Sci.* **1985**, *23*, 333–345.
- (377) Mansourizadeh, A.; Ismail, A. F. Hollow Fiber Gas-Liquid Membrane Contactors for Acid Gas Capture: A Review. *J. Hazard. Mater.* **2009**, *171*, 38–53.
- (378) Li, K.; Wang, D.; Koe, C. C.; Teo, W. K. Use of Asymmetric Hollow Fibre Modules for Elimination of  $H_2S$  from Gas Streams via a Membrane Absorption Method. *Chem. Eng. Sci.* **1998**, *53*, 1111–1119.
- (379) Li, K.; Kong, J. F.; Wang, D.; Teo, W. K. Tailor-Made Asymmetric PVDF Hollow Fibers for Soluble Gas Removal. *AIChE J.* **1999**, *45*, 1211–1219.
- (380) Wang, D.; Teo, W. K.; Li, K. Removal of  $H_2S$  to Ultra-Low Concentrations Using an Asymmetric Hollow Fibre Membrane Module. *Sep. Purif. Technol.* **2002**, *27*, 33–40.
- (381) Wang, D.; Teo, W.; Li, K. Selective Removal of Trace  $H_2S$  from Gas Streams Containing  $CO_2$  Using Hollow Fibre Membrane Modules/Contractors. *Sep. Purif. Technol.* **2004**, *35*, 125–131.
- (382) Marzouk, S. A. M.; Al-Marzouqi, M. H.; Abdullatif, N.; Ismail, Z. M. Removal of Percentile Level of  $H_2S$  from Pressurized  $H_2S$ - $CH_4$  Gas Mixture Using Hollow Fiber Membrane Contactors and Absorption Solvents. *J. Membr. Sci.* **2010**, *360*, 436–441.
- (383) Hedayat, M.; Soltanieh, M.; Mousavi, S. A. Simultaneous Separation of  $H_2S$  and  $CO_2$  from Natural Gas by Hollow Fiber Membrane Contactor Using Mixture of Alkanolamines. *J. Membr. Sci.* **2011**, *377*, 191–197.
- (384) Marzouk, S. A. M.; Al-Marzouqi, M. H.; Teramoto, M.; Abdullatif, N.; Ismail, Z. M. Simultaneous Removal of  $CO_2$  and  $H_2S$  from Pressurized  $CO_2$ - $H_2S$ - $CH_4$  Gas Mixture Using Hollow Fiber Membrane Contactors. *Sep. Purif. Technol.* **2012**, *86*, 88–97.
- (385) Rongwong, W.; Boributh, S.; Assabumrungrat, S.; Laosiripojana, N.; Jiraratananon, R. Simultaneous Absorption of  $CO_2$  and  $H_2S$  from Biogas by Capillary Membrane Contactor. *J. Membr. Sci.* **2012**, *392*–393, 38–47.
- (386) Esquiroz-Molina, A.; Georgaki, S.; Stuetz, R.; Jefferson, B.; McAdam, E. J. Influence of pH on Gas Phase Controlled Mass Transfer in a Membrane Contactor for Hydrogen Sulphide Absorption. *J. Membr. Sci.* **2013**, *427*, 276–282.
- (387) Boucif, N.; Favre, E.; Roizard, D.; Belloul, M. Hollow Fiber Membrane Contactor for Hydrogen Sulfide Odor Control. *AIChE J.* **2008**, *54*, 122–131.
- (388) Faiz, R.; Al-Marzouqi, M. Mathematical Modeling for the Simultaneous Absorption of  $CO_2$  and  $H_2S$  Using MEA in Hollow Fiber Membrane Contactors. *J. Membr. Sci.* **2009**, *342*, 269–278.
- (389) Faiz, R.; Al-Marzouqi, M.  $H_2S$  Absorption via Carbonate Solution in Membrane Contactors: Effect of Species Concentrations. *J. Membr. Sci.* **2010**, *350*, 200–210.
- (390) Faiz, R.; Al-Marzouqi, M. Insights on Natural Gas Purification: Simultaneous Absorption of  $CO_2$  and  $H_2S$  Using Membrane Contactors. *Sep. Purif. Technol.* **2011**, *76*, 351–361.
- (391) Sohrabi, M. R.; Marjani, A.; Moradi, S.; Davallo, M.; Shirazian, S. Simulation Studies on  $H_2S$  Absorption in Potassium Carbonate Aqueous Solution Using a Membrane Module. *Asian J. Chem.* **2011**, *23*, 4227.
- (392) Mahdavian, M.; Atashi, H.; Zivdar, M.; Mousavi, M. Simulation of  $CO_2$  and  $H_2S$  Removal Using Methanol in Hollow Fiber Membrane Gas Absorber (HFMGA). *Adv. Chem. Eng. Sci.* **2012**, *2*, 50–61.
- (393) Amrei, S. M. H. H.; Memardoost, S.; Dehkordi, A. M. Comprehensive Modeling and CFD Simulation of Absorption of  $CO_2$  and  $H_2S$  by MEA Solution in Hollow Fiber Membrane Reactors. *AIChE J.* **2014**, *60*, 657–672.
- (394) Faiz, R.; Li, K.; Al-Marzouqi, M.  $H_2S$  Absorption at High Pressure Using Hollow Fibre Membrane Contactors. *Chem. Eng. Process.* **2014**, *83*, 33–42.
- (395) Schlünder, E. U. On the Mechanism of Mass Transfer in Heterogeneous SystemsIn particular in Fixed Beds, Fluidized Beds and on Bubble Trays. *Chem. Eng. Sci.* **1977**, *32*, 845–851.
- (396) Cussler, R. L. *Diffusion: Mass Transfer in Fluid Systems*, 3rd ed.; Cambridge University Press, New York, 2009.
- (397) Prasad, R.; Sirkar, K. K. Dispersion-Free Solvent Extraction with Microporous Hollow-Fiber Modules. *AIChE J.* **1988**, *34*, 177–188.
- (398) Maghsoudi, H.; Soltanieh, M. Simultaneous Separation of  $H_2S$  and  $CO_2$  from  $CH_4$  by a High Silica CHA-Type Zeolite Membrane. *J. Membr. Sci.* **2014**, *470*, 159–165.
- (399) Bunch, J. S.; Verbridge, S. S.; Alden, J. S.; van der Zande, A. M.; Parpia, J. M.; Craighead, H. G.; McEuen, P. L. Impermeable Atomic Membranes from Graphene Sheets. *Nano Lett.* **2008**, *8*, 2458–2462.
- (400) Jiang, D.; Cooper, V. R.; Dai, S. Porous Graphene as the Ultimate Membrane for Gas Separation. *Nano Lett.* **2009**, *9*, 4019–4024.
- (401) Koenig, S. P.; Wang, L.; Pellegrino, J.; Bunch, J. S. Selective Molecular Sieving Through Porous Graphene. *Nat. Nanotechnol.* **2012**, *7*, 728–732.
- (402) O'Hern, S. C.; Stewart, C. A.; Boutilier, M. S. H.; Idrobo, J.-C.; Bhatirupudi, S.; Das, S. K.; Kong, J.; Laoui, T.; Atieh, M.; Karnik, R. Selective Molecular Transport Through Intrinsic Defects in a Single Layer of CVD Graphene. *ACS Nano* **2012**, *6*, 10130–10138.
- (403) Kim, H. W.; Yoon, H. W.; Yoon, S.-M.; Yoo, B. M.; Ahn, B. K.; Cho, Y. H.; Shin, H. J.; Yang, H.; Paik, U.; Kwon, S.; Choi, J.-Y.; Park, H. B. Selective Gas Transport Through Few-Layered Graphene and Graphene Oxide Membranes. *Science* **2013**, *342*, 91–95.
- (404) Li, H.; Song, Z.; Zhang, X.; Huang, Y.; Li, S.; Mao, Y.; Ploehn, H. J.; Bao, Y.; Yu, M. Ultrathin, Molecular-Sieving Graphene Oxide Membranes for Selective Hydrogen Separation. *Science* **2013**, *342*, 95–98.
- (405) Boutilier, M. S. H.; Sun, C.; O'Hern, S. C.; Au, H.; Hadjiconstantinou, N. G.; Karnik, R. Implications of Permeation Through Intrinsic Defects in Graphene on the Design of Defect-Tolerant Membranes for Gas Separation. *ACS Nano* **2014**, *8*, 841–849.
- (406) Celebi, K.; Buchheim, J.; Wyss, R. M.; Droudian, A.; Gasser, P.; Shorubalko, I.; Kye, J.-I.; Lee, C.; Park, H. G. Ultimate Permeation Across Atomically Thin Porous Graphene. *Science* **2014**, *344*, 289–292.
- (407) Joshi, R. K.; Carbone, P.; Wang, F. C.; Kravets, V. G.; Su, Y.; Grigorieva, I. V.; Wu, H. A.; Geim, A. K.; Nair, R. R. Precise and ultrafast molecular sieving through graphene oxide membranes. *Science* **2014**, *343*, 752–754.
- (408) Sun, C.; Boutilier, M. S. H.; Au, H.; Poesio, P.; Bai, B.; Karnik, R.; Hadjiconstantinou, N. G. Mechanisms of Molecular Permeation Through Nanoporous Graphene Membranes. *Langmuir* **2014**, *30*, 675–682.
- (409) Hashimoto, A.; Suenaga, K.; Gloter, A.; Urita, K.; Iijima, S. Direct Evidence for Atomic Defects in Graphene Layers. *Nature* **2004**, *430*, 870–873.
- (410) Bieri, M.; Treier, M.; Cai, J.; Ait-Mansour, K.; Ruffieux, P.; Gröning, O.; Gröning, P.; Kastler, M.; Rieger, R.; Feng, X.; Müllen, K.; Fasel, R. Porous Graphenes: Two-Dimensional Polymer Synthesis with Atomic Precision. *Chem. Commun.* **2009**, 6919–6921.
- (411) Lei, G.; Liu, C.; Xie, H.; Song, F. Separation of the Hydrogen Sulfide and Methane Mixture by the Porous Graphene Membrane: Effect of the Charges. *Chem. Phys. Lett.* **2014**, *599*, 127–132.
- (412) Sun, C.; Wen, B.; Bai, B. Application of Nanoporous Graphene Membranes in Natural Gas Processing: Molecular Simulations of  $CH_4$ / $CO_2$ ,  $CH_4$ / $H_2S$  and  $CH_4$ / $N_2$  Separation. *Chem. Eng. Sci.* **2015**, *138*, 616–621.

- (413) Jones, C. W.; Koros, W. J. carbon Molecular Sieve Gas Separation Membranes-I. Preparation and Characterization Based on Polyimide Precursors. *Carbon* **1994**, *32*, 1419–1425.
- (414) Sedigh, M. G.; Onstot, W. J.; Xu, L.; Peng, W. L.; Tsotsis, T. T.; Sahimi, M. Experiments and Simulation of Transport and Separation of Gas Mixtures in Carbon Molecular Sieve Membranes. *J. Phys. Chem. A* **1998**, *102*, 8580–8589.
- (415) Wenz, G. B.; Koros, W. J. Tuning Carbon Molecular Sieves for Natural Gas Separations: A Diamine Molecular Approach. *AICHE J.* **2017**, *63*, 751–760.
- (416) Hinds, B. J.; Chopra, N.; Rantell, T.; Andrews, R.; Gavalas, V.; Bachas, L. G. Aligned Multiwalled Carbon Nanotube Membranes. *Science* **2004**, *303*, 62–65.
- (417) Gilani, N.; Towfighi, J.; Rashidi, A. Performance Enhancement of Vertically Aligned Carbon Nanotube Membranes for Separation of Binary Mixtures of  $\text{H}_2\text{S}/\text{CH}_4$  Using Different Amine Groups. *Mater. Res. Bull.* **2016**, *77*, 155–165.
- (418) Lee, S.-H.; Kim, B.-S.; Lee, E.-W.; Park, Y.-I.; Lee, J.-M. The Removal of Acid Gases from Crude Natural Gas by Using Novel Supported Liquid Membranes. *Desalination* **2006**, *200*, 21–22.
- (419) Park, Y.-I.; Kim, B.-S.; Byun, Y.-H.; Lee, S.-H.; Lee, E.-W.; Lee, J.-M. Preparation of Supported Ionic Liquid Membranes (SILMs) for the Removal of Acidic Gases from Crude Natural Gas. *Desalination* **2009**, *236*, 342–348.
- (420) Wang, S.; Wu, D.; Huang, H.; Yang, Q.; Tong, M.; Liu, D.; Zhong, C. Computational Exploration of  $\text{H}_2\text{S}/\text{CH}_4$  Mixture Separation Using Acid-Functionalized UiO-66 (Zr) Membrane and Composites. *Chin. J. Chem. Eng.* **2015**, *23*, 1291–1299.
- (421) Skouidas, A. I.; Sholl, D. S.; Krishna, R. Correlation Effects in Diffusion of  $\text{CH}_4/\text{CF}_4$  Mixtures in MFI Zeolite. A Study Linking MD Simulations with the Maxwell-Stefan Formulation. *Langmuir* **2003**, *19*, 7977–7988.
- (422) Li, Z.; Liao, F.; Jiang, F.; Liu, B.; Ban, S.; Chen, G.; Sun, C.; Xiao, P.; Sun, Y. Capture of  $\text{H}_2\text{S}$  and  $\text{SO}_2$  from Trace Sulfur Containing Gas Mixture by Functionalized UiO-66 (Zr) Materials: A Molecular Simulation Study. *Fluid Phase Equilib.* **2016**, *427*, 259–267.
- (423) Reamer, H. H.; Sage, B. H.; Lacey, W. N. Phase Equilibria in Hydrocarbon Systems - Volumetric and Phase Behavior of the Methane-Hydrogen Sulfide System. *Ind. Eng. Chem.* **1951**, *43*, 976–981.
- (424) Kohn, J. P.; Kurata, F. Heterogeneous Phase Equilibria of the Methane-Hydrogen Sulfide System. *AICHE J.* **1958**, *4*, 211–217.
- (425) Kohn, J.; Kurata, F. Volumetric Behavior of the Methane-Hydrogen Sulfide System at Low Temperatures and High Pressures. *J. Chem. Eng. Data* **1959**, *4*, 33–36.
- (426) Coquelet, C.; Valtz, A.; Stringari, P.; Popovic, M.; Richon, D.; Mougin, P. Phase Equilibrium Data for the Hydrogen Sulphide + Methane System at Temperatures from 186 to 313 K and Pressures Up to About 14 MPa. *Fluid Phase Equilib.* **2014**, *383*, 94–99.
- (427) Lange, S.; Campestrini, M.; Stringari, P. Phase Behavior of System Methane + Hydrogen Sulfide. *AICHE J.* **2016**, *62*, 4090–4108.
- (428) Perez, A. G.; Valtz, A.; Coquelet, C.; Paricaud, P.; Chapoy, A. Experimental and Modelling Study of the Densities of the Hydrogen Sulphide + Methane Mixtures at 253, 273 and 293 K and Pressures up to 30 MPa. *Fluid Phase Equilib.* **2016**, *427*, 371–383.
- (429) Lallemand, F.; Lecomte, F.; Streicher, C. *Highly Sour Gas Processing:  $\text{H}_2\text{S}$  Bulk Removal With The Sprex Process*. International Petroleum Technology Conference, Doha, Qatar, Nov 21–23, 2005; DOI: [10.2523/IPTC-10581-MS](https://doi.org/10.2523/IPTC-10581-MS).